

Ahmet ÖZDİL

A Ph.D. Thesis

AGU 2022

AUTOMATED PROCESSING AND CLASSIFICATION OF MEDICAL THERMAL IMAGES

A THESIS

SUBMITTED TO THE DEPARTMENT OF ELECTRICAL AND
COMPUTER ENGINEERING AND THE GRADUATE SCHOOL OF
ENGINEERING AND SCIENCE OF ABDULLAH GUL UNIVERSITY
IN PARTIAL FULFILLMENT OF THE REQUIREMENTS
FOR THE DEGREE OF
Ph.D.

By

Ahmet ÖZDİL

June 2022

AUTOMATED PROCESSING AND
CLASSIFICATION OF MEDICAL THERMAL
IMAGES

A THESIS

SUBMITTED TO THE DEPARTMENT OF ELECTRICAL AND COMPUTER
ENGINEERING AND THE GRADUATE SCHOOL OF ENGINEERING AND
SCIENCE OF ABDULLAH GUL UNIVERSITY
IN PARTIAL FULFILLMENT OF THE REQUIREMENTS
FOR THE DEGREE OF
Ph.D.

By
Ahmet ÖZDİL
June 2022

SCIENTIFIC ETHICS COMPLIANCE

I hereby declare that all information in this document has been obtained in accordance with academic rules and ethical conduct. I also declare that, as required by these rules and conduct, I have fully cited and referenced all materials and results that are not original to this work.

Name-Surname: Ahmet ÖZDİL

Signature :

X X X X

REGULATORY COMPLIANCE

Ph.D. thesis titled “AUTOMATED PROCESSING AND CLASSIFICATION OF MEDICAL THERMAL IMAGES” has been prepared in accordance with the Thesis Writing Guidelines of the Abdullah Gül University, Graduate School of Engineering & Science.

Prepared By
Ahmet ÖZDİL

Advisor
Prof.Dr. Bülent YILMAZ

Head of the Electrical and Computer Engineering Program
Assoc. Prof. Kutay İÇÖZ

ACCEPTANCE AND APPROVAL

Ph.D. thesis titled “AUTOMATED PROCESSING AND CLASSIFICATION OF MEDICAL THERMAL IMAGES” and prepared by Ahmet ÖZDİL has been accepted by the jury in the Electrical and Computer Engineering Graduate Program at Abdullah Gül University, Graduate School of Engineering & Science.

23 /06 / 2022

(Thesis Defense Exam Date)

JURY:

Advisor : Prof. Dr. Bülent YILMAZ

Member : Assoc. Prof. Zafer AYDIN

Member : Prof Dr. Mustafa Ersel KAMAŞAK

Member : Assist. Prof. Kasım TAŞDEMİR

Member : Assist. Prof. Özkan Ufuk NALBANTOĞLU

APPROVAL:

The acceptance of this Ph.D. thesis has been approved by the decision of the Abdullah Gül University, Graduate School of Engineering & Science, Executive Board dated /..... / and numbered

..... /..... /

(Date)

Graduate School Dean
Prof. Dr. İrfan ALAN

ABSTRACT

AUTOMATED PROCESSING AND CLASSIFICATION OF
MEDICAL THERMAL IMAGES

Ahmet ÖZDİL

Ph.D. in Electrical and Computer Engineering

Advisor: Prof. Dr. Bülent YILMAZ

June 2022

The aim of this dissertation is to develop computer aided methods for processing and evaluating medical infrared thermal images. Throughout this study three problems were evaluated. The first problem was to automatically classify the body part and pose in the thermal images. In this study there were four classes; upper-lower body parts with back-front views. The first step included the segmentation of the background with Otsu's thresholding method applying histogram equalization. Next, DarkNet-19 architecture was used to extract features from images and these features were reduced using PCA and t-SNE methods. Finally reduced feature sets were used for classification. The second problem was to automatically classify liver steatosis from using thermal images. In this study, the classification problem was tested on an anatomical region of interest from abdominal images corresponding to the liver. Deep learning and texture analysis methods were employed for feature extraction, and then the selected feature sets were used for classification. The third problem was to quantify thermograms of multiple sclerosis (MS) patients for better assessment of the disease and monitoring the therapy. Thermal images of two patients and a healthy control from lower limbs were evaluated during experiments, and localized quantification of the effect of MS on the feet of the patients using thermal images method was proposed. The proposed method was fully correlated with the evaluations of physician. It is shown that medical thermal imaging has high potential in many fields of medicine as a non-invasive method for pre-diagnosis and follow-up.

Keywords: Medical infrared thermal imaging, Machine learning, Deep learning, Classification, Image processing

ÖZET

MEDİKAL TERMAL GÖRÜNTÜLERİN OTOMATİK OLARAK İŞLENMESİ VE SINIFLANDIRILMASI

Ahmet ÖZDİL

Elektrik ve Bilgisayar Mühendisliği Anabilim Dalı Doktora

Tez Yöneticisi: Prof. Dr. Bülent YILMAZ

Haziran-2022

Bu tezin amacı, tıbbi kızılötesi termal görüntülerin işlenmesi ve değerlendirilmesi için bilgisayar destekli yöntemler geliştirmektir. Bu çalışma boyunca üç problem değerlendirilmiştir. İlk problem, termal görüntülerde vücut kısımlarını ve pozunu otomatik olarak sınıflandırmaktır. Bu çalışmada, arka-ön ve üst-alt vücut görünüşleri olan dört sınıf vardı. İlk adımda, Otsu'nun yöntemiyle arka plan ayrıldı ve histogram eşitleme uygulandı. Daha sonra, görüntülerden öznelik çıkarmak için DarkNet-19 mimarisi kullanıldı ve bu öznelikler PCA ve t-SNE yöntemleri kullanılarak azaltıldı. Son olarak, sınıflandırma için indirgenmiş öznelik kümeleri kullanıldı. Üzerinde çalışılan ikinci problem, karaciğer yağlanmasını termal görüntüler kullanarak otomatik olarak sınıflandırmaktır. Bu çalışmada abdominal görüntülerden anatomik bir ilgi alanı bölütlenmiş, bu alandan öznelikler çıkarılmıştır. Öznelik çıkarımı esnasında derin öğrenme ve doku analizi yöntemleri kullanılmış, seçilen en uygun öznelikler sınıflandırmada. Son olarak bu tezde, multipl skleroz (MS) hastalarının tedaviye yanıt seyrini değerlendirmede kullanılmak üzere termogramların yerel nicelleştirilmesine dair bir yöntem önerisi yapıldı. Deneyler sırasında iki MS hastasının ve bir sağlıklı bireyin bacak termal görüntüleri değerlendirildi. Önerilen yöntemin sonuçları, hekimin değerlendirmeleri ile tam olarak uyuşmaktadır. Bu tezde, tıbbi termal görüntülemenin invaziv olmayan bir yöntem olarak ön tanı ve takip için farklı alanlarda yüksek potansiyele sahip olduğu gösterilmiştir.

Anahtar kelimeler: Medikal infrared termal görüntüleme, Makine öğrenmesi, Derin öğrenme, Sınıflandırma, Görüntü işleme

Acknowledgements

First of all, I would like to express my deepest gratitude to my advisor Prof. Bülent YILMAZ for his helpful advice and valuable assistance throughout the doctoral study. I am eternally grateful for his endless patience, support, encouragement, and valor.

I would like to give special thank you to Dr. Mustafa Mücahit YILMAZ who helped me to carry out this thesis. I am most grateful for the opportunity he gave me to work together, and also for his valuable comments and useful discussions.

With the same level of gratitude, I would also like to thank Assoc. Prof. Zafer AYDIN, who was a member of my thesis committee throughout this thesis, for his valuable comments and understanding.

I am also grateful to the committee member, Prof. Mustafa Ersel KAMAŞAK. Thank you for your time and valuable comments.

I would also like to thank all my colleagues who directly and indirectly help me for their unlimited support and encouragement.

Finally, I owe a deep gratitude to everyone who supported and encouraged me in my private life. I am especially grateful to my family for their endless support throughout my life.

TABLE OF CONTENTS

INTRODUCTION	1
1.1. LITERATURE OVERVIEW	4
BACKGROUND	8
2.1. INFRARED RADIATION	8
2.2. THERMAL IMAGING CAMERA	9
2.3. PREPROCESSING OF IMAGES.....	13
2.3.1. <i>Otsu's Thresholding Method</i>	13
2.3.2. <i>Histogram Equalization</i>	16
2.4. MACHINE LEARNING	19
2.4.1. <i>Batch vs. Online Learning</i>	20
2.4.2. <i>Instance-Based vs. Model-Based Learning</i>	20
2.4.3. <i>Test and Validation</i>	21
2.4.4. <i>Supervised vs. Unsupervised Learning</i>	21
2.4.5. <i>Classification Performance Assessment</i>	22
2.4.6. <i>Classification Models</i>	25
2.4.7. <i>Deep Learning</i>	25
2.4.8. <i>Convolutional Neural Networks</i>	27
2.4.9. <i>Weka</i>	28
2.5. DATA SET	31
AUTOMATIC BODY PART AND POSE DETECTION IN MEDICAL INFRARED THERMAL IMAGES	33
3.1. MATERIALS AND METHODS.....	35
3.1.1. <i>Thermal Images</i>	35
3.1.2. <i>Background Extraction with Blue Component of Image</i>	35
3.1.3. <i>Background Extraction with K-Means Clustering</i>	37
3.1.4. <i>Background Extraction with Thresholding</i>	38
3.1.5. <i>Preprocessing of Thermal Images</i>	39
3.1.6. <i>Feature Extraction and Selection</i>	39
3.1.7. <i>Classification: Pose Detection</i>	40

3.2. RESULTS	42
3.3. DISCUSSION AND CONCLUSIONS	48
MEDICAL INFRARED THERMAL IMAGE BASED FATTY LIVER CLASSIFICATION USING MACHINE AND DEEP LEARNING.....	50
4.1. MATERIALS AND METHODS	52
4.1.1. <i>Pre-Processing of Thermal Images</i>	53
4.1.2. <i>Image Datasets</i>	54
4.1.3. <i>Feature Extraction and Selection of Thermal Images</i>	55
4.1.4. <i>Classification</i>	56
4.2. RESULTS	57
4.3. DISCUSSION AND CONCLUSIONS	61
LOCALIZED QUANTIFICATION OF MEDICAL INFRARED THERMAL IMAGES FOR MULTIPLE SCLEROSIS ASSESSMENT AND MONITORING	65
5.1. MATERIALS AND METHODS	66
5.1.1. <i>Thermal Images</i>	66
5.1.2. <i>Processing of Thermal Images</i>	67
5.2. RESULTS	68
5.3. DISCUSSION AND CONCLUSIONS	74
CONCLUSIONS AND FUTURE PROSPECTS	79
6.1. CONCLUSIONS	79
6.2. SOCIETAL IMPACT AND CONTRIBUTION TO GLOBAL SUSTAINABILITY	80
6.3. FUTURE PROSPECTS	81

LIST OF FIGURES

Figure 2.1 Thermal image and visible light image	10
Figure 2.2 FLIR A35 FOV 69 (30 Hz, ver. 2017) thermal camera	11
Figure 2.3 Different types of thermal image display	11
Figure 2.4 How thermal imaging cameras can see through smoke	12
Figure 2.5 Thermal reflection from glass	13
Figure 2.6 Histogram equalization.....	18
Figure 2.7 Histogram equalization of thermal gray-level images	19
Figure 2.8 Precision vs recall tradeoff.....	24
Figure 2.9 Receiver operating characteristic (ROC) curve.....	24
Figure 2.10 Deep learning within artificial intelligence	26
Figure 2.11 Multiple layers of human cortex	26
Figure 2.12 Logical operations of ANNs.....	27
Figure 2.13 Architecture of LeNet-5	27
Figure 2.14 CNN layers consist of rectangular local receptive fields	28
Figure 2.15 Weka GUI Chooser screen	30
Figure 2.16 Medcore IRIS-XP medical infrared thermography system.....	31
Figure 2.17 Sample raw thermal images from our database.....	32
Figure 3.1 Sample for non-standard images	35
Figure 3.2 Blue component result on standard image (a: RGB image, b: Red component of RGB image, c: Green component of RGB image, d: Blue component of RGB image, e: Blue component edges interconnected)	36
Figure 3.3 Blue component result on non-standard image (a: Non-standard RGB image, b: Non-standard RGB image blue component, c: Non-standard image blue component edges interconnected).....	37
Figure 3.4 Results using k-means clustering approach to extraction the foreground (a & d are original RGB images, b & e are temperatures, c & f are extracted body images).	37
Figure 3.5 Results for background thresholding (a & e: original RGB images, b & f: temperatures, c & g: level thresholding results, and d & h: Otsu's thresholding results).....	38
Figure 3.6 Evaluation of segmentation methods	42

Figure 3.7 Application of ROI mask generated using Otsu’s thresholding method on thermal images.....	43
Figure 3.8 The results of histogram equalization (HE) method with and without focusing on the body parts as the ROI The first column: original image, second column: HE applied on the whole image, third column: HE applied on the whole masked image, and the fourth column: HE applied only within the ROI.....	44
Figure 3.9 PCA and t-SNE results on the first, second, third, and fourth image subsets.	46
Figure 3.10 A visual explanation of the resemblance of the back and front views of the lower part of the body. Lower part back view is shown on the first row, and lower part front view on the second row.	46
Figure 3.11 Summary of the classification accuracies for the best performing approaches on 4 different image subsets.	48
Figure 4.1 Upper front view of thermal images and the corresponding liver regions selected manually.....	53
Figure 4.2 Pre-processing of images a: original image, b: foreground mask, c: HE applied only within the body, and d: ROI corresponding to the liver of the patient.	55
Figure 4.3 Upper triangular ROI used in Dataset 3.	55
Figure 4.4 Classification accuracy of MCC classifier in which the features were extracted using Inception Resnet V2 extractor and selected by PCA (1 to 148 features).....	58
Figure 5.1 Extracting legs and feet from an IRT image from the first visit of the first patient (front view)	68
Figure 5.2 Automatic thresholding results (Patient 1, first row: visit 1, second row: visit 3).....	69
Figure 5.3 Colored thermal images of the three visits of patient 1 (a-b-c and g-h-i right leg images of three visits from front and back view respectively, d-e-f and j-k-l left leg images of three visits from front and back view respectively)	70
Figure 5.4 Colored thermal images of the four visits of patient 2 (a-b-c-d and i-j-k-l right leg images of four visits from front and back view respectively, e-f-g-h and m-n-o-p left leg images of four visits from front and back view respectively)	71
Figure 5.5 A sample image is presented to show how the dividing image into subregions and blocks is performed (Patient 1, visit 1, right leg, front view)	71
Figure 5.6 Patient 1, right foot images acquired during different visits (a: visit 1, b: visit 2, and c: visit 3).....	72

Figure 5.7 Comparison of mean gray levels corresponding to 9 blocks of the right and left feet for MS patients and healthy control from front view during different visits... 73



LIST OF TABLES

Table 2.1 Light comparison	8
Table 2.2 Confusion matrix structure	23
Table 3.2 DarkNet-19 architecture.	40
Table 3.3 Classifiers list employed during evaluations	41
Table 3.4 Performance metrics for different classification methods on different image subsets.....	47
Table 4.1 Classifiers list employed during evaluations	57
Table 4.2 Summary of the classification attempts those with the highest performances.	59
Table 4.3 Abbreviations of classification methods.....	59
Table 5.1 Differences of block-mean vectors for the right feet.....	74
Table 5.2 Differences of block-mean vectors for the left feet	74

LIST OF ABBREVIATIONS

ANNs	Artificial Neural Networks
ARFF	Attribute-Relation File Format
aTPR	Average True Positive Rate
AUC	Area Under Curve
BLR	Bayesian Logistic Regression
BMI	Body Mass Index
CDF	Cumulative Distribution Function
CNN	Convolutional Neural Networks
CNS	Central Nervous System
CS	Chronic Sinusitis
CSF	Cerebrospinal Fluid
CSV	Comma Separated Values
CT	Computed Tomography
DBNs	Deep Belief Networks
EHz	Exa Hertz
ENMG	Electroneuromyography
EST	Elevated Skin Temperature
EMR	Electromagnetic Radiation
eV	Electron Volt
FN	False Negative
FP	False Positive
FPR	False Positive Rate
GHz	Giga Hertz
GLCM	Gray Level Co-Occurrence Matrix
GLV	Gray Level Intensity Values
GMM	Gaussian Mixture Model
HE	Histogram Equalization
HOG	Histogram of Oriented Gradients
Hz	Hertz
IB1	Instance Based 1 Nearest Neighbor

IR	Infrared
IRT	Infrared Thermography
KMC	K-Means Clustering
k-NN	K Nearest Neighbors
keV	Kilo Electron Volt
meV	Milli Electron Volt
MHz	Mega Hertz
MR	Magnetic Resonance
MRI	Magnetic Resonance Imaging
MS	Multiple sclerosis
MITI	Medical Infrared Thermal Imaging
NAFLD	Non-Alcoholic Fatty Liver Disease
NETD	Noise Equivalent Temperature Difference
nm	Nano Meters
NN	Neural Network
OVA	One Versus All
OVO	One Versus One
PCA	Principal Component Analysis
PDF	Probability Density Function
PHz	Peta Hertz
RaF	Random Forest
RBM	Restricted Boltzmann Machines
REPTree	Reduced Error Pruning Tree
RGB	Red Green Blue
ROC	Receiver Operating Characteristic
RoF	Rotation Forest
ROI	Region of Interest
SMO	Sequential Minimal Optimization
SVM	Support Vector Machines
t-SNE	t-Distributed Stochastic Neighbor Embedding
TN	True Negative
TNR	True Negative Rate
TP	True Positive

TPR	True Positive Rate
THz	Tera Hertz
TP	True Positive
US	Ultrasonography
Weka	Waikato Environment for Knowledge Analysis
YOLO	You Only Look Once
μeV	Micro Electron Volt
μm	Micro Meter
$^{\circ}\text{C}$	Degree Celsius
$^{\circ}\text{F}$	Degree Fahrenheit





To my family

Chapter 1

Introduction

The homeothermic structure of the human body balances the thermal distribution using the different systems built into it. These different systems can be perspiration-evaporation, thermal conduction, forced and natural convection, exhalation, and infrared (IR) radiation to discharge the heat where vital activities produce [1]. Temperature differences of core or skin surface depict potential/emerging complications/diseases originating from anabolism or metabolism. This means that health problems that occur in the body can disrupt the heat balance locally or in general.

Infrared (IR) thermography is an imaging method that displays the heat distribution map of the target as an image to reveal detected abnormalities by evaluating temperature changes in the body. An IR thermogram is an image that displays the heat distribution – heat map of the target. The relationship of body heat balance and illness was first documented in 400 BC [2]. R. Lawson, in the year 1956, applied this technique on breast tumors in healthcare for the first time in literature. He found out that the surface temperature of the skin over a tumor tissue increased more than the skin over the normal tissue did. There, the focus was breast cancer detection. However, this technique gained interest after 1995 due to improvements in IR camera technology and image processing algorithms [1]. Diseases such as cancer, nerve blockage, vascular problems, upper respiratory tract infection, hernia, skeletal system abnormalities (such as scoliosis), abnormal thyroid activity, liver-spleen-stomach disorders and intestinal problems can cause heat imbalance in various body regions and organs and their thermal reflections may occur on body surface. Therefore, it has been shown that IR thermography can be used not only for breast tumor screening but also for various kinds of abnormalities such as the inflammatory arthritis, osteoarthritis, soft tissue rheumatism, tennis elbow, fibromyalgia, complex regional pain syndrome, peripheral circulation, and fever [3]. As the interest of medical experts turn on to IR thermography, they expose different application fields. In [4], breathing cycle and cardiac pulse wave monitoring was performed. In Mercer et al.'s autologous transplantation work, thermal imaging was used

to monitor the vessels to find out which one feeds the tissue and monitor compliance after transplantation [5]. IR thermography has not only been applied on human subjects but also on animals, many different studies have been conducted on horses or other athletic animals to monitor injuries and inflammatory responses [6]–[9].

Currently, researchers or physicians perform the analysis and evaluation of thermograms by visual inspection. Due to fast improvement in image processing techniques, it became possible to apply machine and deep learning techniques to various kind of fields. Exploring automatic processing and evaluation of thermograms by using newly developed methods will open new avenues to researchers in this field to apply IR thermography to unstudied fields, and thus more complex problems will be handled.

When body heat map is generated, thermal differences should be examined throughout the body surface. Even minor differences of temperature on the body surface may be significant indicators for diverse spectrum of diseases beneath that area, therefore slight temperature changes should also be evaluated during the examination of patients [3]. Applying medical IR thermal imaging (MITI) in clinical practice for diagnosing or monitoring has been evaluated by many researchers. While integrating this tool to medicine, the first aim has been to apply this imaging modality as a pre-diagnosis/interpretation tool, and by doing so, many clinics around the world have been using MITI as an integral part of their diagnosis process (maybe not the only tool). Since the number of professional physicians working with MITI is highly limited, it is imperative to develop new approaches and tools to help the experienced physicians in their efforts and even for the novice ones. MITI is a simple imaging approach that does not cause radiation-related risks, does not deteriorate the comfort of the patient, does not take long time, and is cheaper than the existing approaches such as magnetic resonance imaging (MRI) and computed tomography (CT) that will help the physician during the pre-diagnosis and screening of these diseases. In order to promote the use of this method there is a need for automated approaches that has high precision and is handy for the screening and diagnosis of different diseases.

Many studies are focused only on one disease and have limited number of samples to be used in the test phase. Dr. M.M. Yılmaz Clinic is one of the largest integrative medicine clinics and is the first clinic that uses the thermography vastly for pre-diagnosis and screening of many diseases in Türkiye. In this clinic, nearly 4000 patients have been examined with IR thermography since 2012. Development of an automated system which

aims at transferring the experience of a field expert, Dr. M.M. Yılmaz who has dealt with numerous cases with thermographs so far, is one of the goals of this thesis work.

The implementation of the imaging process should be demonstrated to provide a better understanding of the MITI. A controlled environment should be prepared while obtaining thermal images of a patient, because it is important to achieve better heat maps [10]. Patients should settle down before the image capturing begins by resting for a while in a controlled room. Safety measures should be considered to stabilize the conditions which are effective on changing the thermal conditions of the room. The dresses over the body are a hindrance which prevents the infrared camera from sensing the infrared radiations emitted from the body. Therefore, patients should be disrobed during the image acquisition phase. The next step is to reevaluation of the camera position in accordance with the height and position of patient. The first images taken when patient stand still facing the camera, then the patient is asked to turn 90 and/or 180 degrees around his/her axis, and then, if necessary, raise his/her arms to show the armpits. Another action to be taken is to lower the altitude of the camera position to facilitate the capturing images of legs and feet. Fifteen to twenty images are acquired from each patient during every visit, and stored in a database predominantly without any labelling of disease or sufficient physical information. Searching through a database like this for any images with specific disease related diagnostic labels is not possible for now. This process is done manually which means for the pre-diagnosis phase the physician should go over the images one by one, adjust color maps manually and focus on specific regions/parts of the body visually.

The IR thermograms may include and represent various signs about the health status of different body parts of a patient. However, interpreting them depends highly on the experience of the doctor examining the medical thermal images. Since the number of experienced physicians is limited in this area, it would be highly beneficial to improve methods to process and classify thermograms automatically. This will also help novice doctors or technicians to interpret them more accurately. In this study, medical thermograms will automatically be processed and classified to offer physicians a computer-aided diagnosis opportunity or a tool for pre-screening and diagnosing different types of diseases. This thesis work specifically focusses on the development of new approaches to automatically detect body parts and pose on a custom database of IR thermograms and detect and classify liver steatosis and multiple sclerosis (MS) diseases. The studies on these problems using thermal imaging are scarce or do not exist, and pre-

diagnosing by automated processing and classification methods have not yet been implemented.

1.1. Literature Overview

Quantitative thermal image analysis is a recent topic which awaits to be explored and there should be a full collaboration with thermal physiology of body beneath the skin and of course quantitative analysis will increase the objectiveness of the interpretation of thermogram [11], [12]. Therefore, recently in literature, automatic processing of thermal images has emerged as a new field. In this new field, automatic image thresholding, region-of-interest (ROI) extraction, classification, and remote sensing methods have been focused in many different studies [13]–[28]. Deep learning (Convolutional Neural Networks, CNN) and conventional machine learning (Support Vector Machines, SVM) methods have been employed for automatization. However, these types of studies/methods typically need organized data, and it is necessary to pre-process and/or preparation or selection of the images manually. If the intent is to develop a fully automatic system, manual intervention should be at minimal level. Determination of the body part (upper or lower) and orientation of the patient (anterior or posterior pose) on each thermal image is currently done by the physician him/herself manually. However, while generating dataset to perform image processing and automatic classification, the physician should determine what kind of disease the image contains. In the literature, researchers have done this selection process manually. Unfortunately, automatic body part and pose determination on thermal images has not been studied so far.

Since the first application of thermal imaging in medicine is breast tumor monitoring, broad amount of MITI studies focus on breast screening [18], [20], [29]–[41]. In [42], the sleeping position as lateral and supine of the head and body separately studied and deep learning methods were used for estimation. In this study, 92% level of accuracy was attained by employing a pre-trained CNN architecture called DarkNet-19. In [43], Kakileti et al. studied that comparison of semantic segmentation performance of different CNN architectures and found that the encoder-decoder architectures had better performance than the other architectures did. In [44], Bayesian based Gaussian Mixture Model (GMM) approach was proposed for segmenting and semi-supervised classification of image data, however in [45] a deterministic approach was used for data segmentation. Exercise-induced fatigue detection was studied by Lopez et al. [46], by processing

thermal images using CNN approach with an accuracy over 80%. In [47], a protocol is offered to detect people affected from severe acute respiratory syndrome (SARS) with abnormal physiological temperature.

Different machine learning algorithms were evaluated on plantar feet thermal images for diabetic foot ulcer identification and k-nearest neighborhood (k-NN) with 5 neighbors achieved 81.25% accuracy in [48]. Two different skin cancer tumors were classified using SVM in [49]. Histogram of oriented gradients (HOG) and random forest classifier methods were employed in another study [50] on thermal images for predicting hemodynamic shock. In [51], comparable results were achieved against the standard methods while testing the effect of MITI for diagnosing cardiovascular disease, and MITI was better when combined with standard methods in a computer aided diagnosis system. As an additional topic for MITI studies so far, assessment of hypertension was carried out in [52], they evaluated different pre-processing methods, and 89% accuracy was achieved by backpropagation neural network classifier.

In [53], the symmetry of dorsal view of body is studied in which the researchers selected a trapezoidal region of interest (ROI), and extracted 5 features such as the histogram correlation coefficient (HCC), image similarity coefficient (ISC), difference of mean gradient vector angle (DMGVA), dorsal-ventral (DV) index, and the absolute difference of standard deviation (DSTD). For data preprocessing they used normalization and digitization. The classifier was probabilistic RAM (pRAM) neural network, consisted of eight-input pRAMs (or 8-PRAMS). There were two hidden layers and one output layer placed in a pyramidal structure. They achieved noticeable classification accuracy results compared to the linear Fisher algorithm. In [54], necrotizing enterocolitis (NEC) in newborns was detected using abdominal thermal images with a new approach. They extracted a rectangular area over the umbilical stump, and denoised the ROI using non-local means denoising algorithm by considering the Gaussian noise. After denoising, they subdivided the ROI horizontally and vertically to obtain identical small areas. The mean of values of underlying pixels in the small area was calculated and set to be the small area value. They computed the mean, median, standard deviation (SD), median absolute deviation (MAD), interquartile range (IQR), total sum of squares (TSS), kurtosis, and the skewness. They had 80 normal and 84 NEC images. In addition, hypo and hyperthyroid disorder was detected using the Bayesian classifier by Mahajan and Madhe [55]. They classified the hypothyroid, hyperthyroid, and normal people with 81.81% accuracy, but their specificity was 100%. On the other hand, different skin problems can be examined

with thermography. In [15], the researchers used multispectral and thermal cameras to examine the acne vulgaris disease. Their aim was to develop a better imaging modality and image acquisition setup for acquiring as much information from the patient as possible. They used homomorphic filtering to eliminate non-uniform illumination, but this was not enough to produce a uniform image. Therefore, they put their effort to develop a better image acquisition modality. They used multispectral camera to eliminate unwanted wavelengths and used only those wavelengths in which the reflectance of the lesions was high. According to their hypothesis (based on similar theory) details of an acne lesion could be extracted at certain wavelengths that showed a high reflectivity. They planned to reduce features to two-dimensions (2D) by applying the PCA approach on three-dimensional (3D) hyper-spectral images. They used thermal images to find out whether a pixel was on a scar or on an inflammatory lesion. Another study was performed on skin burns [56] in which the authors classified light/severe burns using thermal images with standard classifiers and convolutional neural network. Nhan and Chau extracted features from the thermal infrared images to classify affective states of an individual with a genetic algorithm [57]. However, still the most popular area of thermal imaging in medicine is breast cancer screening.

Backache is studied in the literature, and different approaches have been investigated. In [53], the back thermograms of 120 HIV patients with Kaposi's sarcoma are used to do a symmetry classification with pRAM neural network classifier. However, in [58] and [59], thermal imaging was used as the outcome measure, or in [60] thermogram was used to diagnose and find out the location spot of spine-related disease in horses manually. A dorsal view image can give information about hernia, pain centers, and activation of acupuncture centers. Acupuncture center activation can be observed throughout the whole body as well.

Sinus inflammation detection using IR thermograms is rarely studied in the literature. In [61], acute maxillary rhinosinusitis detection with IR thermograms was studied, and they stated that the IR thermogram was not a reliable diagnosis approach. However, inflammation makes a temperature effect [62], where their starting point is different from the study in [61]. Kalaiarasi et al. studied chronic sinusitis (CS), and tested IR thermogram usage for diagnosing the CS. They acquired promising results that the IR thermogram can be beneficial for sinuses that are close to the body surface [62].

Varicose is a disorder of blood flow, which makes it easier for IR imaging to detect. Blood flow has direct heat impact on body surface, and the vessels close to the skin are

easily detected if there is varicose due to slow blood flow [63]. In the literature there are different studies for diagnosing or investigating varicose [63], [64]. Bagavathiappan et al. investigated and found out correlation between thermal images and clinical findings on 3 patients who have similar histories as prolonged standing [63][31]. In [64], an automatic system was designed to extract ROI for suspicious varicose vein areas.

In [65], the classification performances of different sets of features were evaluated through support vector machines (SVM), which generated from breast infrared (IR) thermal images. Promising results were found which include the performance comparison of MITI and traditional techniques on screening cardiovascular disease [51]. In [66], IR images of both iris were used for diagnosing type-2 diabetes. In [67], they developed a treatment decision system to determine the most effective treatment method for patient by monitoring the wounds via MITI. A review of studies performed on different diseases can be found in [68].

An infrared camera can be integrated into another monitoring system to increase the performance of the system. In [69], an instant stress detection model was developed and a smartphone camera-based photoplethysmography (PPG) and a low-cost thermal camera were employed together. In [70], SVM was applied on thermal images for recognition of facial expressions.

Chapter 2

Background

2.1. Infrared Radiation

Infrared (IR) is electromagnetic radiation (EMR) and its wavelength is longer than visible lights. Because of this, IR is invisible for human eye. Astronomer Sir William Herschel discovered infrared radiation in 1800. Herschel's studies presented that a little more than half portion of the energy from the sun land on Earth in the form of infrared. The climate of Earth was shaped by the absorbed and emitted infrared radiation.

Rotational and vibrational movements of molecules cause emission or absorption of infrared radiation. Infrared radiation has many different application areas such as industrial, scientific, military, commercial, and medical applications. Detecting heat loss in isolated systems, monitoring temperature change over body skin surface, detecting overheat in the electrical components are carried out by employing infrared thermal-imaging cameras. Target acquisition, surveillance, night vision, homing, and tracking are included by military and non-military use of infrared radiation. Non-military uses include thermal performance analysis, environmental monitoring, industrial facility investigation, detection of grow-ops, distant temperature sensing, short-range wireless communication, spectroscopy, and weather forecasting [71].

The spectrum of infrared radiation has no broadly accepted edges, but 700 nm to 1mm interval can be a trustworthy interval as shown in Table 2.1.

Table 2.1 Light comparison

Name	Wavelength	Frequency (Hz)	Photon energy (eV)
Gamma ray	less than 0.01 nm	more than 30 EHz	more than 124 keV
X-ray	0.01 nm – 10 nm	30 PHz – 30 EHz	124 keV – 124 eV
Ultraviolet	10 nm – 400 nm	750 THz – 30 PHz	124 eV – 3.3 eV
Visible	400 nm – 700 nm	430 THz – 750 THz	3.3 eV – 1.7 eV
Infrared	700 nm – 1 mm	300 GHz – 430 THz	1.7 eV – 1.24 meV
Microwave	1 mm – 1 meter	300 MHz – 300 GHz	1.24 meV – 1.24 μ eV
Radio	1 meter and more	300 MHz and below	1.24 μ eV and below

There are 5,780 kelvins (5,510 °C, 9,940 °F) of temperature throughout the sun surface and it is composed of near-thermal-spectrum radiation. At sea level there is over a kilowatt irradiance, consists of 527 watts infrared, 445 watts visible light, and 32 watts is ultraviolet radiation. This means nearly whole portion of infrared radiation from sunlight is near infrared.

Infrared radiation generally lies beyond the visible light wavelengths by human eye. Yet, infrared radiation is not totally invisible for human eye, where the human eye's sensitivity decreases immediately but smoothly above 700nm wavelength. This means longer wavelengths which are classified as infrared by usual definitions, can be seen if they are bright enough.

Infrared radiation is generally described as "heat radiation", still the surfaces become warmer when they absorb other waves like visible light or electromagnetic constituted from any frequency. Heating of the Earth is 49% met by infrared radiation from the sun and 51% met by the visible light which has longer wavelengths. At room temperature objects generally emit radiation around 8 to 25 μm band. This band interval is not so different from the visible light of incandescent objects' and ultraviolet of hotter objects. Heat is energy in a transitional state that flows due to a temperature difference. Thermal transmission types, thermal conduction and thermal convection cannot propagate through a vacuum like thermal radiation [72].

2.2. Thermal Imaging Camera

Thermal imaging camera generates an image by collecting infrared radiation like normal camera that collects visible light. Thermal imaging camera generates a heat map from collected infrared radiation as shown in Figure 2.1, the uppermost image was captured with thermal imaging camera and the below image was captured with normal camera from the same scene [73]. To be more specific, MITI system captures infrared radiation emitted from the surface of the object as temperature value of that relevant location and incorporate into the image as a pixel using infrared sensor arrays and generates a heatmap called thermogram. The temperature values in the thermal image are colored according to a selected color palette and the thermal image is converted to RGB image.

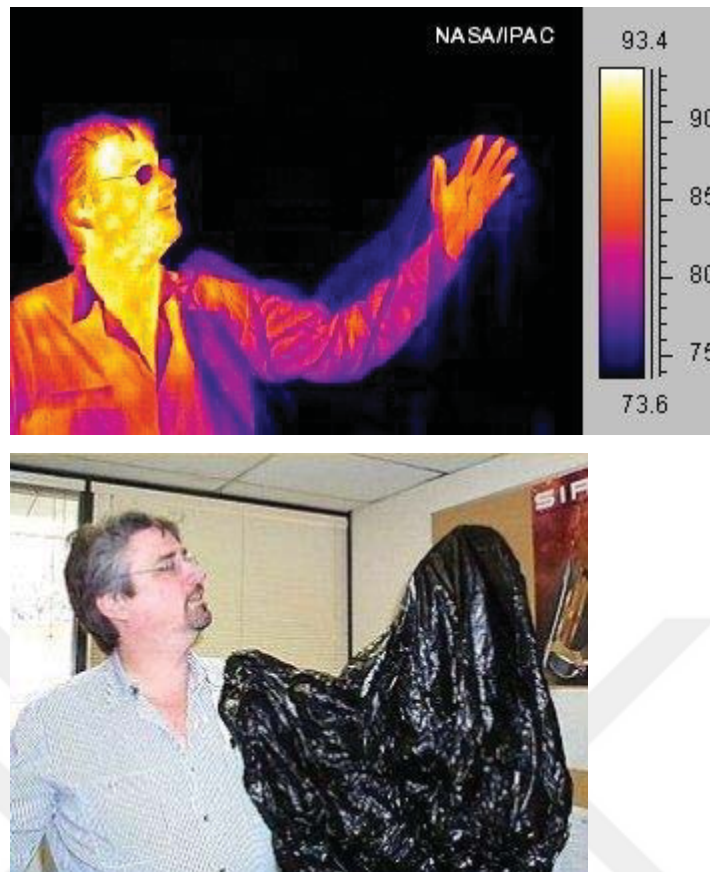


Figure 2.1 Thermal image and visible light image

Thermal camera's working principle is different on capturing mechanism, normal camera captures the visible light, but thermal imaging camera captures the infrared radiation emitted from objects due to heat. Infrared radiation has longer wavelength than visible light, $1\ \mu\text{m}$ to $14\ \mu\text{m}$. Longer wavelength causes decrease of the resolution of the image captured therefore image resolutions of thermal images ranges from 80×60 to 1280×1024 pixels. Since the wavelength is longer, the infrared sensors should be larger. As a result, thermal imaging cameras has lower resolution compared to visible light cameras with same mechanical size.

Figure 2.2, demonstrates a typical thermal imaging camera from Teledyne FLIR, with 320×256 resolution [74]. Thermal imaging cameras can detect about 0.01°C difference today, this sensitivity is good for medical applications.



Figure 2.2 FLIR A35 FOV 69 (30 Hz, ver. 2017) thermal camera

A thermal imaging camera consists of a lens, a thermal sensor, processing electronics, and a mechanical housing. The lens in the thermal imaging camera collects and focuses infrared radiation onto the sensor array. Thermal images captured by thermal imaging cameras can be displayed as shades of gray values or with different color palettes. In Figure 2.3, color palette and gray level thermal images can be seen. Gray level images can be arranged as white hot or black hot, which means the hottest area will be represented by white or black, in Figure 2.3, white hot gray level scale is used [75].

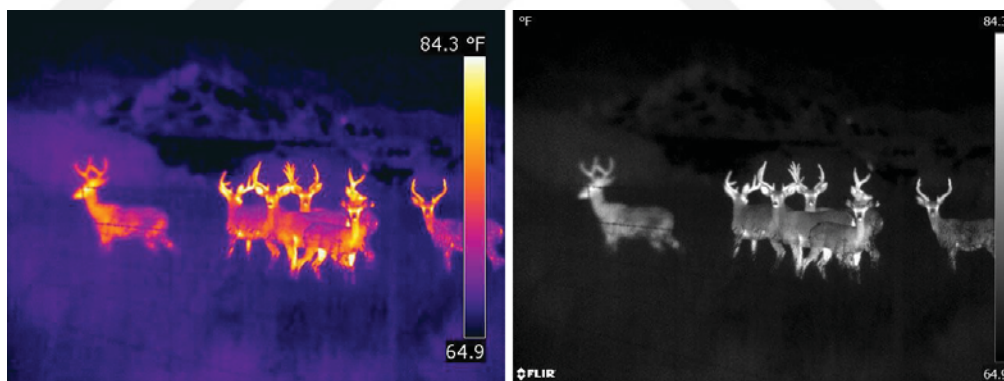


Figure 2.3 Different types of thermal image display

Thermal imaging cameras are built to answer different application areas. Originally, thermal imaging cameras were developed for surveillance and military operations, however today vast number of areas like building inspections (moisture, insulation, roofing, etc.), firefighting, autonomous vehicles and automatic braking, skin temperature screening, industrial inspections, scientific research, etc. Also, it is an effective tool to measure skin surface temperature and identify individuals with Elevated Skin Temperature (EST).

Since there are different application areas for thermal imaging camera there are different specifications for applicable for specific usage: range (the entire span of temperatures the camera is calibrated to scan), field of view (FOV) (determined by the camera lens, and is total of the scene that the camera will see), IR resolution (how many pixels the camera has on the scene), thermal sensitivity (Noise Equivalent Temperature Difference, NETD) (smallest temperature difference that the camera can detect), focus (focused distance in scene fixed, manual, or auto), spectral range (range sensitivity in the electromagnetic spectrum).

Another popular question about thermal imaging cameras is “what can thermal imaging camera see?”. Thermal imaging cameras cannot see through the concrete materials. However, they can see through smoke and in Figure 2.4 the image in the left was captured with visible light camera and the image on the right was captured with thermal imaging camera, and the man standing backward of the door can be seen in the image captured by thermal imaging camera [76]. The vision of thermal imaging camera decreases through fog or rain due to scattering of infrared radiation caused by rain droplets.



Figure 2.4 How thermal imaging cameras can see through smoke

Infrared radiation can be reflected from some surfaces like mirror or glass. Therefore, thermal imaging camera capture the reflection from that surface. In Figure 2.5, there is a glass between the thermal imaging camera and the scene in the image on the left side, and thermal imaging camera captures the reflection of the person who captures the image, not the scene [76]. Since thermal imaging camera captures the infrared radiation, it captures the reflected radiation from the glass surface.



Figure 2.5 Thermal reflection from glass

The first thermal camera was invented by Kálmán Tihanyi in 1929 named infrared-sensitive (night vision) electronic television camera for anti-aircraft defense in Britain [77]. However, civilian use of thermal camera was more possible towards to end of 1990s, due to dramatic decrease of the expenses.

Throughout this study different methods have been utilized for assessment during investigations. In this subject, utilized methods were described briefly.

2.3. Preprocessing of Images

2.3.1. Otsu's Thresholding Method

In image processing it is important to select a sufficient gray level threshold to discriminate objects from the background. Various techniques have been proposed on this subject so far. The threshold value can be chosen at the bottom of a deep and sharp valley between two peaks that represent objects and background in an ideal histogram. However, for most real pictures it is often difficult to pinpoint the valley floor; especially where the valley is flat and wide, full of noise, or where the heights of the two hills are extremely different and often do not produce a traceable valley.

Nobuyuki Otsu presented a nonparametric and unsupervised threshold selection approach for segmenting background from objects on digital images [78]. In order to maximize the separability of the classes obtained in gray levels, an optimal threshold is chosen by the discrimination criterion. In general, it uses the zeroth and first order cumulative moments of the gray level histogram. It is easy to extend the method to multi-threshold problems.

Otsu proposed that, since the "precision" of the threshold has not been evaluated in most of the methods proposed so far, it may be the right way to derive an optimal

thresholding method to establish a suitable criterion for evaluating the "precision" of the threshold from a more general point of view. Therefore, he investigated the choice of baseline threshold, for which only the gray-level histogram is sufficient without any other prior knowledge.

The formulation of the Otsu's method is as follows:

If the image consists of L gray levels $[1, 2, \dots, L]$, the number of pixels at level i is denoted by n_i and total number of pixels is $N = n_1 + n_2 + \dots + n_L$. The histogram is normalized and regarded as a probability distribution as depicted in equations (2.1):

$$p_i = \frac{n_i}{N}, \quad p_i \geq 0, \quad \sum_{i=1}^L p_i = 1 \quad (2.1)$$

Next, the pixels are divided into C_0 and C_1 classes (background and foreground respectively or vice versa) at a threshold gray level k , where C_0 covers $[1, 2, \dots, k]$ and C_1 covers $[k+1, \dots, L]$. Then, the probabilities of class occurrence and the class mean levels, respectively, are given by equations (2.2) to (2.7):

$$\omega_0 = \Pr(C_0) = \sum_{i=1}^k p_i = \omega(k) \quad (2.2)$$

$$\omega_1 = \Pr(C_1) = \sum_{i=k+1}^L p_i = 1 - \omega(k) \quad (2.3)$$

and

$$\mu_0 = \sum_{i=1}^k i \Pr(i|C_0) = \sum_{i=1}^k i p_i / \omega_0 = \mu(k) / \omega(k) \quad (2.4)$$

$$\mu_1 = \sum_{i=k+1}^L i \Pr(i|C_0) = \sum_{i=k+1}^L i p_i / \omega_1 = \frac{\mu_T - \mu(k)}{1 - \omega(k)} \quad (2.5)$$

where

$$\omega(k) = \sum_{i=1}^k p_i \quad (2.6)$$

and

$$\mu(k) = \sum_{i=1}^k i p_i \quad (2.7)$$

are the zeroth- and the first-order cumulative moments of the histogram up to the k th level, respectively, and

$$\mu_T = \mu(L) = \sum_{i=1}^L i p_i \quad (2.8)$$

is the total mean level of the original image. The relationship of the following can be verified for any choice of k:

$$\omega_0 \mu_0 + \omega_1 \mu_1 = \mu_T, \quad \omega_0 + \omega_1 = 1 \quad (2.9)$$

The class variances are found as follows:

$$\sigma_0^2 = \sum_{i=1}^k (i - \mu_0)^2 Pr(i|C_0) = \sum_{i=1}^k (i - \mu_0)^2 p_i / \omega_0 \quad (2.10)$$

$$\sigma_1^2 = \sum_{i=k+1}^L (i - \mu_1)^2 Pr(i|C_1) = \sum_{i=k+1}^L (i - \mu_1)^2 p_i / \omega_1 \quad (2.11)$$

Quadratic cumulative moments (statistics) are required for these calculations.

To assess the "goodness" of the threshold (at the k level), the following class separability measures used in discriminant analysis were introduced:

$$\lambda = \sigma_B^2 / \sigma_W^2, \quad K = \sigma_T^2 / \sigma_W^2, \quad \eta = \sigma_B^2 / \sigma_T^2, \quad (2.12)$$

where

$$\sigma_W^2 = \omega_0 \sigma_0^2 + \omega_1 \sigma_1^2 \quad (2.13)$$

$$\sigma_B^2 = \omega_0 (\mu_0 - \mu_T)^2 + \omega_1 (\mu_1 - \mu_T)^2 = \omega_0 \omega_1 (\mu_1 - \mu_0)^2 \quad (2.14)$$

(due to (2.9)) and

$$\sigma_T^2 = \sum_{i=1}^L (i - \mu_T)^2 p_i \quad (2.15)$$

are the within-class variance (equation (2.13)), between-class variance (equation (2.14)), and total variance of levels (equation (2.15)), respectively. Then the problem is to optimize the threshold k that maximizes one of the object functions in the equation (2.12).

This perspective is motivated by the assumption that classes with good thresholds will segregate at gray levels, and conversely, a threshold that gives the best separation of classes at gray levels will be the best threshold.

The discriminant criteria maximizing λ , K , and η , respectively, for k are, however, equivalent to one another; e.g., $K = \lambda + 1$ and $\eta = \lambda / (\lambda + 1)$ in terms of λ , because the following basic relation always holds:

$$\sigma_W^2 + \sigma_B^2 = \sigma_T^2 \quad (2.16)$$

When compared by the inclusion of the threshold level k , σ_W^2 and σ_B^2 are functions of threshold level k , but σ_T^2 is independent of k . Among σ_W^2 , σ_B^2 and η the simplest measure determined as η , because σ_W^2 and σ_B^2 based on second-order statistics (class variances) and the first-order statistics (class means), respectively. Thus, Otsu has chosen η as the criterion measure to determine the “goodness” of the threshold level k .

The optimal threshold k^* that maximizes η , or σ_B^2 , is selected in the following sequential search by using the simple cumulative quantities (2.6) and (2.7), or explicitly using (2.2)-(2.5):

$$\eta(k) = \sigma_B^2(k)/\sigma_T^2 \quad (2.17)$$

$$\sigma_B^2(k) = \frac{[\mu_T \omega(k) - \mu_K]^2}{\omega(k)[1 - \omega(k)]} \quad (2.18)$$

and the optimal threshold k^* is

$$\sigma_B^2(k^*) = \max_{1 \leq k < L} \sigma_B^2(k) \quad (2.19)$$

The k range for which the maximum is sought can be limited by the following formula:

$$S^* = \{k; \omega_0 \omega_1 = \omega(k)[1 - \omega(k)] > 0, \text{ or } 0 < \omega(k) < 1\}$$

This range can be called the effective range of the gray level histogram.

From the definition in (2.14), the criterion measure σ_B^2 (or η) takes a minimum value of zero for such k as $k \in S - S^* = \{k; \omega(k) = 0 \text{ or } 1\}$ (i.e., making all pixels either C_1 or C_0) and takes a positive and bounded value for $k \in S^*$. It is, therefore, obvious that the maximum always exists.

2.3.2. Histogram Equalization

Historically, the histogram equalization algorithm has been the preferred image enhancement algorithm because of its simplicity and efficiency. By changing the gray level of an image, it adjusts it according to the probability distribution function of the image, thereby magnifying the dynamic range of the gray-level distribution to make the image visually more understandable [79]. The histogram equalization algorithm performs the gray-level mapping of pixels in the image by processing gray level values based on

probability theory. Thus, it aims to improve the image by aiming its histogram to have uniform, smooth and clear gray levels.

In the original image, r is the gray-level value of a pixel in the original image, r is in the range $[0, L-1]$, where $r = 0$ represents black and $r = L-1$ represents white. Transformation can be done when r satisfied these conditions:

$$s = T(r) \quad 0 \leq r \leq L - 1 \quad (2.20)$$

where s is the gray-level intensity value of enhanced image. Assuming:

- a. $T(r)$ is monotonically increasing function within $0 \leq r \leq L - 1$,
- b. $0 \leq T(r) \leq L - 1$ for $0 \leq r \leq L - 1$

The inverse is:

$$r = T^{-1}(s) \quad 0 \leq s \leq L - 1, \quad (2.21)$$

in this case condition (a) will be changed to

- a'. $T(r)$ is a strictly monotonically increasing function within $0 \leq r \leq L - 1$,

the requirement that $T(r)$ in condition (a) increase monotonically ensures that the output density values will never be less than the corresponding input values, thus avoiding the artifacts produced by the intensity reversal.

The values within $[0, L-1]$ can be considered as random variables. Probability density function (PDF) is among the fundamental descriptors of a random variable. Consider, $p_r(r)$ and $p_s(s)$ are probability density functions of r and s , respectively, if $p_r(r)$ and $T(r)$ are known, and $T^{-1}(s)$ satisfies the condition (a) then $p_s(s)$ can be obtained using the following equation:

$$p_s(s) = p_r(r) \left| \frac{dr}{ds} \right| \quad (2.22)$$

The gray-level PDF of the input image and the chosen transformation function determines the PDF of s . A transform function of particular importance in image processing is as follows:

$$s = T(r) = \int_0^r p_r(\omega) d\omega \quad (2.23)$$

ω is dummy variable of integration. The right side of (2.23) is random variable r 's cumulative distribution function (CDF). At this point, both conditions (a) and (b) are satisfied. When $T(r)$ is given, the $p_s(s)$ can be calculated using (2.22). If Leibniz's rule is applied:

$$\frac{ds}{dr} = \frac{dT(r)}{dr} = \frac{d}{dr} \left[\int_0^r p_r(\omega) d\omega \right] = p_r(r) \quad (2.24)$$

when this result is applied to (2.22) leads to:

$$p_s(s) = p_r(r) \left| \frac{dr}{ds} \right| = p_r(r) \left| \frac{1}{p_r(r)} \right| = 1, \quad 0 \leq s \leq 1 \quad (2.25)$$

The probability of occurrence of a r_k gray-level in an image is estimated as follows:

$$p_r(r_k) = \frac{n_k}{n}, \quad k = 0, 1, 2, \dots, L - 1 \quad (2.26)$$

n is total number of pixels in the image, n_k is the number of pixels at gray level r_k , and L is the gray level range. If (2.23) is discretized:

$$s_k = T(r_k) = \sum_{j=0}^k p_r(r_j) = \sum_{j=0}^k \frac{n_j}{n}, \quad k = 0, 1, 2, \dots, L - 1 \quad (2.27)$$

Thus, by mapping pixels with level r_k to corresponding pixels with level s_k using (2.27) the output image is obtained. The transformation given in (2.27) is called histogram equalization or histogram linearization.

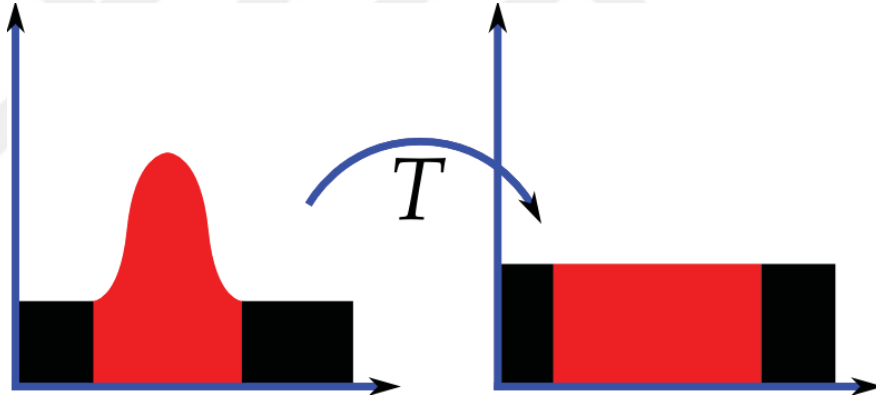


Figure 2.6 Histogram equalization

The effect of the histogram equalization on image histogram can be seen in Figure 2.6 [80]. The method justifies the histogram in a smooth manner.

Subject	Original image	HE applied on the original image
Male Upper Body Front View		
Male Lower Body Front View		

Figure 2.7 Histogram equalization of thermal gray-level images

In Figure 2.7, sample gray-level thermal images on the left column and their histogram equalized counterparts can be seen.

2.4. Machine Learning

Machine Learning (ML) is a science, but also it can be considered as an art, of programming computers so they can learn by processing the data [81]. Two definitions of machine learning are as follows: “[Machine Learning is the] field of study that gives computers the ability to learn without being explicitly programmed.” (Arthur Samuel, 1959). A more engineering-oriented definition is “A computer program is said to learn from experience E with respect to some task T and some performance measure P, if its performance on T, as measured by P, improves with experience E.” (Tom Mitchell, 1997).

For example, a spam filter uses a machine learning system which can learn to flag the given emails as spam, by assessing the already flagged emails by users. The already flagged email set is called as “training set”, which the machine learning system uses to learn how to flag emails. According to Tom Mitchell’s definition, flagging new emails is the task T, the experience E is the training data, and the performance measure P should be defined by system administrators; if you evaluate the ratio of correctly classified emails then this particular performance measure is called accuracy and it is often used in machine learning systems. Machine Learning can be used for:

- For solutions that require a lot of hand-tuning or long lists of rules,
- When a good solution cannot be found for complex problems by traditional approach,
- When there exist fluctuating environments,

- Assessing the large amount of data.

Machine Learning systems can be classified in broad categories based on (i) whether they are trained with supervision (supervised, unsupervised, semi-supervised, and reinforcement learning), (ii) whether they can learn instantaneously or incrementally (online versus batch learning), and (iii) whether they work by comparing new data points with known data points or detect patterns in training data, and generate a predictive model (instance-based versus model-based learning).

2.4.1. Batch vs. Online Learning

If the system cannot learn incrementally, it is called batch learning, because this system needs to be trained using all the available data. Therefore, using all the available data needs a lot of time and computational resources, so it is generally done offline. First the system is trained, and then it is started to be used and runs without learning anymore; it just applies what it has learned. This is called offline learning. If a batch learning system needs to know about new data, the system should be trained from scratch on the full dataset (both the new data and the old data), then the old system is replaced with the new one.

However, online learning system is trained incrementally with the data instances sequentially, either individually or by small groups called mini-batches. These learning steps are fast and cheap, so the system can be updated with new data simultaneously. Online learning is used when the data comes as a continuous flow and change should be done rapidly or autonomously. If the computing resources are limited, online learning is a good choice.

2.4.2. Instance-Based vs. Model-Based Learning

Generalization is the ability of the model that how the model enhance itself for new examples. Instance-based learning and model-based learning are the main generalization techniques.

Instance-based learning learns examples by repetition, after that uses a similarity measure to generalize the model for new cases. Another way to generalize from a set of examples is called model-based learning, which aims to build a model of these examples, then use that model for generalization.

2.4.3. Test and Validation

When a model is built, it should be tested on new samples to evaluate how well the model generalizes to new cases. One way to do this is to use the model in real practice and evaluate the performance, but if there are too many errors in the model, real users will certainly complain. The general solution is to split data into training and test sets, where model is trained on training set and the generalization performance is evaluated on test set.

If the error rate on the training set is low, but the error rate on test set (generalization error) is high, this means the model is overfitting the training data. On contrary, underfitting occurs when model is too simple to learn the training data, and the training error becomes too high.

2.4.4. Supervised vs. Unsupervised Learning

Supervision can be provided to ML systems while training, and can be categorized according to the amount and type of supervision. These are supervised learning, unsupervised learning, semi-supervised learning, and reinforcement learning.

Desired solutions are included into the training data in supervised learning, and these desired solutions are called labels. Classification is a typical supervised learning task. A spam filter is a good example for classification task. Some of the well-known supervised learning algorithms are k-Nearest Neighbors, Linear Regression, Logistic Regression, Support Vector Machines (SVMs), Decision Trees and Random Forests, and Neural Networks.

In unsupervised learning, the system tries to learn without a supervision, because the training data is unlabeled. Some of the most important unsupervised learning algorithms are the following:

- Clustering
 - K-Means
 - DBSCAN
 - Hierarchical Cluster Analysis (HCA)
- Anomaly detection and novelty detection
 - One-class SVM
 - Isolation Forest
- Visualization and dimensionality reduction

- Principal Component Analysis (PCA)
- Kernel PCA
- Locally-Linear Embedding (LLE)
- t-distributed Stochastic Neighbor Embedding (t-SNE)
- Association rule learning
 - Apriori
 - Eclat

Some problems include partially labeled training data which means a lot of unlabeled data and a little bit of labeled data. Machine learning methods that deals with partially labeled data is called semi-supervised learning. Unsupervised and supervised algorithms are incorporated to build semi-supervised learning algorithms. For example, deep belief networks (DBNs) are built with the combination of restricted Boltzmann machines (RBMs) stacked on top of one another where RBMs are trained in an unsupervised manner, and then the whole system is fine-tuned using supervised learning techniques.

Reinforcement learning is different from other types which has a learning system called an agent. The agent can observe the environment, select and perform actions, and get rewards in return (or penalties in the form of negative rewards). The system learns how to increase the earned reward by itself over time and develop strategies accordingly. These strategies are called policy and they mean what action will be taken in a given situation.

2.4.5. Classification Performance Assessment

While building classification models, assessing the performance of the model is another problem to tackle with. Because we must know the accuracy level of the model when it classified new samples. K-fold cross-validation is a frequently preferred method to evaluate a model. The main idea is to split data into K subsets, for K times one of the subsets is kept for testing and the rest for training, in the next step another subset is kept for testing and the rest are used for training. After K steps the results are averaged.

Another way to evaluate performance of the model is using confusion matrix. True and false classification numbers are placed in the confusion table. The structure of confusion matrix can be seen in Table 2.2. Rows corresponds to actual class and columns corresponds to predicted class.

Table 2.2 Confusion matrix structure

	Predicted Positive	Predicted Negative
Actual Positive	True Positive (TP)	False Negative (FN)
Actual Negative	False Positive (FP)	True Negative (TN)

Different performance metrics can be calculated using the confusion matrix. These performance metrics are different in characteristics and used as a measure for different types of applications. These metrics are error rate, accuracy, sensitivity (recall or true positive rate, TPR), specificity (true negative rate, TNR), false positive rate (FPR), precision (positive predicted value), negative predicted value, F1 score (harmonic mean of precision and recall) and can be calculated as follows:

$$\text{Error Rate} = \frac{(FP + FN)}{(TP + TN + FN + FP)} \quad (2.28)$$

$$\text{Precision} = \frac{TP}{(TP + FP)} \quad (2.29)$$

$$\text{Sensitivity (Recall)} = \frac{TP}{(TP + FN)} \quad (2.30)$$

$$\text{Specificity} = \frac{TN}{(TN + FP)} \quad (2.31)$$

$$\text{Negative Predict Value} = \frac{TN}{(TN + FN)} \quad (2.32)$$

$$\text{Accuracy} = \frac{(TP + TN)}{(TP + TN + FN + FP)} \quad (2.33)$$

$$\text{F1 score} = \frac{(2 * \text{Precision} * \text{Recall})}{(\text{Precision} + \text{Recall})} = \frac{TP}{TP + \frac{FN + FP}{2}} \quad (2.34)$$

$$\text{FPR} = \frac{FP}{(FP + TN)} \quad (2.35)$$

The precision is the accuracy of positive predictions, and it has a drawback when the model labels and ensures only one instance to be true and the rest is labeled false, then the precision is 100%, however, among the positive elements only one is found. Therefore, precision and recall are combined and F1 score metric is developed. F1 score is the harmonic mean of precision and recall. Since there is a tradeoff between precision and recall, F1 score balances this tradeoff. In Figure 2.8, the tradeoff between precision and recall metrics can be seen that precision really starts to fall sharply around 80% recall

[81]. Therefore, selecting a precision/recall tradeoff just before that drop, for example at around 60% recall, will be more effective, but of course the choice depends on the project.

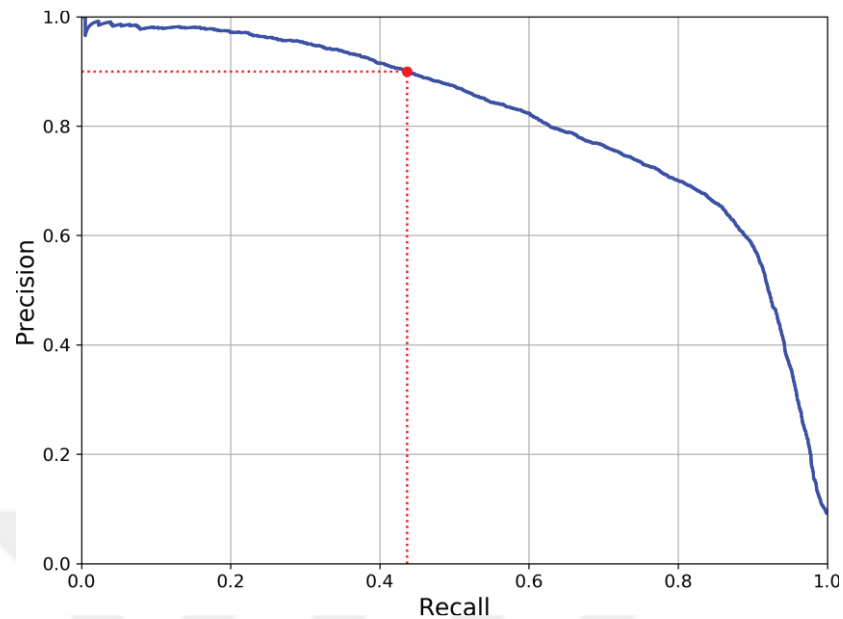


Figure 2.8 Precision vs recall tradeoff

The receiver operating characteristic (ROC) curve is another generalized metric used with binary classifiers. The ROC curve is the plot of the true positive rate (another name for recall) against the false positive rate (FPR). The FPR is equal to one minus the true negative rate. The TNR is also called specificity. Hence the ROC curve plots sensitivity (recall) versus $1 - \text{specificity}$.

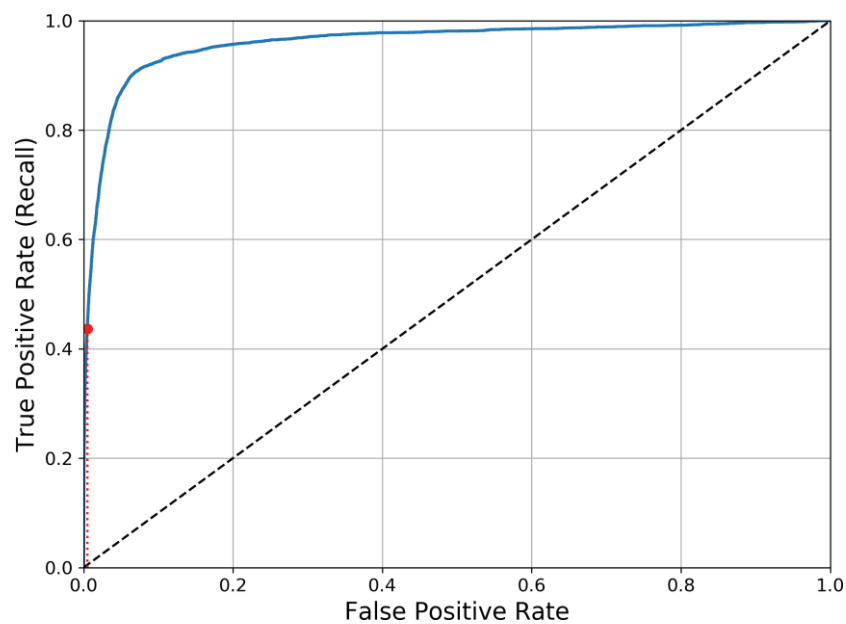


Figure 2.9 Receiver operating characteristic (ROC) curve

In Figure 2.9, a general ROC curve can be seen, and it can be observed that if TPR increases also FPR increases [81]. Generally, area-under-curve (AUC) of ROC is used for comparison of the performances of models.

2.4.6. Classification Models

Classification models can be divided by the number of classes they try to classify. If there are two classes like absence-existence of a disease, then the model is called binary classifier. If there are more than two classes, then the model is called multiclass classifier. Therefore, some classification algorithms can classify only two classes like support vector machines, where others can classify more than two classes like Bayes'.

However, there are different applications of binary classification algorithms to multiclass classification. If a binary classification algorithm is trained to detect one class and refuse others, and this is repeated by the number of classes, then multiple binary classifiers can classify multiclass classification problems. This strategy is called one-versus-all (OVA) or one-versus-the rest. Another strategy is classifying the classes in pairs. For example, if there are N classes in this strategy, classification is performed by distinguishing 1st class from 2nd class, then 1st class from 3rd class, 2nd class from 3rd class and continue to $(N-1)^{\text{th}}$ class to N^{th} class. This strategy is called one-versus-one (OVO) strategy. Therefore $N*(N-1)/2$ classifiers are trained. If N is 10, which means there are 10 classes to be classified, then $10*9/2=45$ classifiers should be trained. This seems an expensive way to train, but only the instances of the two target classes are included into training set, by doing this the training set size is reduced dramatically.

2.4.7. Deep Learning

Deep learning (deep structured learning) is a special field of machine learning family. Deep learning methods are based on artificial neural networks with representation learning which can be supervised, semi-supervised or unsupervised [82]. Deep learning is the child of machine learning and grandchild of artificial intelligence as seen in

Figure 2.10 [82]. Deep learning architectures (like deep neural networks, deep belief networks, deep reinforcement learning, recurrent neural networks, convolutional neural networks, etc.) have produced competitive results and even surpassed human expertise when applied to vast number of different fields like computer vision, speech

recognition, natural language processing, machine translation, bioinformatics, drug design, medical image analysis, climate science, material inspection, board game programs, etc.

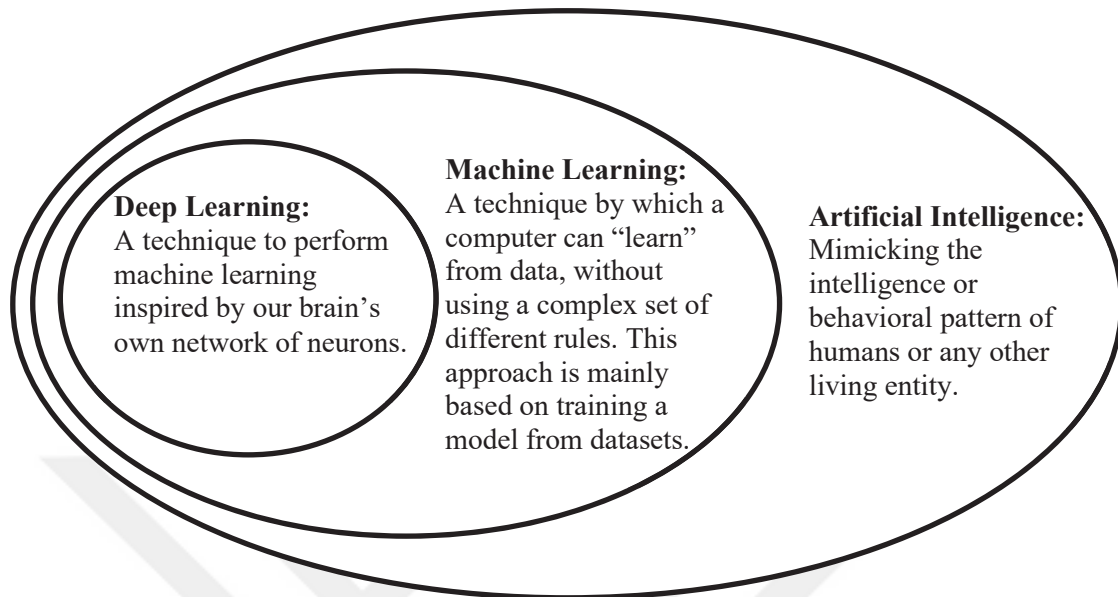


Figure 2.10 Deep learning within artificial intelligence

The adjective "deep" in deep learning refers to the use of multiple layers in the network. Artificial neural networks (ANNs) were inspired by information processing and distributed communication nodes in biological systems, but there are differences from biological brains. Since the network consists of layers it is called "deep". ANNs were first proposed in [83] by Warren McCulloch and Walter Pitts. Multiple layers structure of human cortex inspiring artificial intelligence can be seen in Figure 2.11 [81].

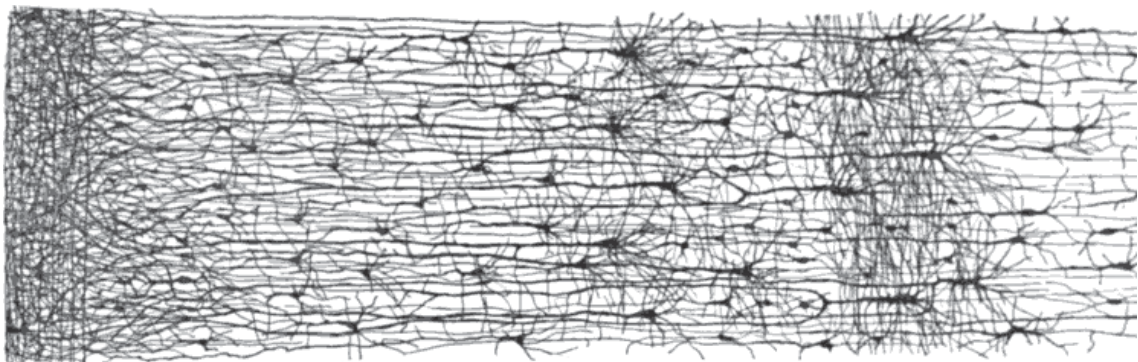


Figure 2.11 Multiple layers of human cortex

Artificial neuron was first proposed by Warren McCulloch and Walter Pitts in their study as a very simple model of the biological neuron: one or more binary (on/off) inputs and one binary output forms the working system of it. The artificial neuron simply activates its output when more than a certain number of its inputs are active. The image in Figure 2.12, illustrates how the simple logical computations are processed within ANNs [81].

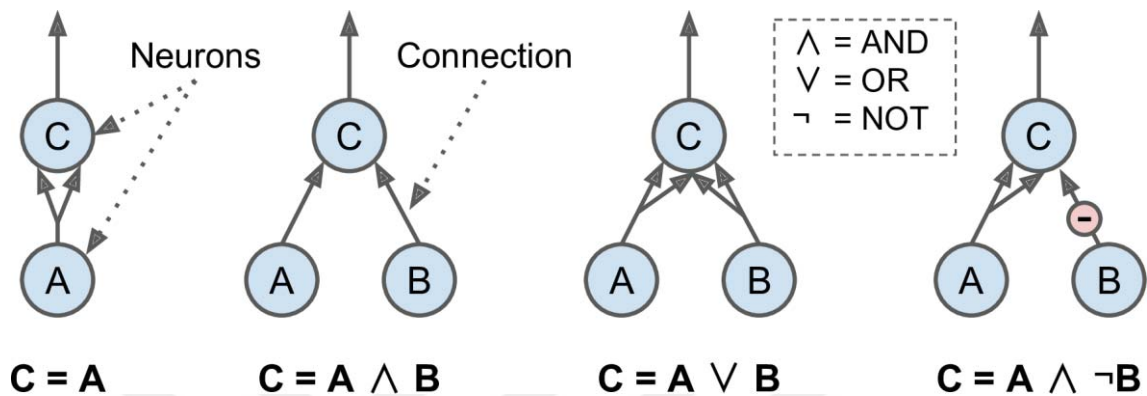


Figure 2.12 Logical operations of ANNs

2.4.8. Convolutional Neural Networks

Convolutional Neural Networks (CNNs) were first proposed by Yann LeCun et al., in [84], after Kunihiko Fukushima presented the Neocognitron in [85]. These studies were the pioneering studies for visual cortex inspired ANN architectures. Later on, different CNN architectures have been presented in literature.

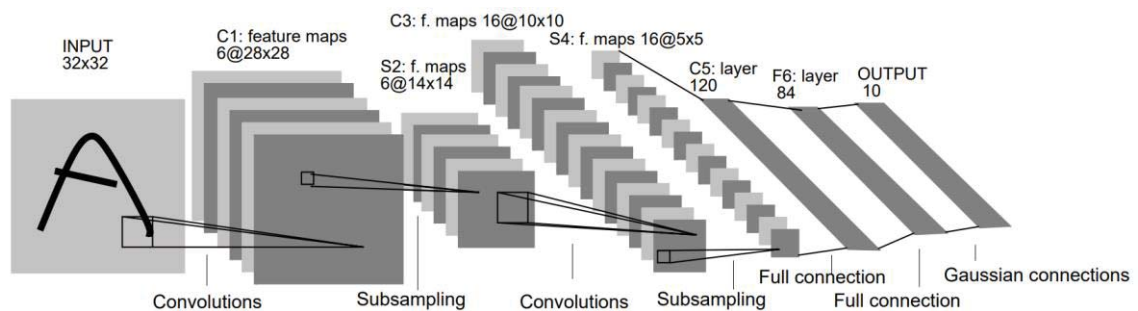


Figure 2.13 Architecture of LeNet-5

In Figure 2.13, the architecture of LeNet-5 proposed by Yann LeCun et al., the model was developed for digit recognition where each plane is a feature map and the weights are constrained to be identical [84]. This architecture has some traditional blocks, such as fully connected layers and sigmoid activation functions, but convolutional layers and pooling layers are also introduced for the first time in literature.

In CNN architecture most of the work depends on the convolutional layers, therefore this layer is important for carrying out the process. The main idea is, all pixels in the input image are not connected with neurons in the first convolutional layer, but the neurons focus on only to pixels in their receptive fields which can be seen in Figure 2.14 [81]. Therefore, low level features in the first hidden layer were assessed by the network when using this architecture, later these features were assembled into larger higher-level features when the next level is processing, and this process is repeated for other levels as well. This hierarchical structure provides CNNs to perform well in image recognition.

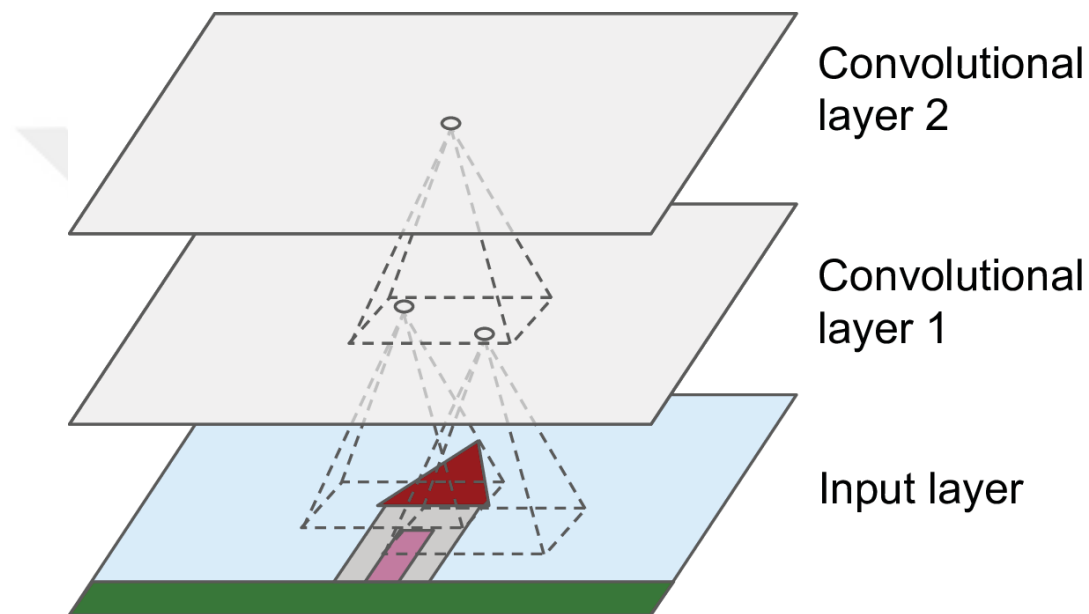


Figure 2.14 CNN layers consist of rectangular local receptive fields

The neuron weights represented as a small image the size of the interested field. The set of weights is also called filter or convolution kernel, because the main idea for CNN architecture was to apply convolutional calculations over image using these filters or other name kernels. In a CNN layer all neurons having the same filter produces a feature map. This feature map contains the information of highlighted areas that activate the filter more than other areas. These filters are not defined manually, during training the convolutional layer automatically determines the most convenient filters for targeted task, and upper layers combine filters into more complex forms.

2.4.9. Weka

Weka is a platform of machine learning algorithms for data mining tasks and includes tools for data preparation, classification, regression, clustering, association rules

mining, and visualization developed in the University of Waikato [86]. Weka is published under the GNU General Public License. The Weka name stands for Waikato Environment for Knowledge Analysis. The software needs java platform already installed in the system.

The objectives of Weka project are:

- Provide ML techniques publicly available
- Solving problems that matter to New Zealand industry
- Developing new ML techniques and providing them to general use
- Improving theoretical knowledge in the literature

The Weka software takes a data file as the input file and processes it accordingly the user selections of methods. The default file format which the Weka software can process, is called attribute-relation file format (ARFF). At the same time, comma separated values (CSV) file can also be processed by the software. Since the default file format is ARFF file, it is easier to launch the experiment with this format.

ARFF files have two sections as the Header information, and the Data information. The Header section of the ARFF file consists of the relation declaration, and attributes declarations (the columns in the data), and their types. The relation name is declared with “@relation [relation name]” format where “@relation” is keyword and “[relation name]” is a string that defines the relation name. The relation name should be quoted if there is space character in it.

The attribute declaration within the header section is more complicated than other sections, since the types of values are set in this section. Also, the sequence of the attribute declaration determines the data section’s columns correspondence to attributes. The form of attribute declaration is like: “@attribute [attribute-name] [datatype]”. “@attribute” is the keyword for attribute declaration. “[attribute-name]” is the name of corresponding column and its format should comply with “[relation name]” declaration as described above. “[datatype]” determines the corresponding column’s data type in the data section, and should be one of the types below:

- numeric
- integer is treated as numeric
- real is treated as numeric
- [nominal-specification]
- string
- date [date-format]

- relational for multi-instance data (for future use)

The data section begins with the “@data” keyword, and the data lines consist of the observations (data instance) and the columns consist of comma separated attributes and the last column is the label. Since attributes are separated by comma, the floating-point separator should be the dot character.

Below, there is a sample of an arff file’s header and data sections of a binary classification problem:

```
@relation 'sample_binary_classification'
@attribute 'attr1' numeric
@attribute 'attr2' numeric
@attribute 'class' {1,2}
@data
3.0497,21.979,1
0.98728,21.841,1
13.238,19.411,1
30.115,-2.1385,2
30.082,16.94,2
...
```

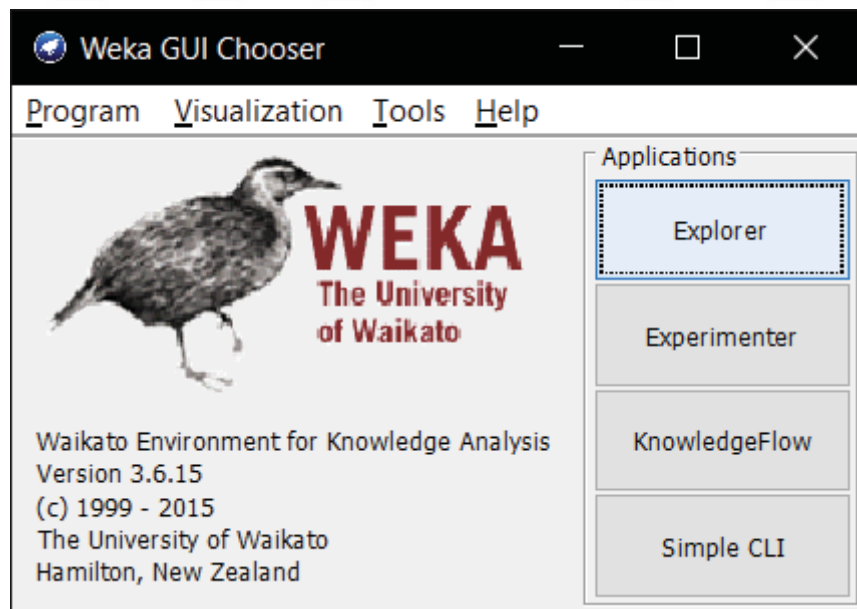


Figure 2.15 Weka GUI Chooser screen

In Figure 2.15, first screen of the Weka software which serves for the different usage of the tool [86]. In this study “Explorer” was used for evaluations and for mass

calculation “weka.classifiers.Evaluation.evaluateModel” class was deployed from MATLAB tool [87].

2.5. Data Set

In this study, medical infrared thermal images were captured during routine inspection in a special clinic owned by a physician (Dr. M. M. YILMAZ Clinic, Kayseri, Türkiye) using IRIS-XP Infrared Thermography Device (Medicore Co. Ltd., Seoul, South Korea). Iris-XP (please see Figure 2.16 [88]), is a Class I medical device, that can measure temperatures between 14.5-40°C. It has both auto and manual focus, and the resolution of the images is 480 (Horizontal) by 640 (Vertical) pixels. The focus range is from 40 cm to infinity, and the system has PACS compatibility.



Figure 2.16 Medicore IRIS-XP medical infrared thermography system

In this clinic, thermal images have been used as a pre-diagnosis tool for the last ten years. The images had a fixed size of 480x480 pixels. The thermal image set was consisting of 3764 images from 63 patients (15 female, ages between 2 - 83). Figure 2.17 demonstrates 8 sample raw images from the database.

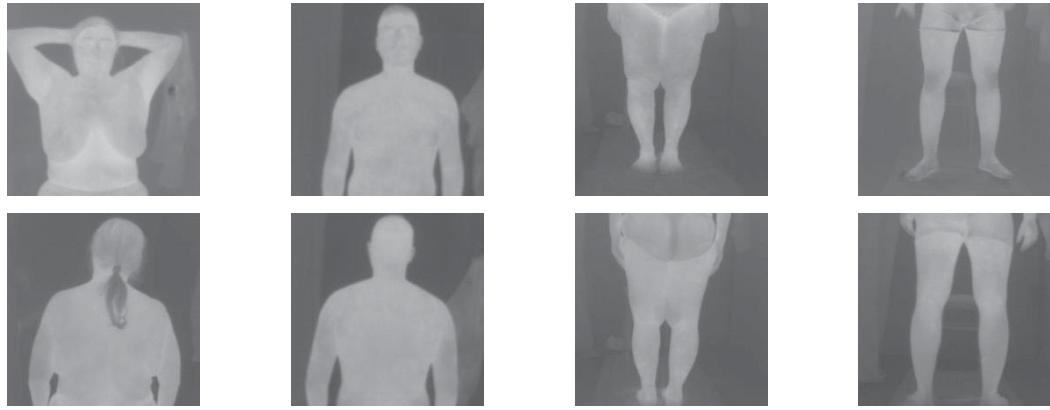


Figure 2.17 Sample raw thermal images from our database

This study was approved by the Erciyes University Ethical Council of Clinical Studies, Kayseri, Türkiye (2019/524). All procedures performed in studies involving human participants were in accordance with the ethical standards of the institutional and/or national research committee and with the 1964 Helsinki declaration and its later amendments or comparable ethical standards. Informed consent was obtained from all individual participants included in the study.

In the clinic, the thermal images are acquired in a controlled environment with stable thermal conditions. Patients take off their clothes during image acquisition and wear only underwear if it is not covering up the examination area. The camera is positioned and focused according to the size and position of the patient. Then, thermal images are captured from anterior, lateral, and posterior positions of the patients from head to toe. First, the patient stands still facing the camera, then turns 90 and 180 degrees around his/her own axis, and then raises the arms. Thus, during the image acquisition procedure thermal images from the upper, lower, frontal and posterior parts of the body were captured.

Chapter 3

Automatic Body Part and Pose Detection in Medical Infrared Thermal Images

Artificial intelligence needs methods that are developed for recognizing human actions in various scenarios for applications such as surveillance, video retrieval and human-computer interaction. Automatic body part and pose detection is a challenging task in digital imaging. There are different challenges for different imaging techniques like illumination, skin color, clothes, noisy images etc. [89]. Generally, the body part detection studies in literature are aiming to track and evaluate the postures and movements of individuals by evaluating the RGB images [89]–[93]. Subsequent to segmenting body area in the image, body key points have to be determined for tracking the movements of a human, which is very unpredictable [93]. Body pose estimating and tracking goes back to 1980's and variety of different studies were investigated applying statistical or deterministic methods for single or multi view [94]. In [95], They integrate the local space-time features obtained from the videos with the SVM classification schemes and use them in classification. In [96] Ramanan et.al. presented a new approach for tracking the people, they developed a model of appearance of each person in the video and tracked that model in the frames.

General studies in literature focuses on the RGB images for body part and pose detection. However, there is no study that evaluated the thermal images for evaluating in this manner. In this study automatic body part and pose detection process was investigated on an authentic medical thermal image database that have been developed in collaboration with an integrative medicine clinic (Dr. M.M. YILMAZ Clinic) in Kayseri, Türkiye. Different thresholding and segmentation methods have been evaluated, and binarizing the image according to the threshold determined using Otsu's method performed well in terms of performance, speed and simplicity compared to other more complex methods like active contours, region growing and local first-order statistics. Thus, Otsu's thresholding-based ROI extraction and histogram equalization method within the selected ROI were used to prepare images for the feature extraction phase. Later, features were

extracted using DarkNet-19 and t-distributed stochastic neighbor embedding (t-SNE) and principal component analysis (PCA) algorithms were employed to select features from the images. The selected features were employed in the classification of the images for body part (upper/lower) and pose (front/back). As a result, an image was able to be labeled with its body part and pose automatically which was a crucial phase in managing unorganized MITI databases. All studies on thermal images need a preliminary step to determine if any image contains the targeted body part and/or pose. Especially the medical centers that investigate the whole body with MITI need an automatic approach to group all the images (hundreds of thousands of them) taken from the patients for the comparison purposes and perform queries on the automatically labeled images.

The aim of this study is that this approach will improve the automatization process of thermal image processing and help physicians study the thermal images in a more user-friendly manner than it is now.

Significant efforts have been put forward for medical infrared thermal imaging (MITI) to be used as a pre-diagnosis method in a clinical setup. Automatization and standardization of the diagnosis process is crucial because the number of medical experts working with MITI is highly limited. The current studies generally need pre-processing and/or preparation or selection of the images manually. Fully automatic systems need minimal manual intervention. One of the manual operations requires physician's determination of the body part and orientation of the patient on each thermal image. In this study automatic pose and body part detection on medical thermal images is investigated. The database included 957 thermal images obtained from 59 patients and was divided into four classes upper-lower body parts with back-front views. First, histogram equalization (HE) method was applied on the pixels only within the body determined using Otsu's thresholding approach. Secondly, DarkNet-19 architecture was used for feature extraction, and principal component analysis (PCA) and t-distributed stochastic neighbor embedding (t-SNE) approaches for feature selection. Finally, the performances of up to 59 machine learning based classification methods were examined. Upper vs. lower body parts and back vs. front of upper body were classified with 100% accuracy, and back vs. front classification of lower body part success rate was 93.38%. This approach will improve the automatization process of thermal images to group them for the comparing one image with the other and to perform queries on the labeled images in a more user-friendly manner.

3.1. Materials and Methods

3.1.1. Thermal Images

In this study 957 thermal images from 59 patients (44 male, ages 2-68) consisting of different body parts and poses were used. The thermal image set was consisting of 3764 images from 63 patients. However, the image set was not standardized due to working conditions of the clinic, and only 957 images were appropriate for further evaluations. Most of the non-standard images were eliminated, however, some images were kept in the image set after we successfully identified the patient as the foreground. For example, in several images the dress of the patient interfered in the image but was assigned as the background using our pre-processing approach (please see Figure 3.1).



Figure 3.1 Sample for non-standard images

For the pose and body part detection of this study which included four different classification problems four different subsets were prepared from the database. The first subset consisted of 4 classes as upper-back (261 images), upper-front (273 images), lower-back (210 images), and lower-front (213 images) which includes all classes in the entire image dataset. The second subset consisted of upper (534 images) and lower (423 images) parts of the body for the second classification problem which is called upper vs. lower. The third subset included 210 posterior/back and 213 anterior/front poses for the third classification problem which is called lower back vs. lower front. The last subset was comprised of 261 back and 273 front images from the upper parts of the body for the fourth classification problem which is called upper back vs. upper front.

3.1.2. Background Extraction with Blue Component of Image

An RGB image consists of three components as red, green, and blue. When these components are investigated, it can be observed that the blue components are gathered on the edges. Using blue component of the image for ROI extraction is a simple and computationally inexpensive method. The original RGB image and three components can be seen in Figure 3.2. The red, green, and blue components of the colored thermal image can be seen in Figure 3.2-a, Figure 3.2-b, and Figure 3.2-c, respectively. In Figure 3.2-e, it can be seen clearly that the body was selected in the image. This is made by applying erosion and dilation procedures on the image.

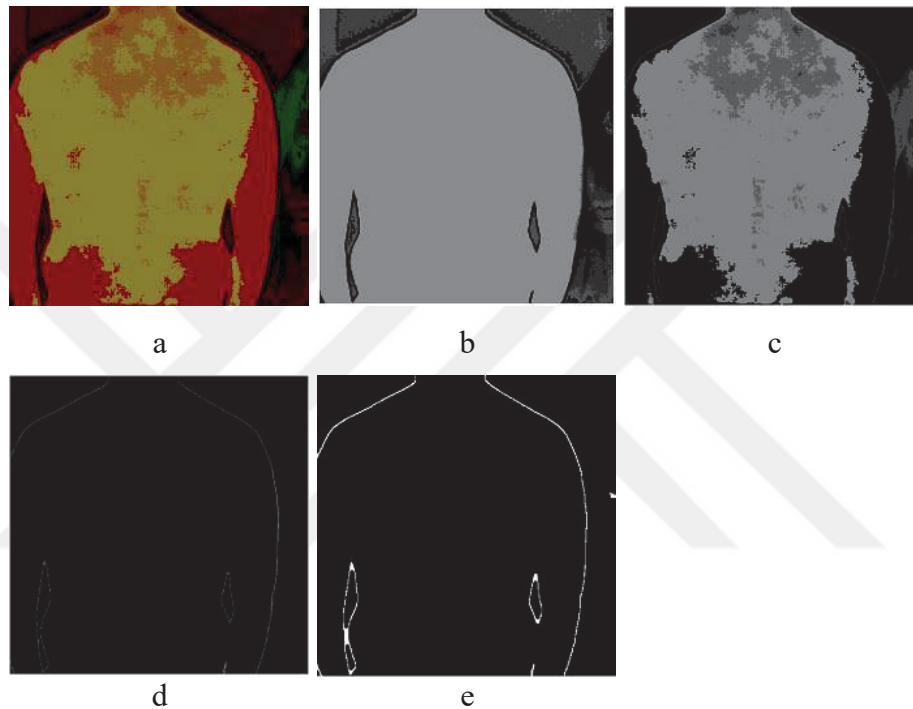


Figure 3.2 Blue component result on standard image (a: RGB image, b: Red component of RGB image, c: Green component of RGB image, d: Blue component of RGB image, e: Blue component edges interconnected)

This method has high performance on standard images, but on non-standard images it fails to wrap around body, since the blue component spreads throughout the image as seen in Figure 3.3. This image is non-standard because the patient had perspired before the imaging was performed, also his cloth hanging on the wall was wet and this made the thermal image inappropriate for further processing.

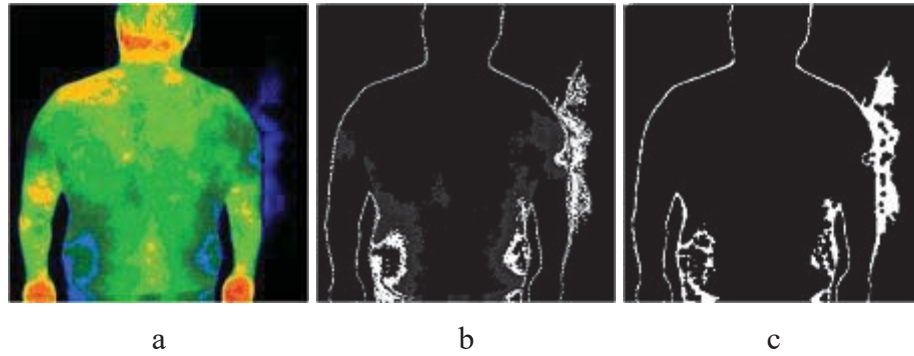


Figure 3.3 Blue component result on non-standard image (a: Non-standard RGB image, b: Non-standard RGB image blue component, c: Non-standard image blue component edges interconnected)

3.1.3. Background Extraction with K-Means Clustering

Since the background and foreground were tried to be separated, since they had different features, using k-means clustering (KMC) approach with two classes can give good results. During evaluations KMC approach showed great success on background extraction over blue component method. In Figure 3.4, it can clearly be seen that KMC method outperformed the blue component method. Especially the performances on the same image can be compared with figures Figure 3.3-c and Figure 3.4-f for blue component method and KMC method, respectively.

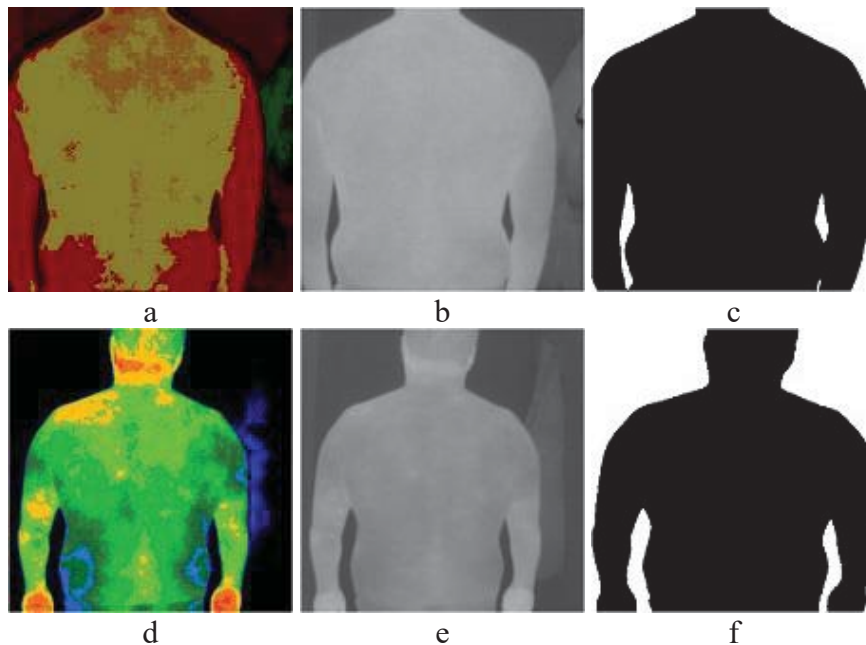


Figure 3.4 Results using k-means clustering approach to extraction the foreground (a & d are original RGB images, b & e are temperatures, c & f are extracted body images).

3.1.4. Background Extraction with Thresholding

Since human body is hotter than its environment, the background can be extracted by thresholding the environment temperatures from the image. Since the thresholding is done by the temperature values non-standard images will not produce good results. The performance of thresholding depends on the selected thresholding method. In our first trial all temperatures, which are greater than a level, were set to 1 (white) and the others to 0 (black). This method successfully extracted human body from the background on standard images (Figure 3.5-c), but it failed to extract background on non-standard images (Figure 3.5-g). Another well-known thresholding method, Otsu's method [78] was used to increase the robustness. This method depicted better performance on different kinds of images. It is observed that both standard and non-standard images were perfectly extracted from background. Figure 3.5-d shows the result for Otsu's method on a standard thermal image, and Figure 3.5-h indicates a non-standard image on which a perfect extraction was achieved. KMC and Otsu's method show similar performances on background extraction. However, when these two methods were compared in terms of computation speed Otsu's method (0,00209 seconds) outperformed KMC method (0,08313 seconds). In this study further steps were proceeded with Otsu's method.

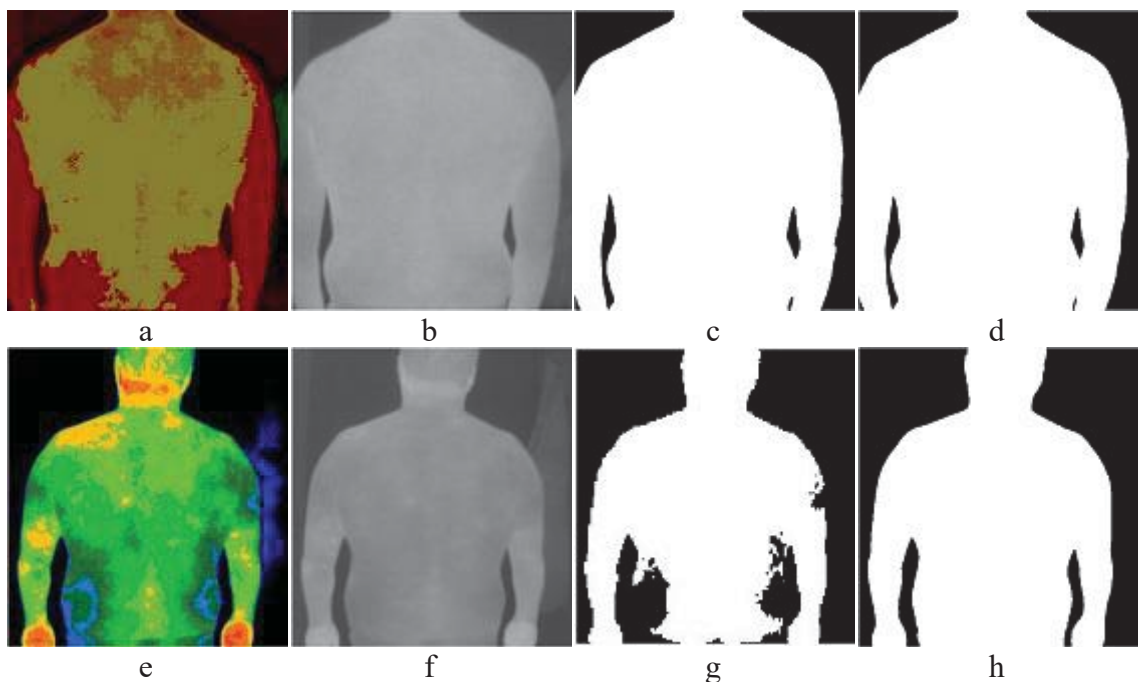


Figure 3.5 Results for background thresholding (a & e: original RGB images, b & f: temperatures, c & g: level thresholding results, and d & h: Otsu's thresholding results).

3.1.5. Preprocessing of Thermal Images

A thermal image consists of thermal values ranging from the lowest room temperature to the highest body temperature. The informative portion of the temperature range exists on the body temperature level, which makes lower temperatures uninformative. The pixels corresponding to non-body parts of the scene decrease the success of the histogram equalization (HE) approach, and the resulting image becomes a low contrast one, which makes the success of the classification process also low. For this reason, a different approach was prepared that the HE method should be used to equalize the histogram of the pixels only within the ROI in order to improve the feature selection procedure[97]. HE method was used to adjust the contrast by manipulating the histogram of the image [98]. Otsu's approach [78], which is a well-known thresholding method for gray level images, was used for discriminating foreground (patient) from the background (non-body parts). Different thresholding and segmentation methods have been evaluated and binarizing the image according to the threshold determined using Otsu's method was good on performance, speed and easy to apply aspects compared to other methods. After determining a proper threshold for each image separately with Otsu's method, the images were binarized with the calculated threshold to generate the foreground mask. The binarized images served as masks for the body parts, which was referred to as the ROI, and the histogram equalization was performed on the mask of each image one-by-one.

3.1.6. Feature Extraction and Selection

Convolutional Neural Networks (CNNs) have recently become a popular approach for image processing. In this study, the pre-trained DarkNet-19 architecture was used for feature extraction from the thermal images. The Darknet-19, which was developed by Redmon et al. [99], consists of a CNN architecture with 19 layers as depicted in detail in Table 3.1 [99].

1024 features were extracted using "avg1" layer of DarkNet-19 from each image. After the feature extraction phase, feature selection was applied to decrease the number of features. Principal component analysis (PCA) [100] and t-distributed stochastic neighbor embedding (t-SNE) [101] algorithms were applied for this purpose. PCA is a method to represent data, which captures most variable dimensions of data and removes low ones to reduce the data dimension. PCA was selected for testing due to its low cost in computation [100]. In contrast, t-SNE embeds high dimensional points to lower

dimensions by considering similarities between neighbors [101] and calculates generally 2-3 features from the available feature set. Different number of features were selected using PCA and t-SNE and the effect of the number of features was investigated for each selection approach and classification methodology.

Table 3.1 DarkNet-19 architecture.

Type	Filters	Size/Stride	Output
Convolutional	32	3×3	224×224
Maxpool		2x2/2	112×112
Convolutional	64	3×3	112×112
Maxpool		2x2/2	56×56
Convolutional	128	3×3	56×56
Convolutional	64	1×1	56×56
Convolutional	128	3×3	56×56
Maxpool		2x2/2	28×28
Convolutional	256	3×3	28×28
Convolutional	128	1×1	28×28
Convolutional	256	3×3	28×28
Maxpool		2x2/2	14×14
Convolutional	512	3×3	14×14
Convolutional	256	1×1	14×14
Convolutional	512	3×3	14×14
Convolutional	256	1×1	14×14
Convolutional	512	3×3	14×14
Maxpool		2x2/2	7×7
Convolutional	1024	3×3	7×7
Convolutional	512	1×1	7×7
Convolutional	1024	3×3	7×7
Convolutional	512	1×1	7×7
Convolutional	1024	3×3	7×7
Convolutional	1000	1×1	7×7
Avgpool		Global	1000
Softmax			

3.1.7. Classification: Pose Detection

Different standard classification methods were applied on selected feature sets for four different image-subsets separately. The Waikato Environment for Knowledge Analysis (Weka) [86] and MATLAB were the software tools that were used for testing

different classification approaches. MATLAB’s “Deep Learning Toolbox” was used during CNN architecture evaluations. Features were extracted with DarkNet-19 pretrained network available in that toolbox. After the feature extraction and selection phases, the classification methods were evaluated on Weka except for the support vector machines (SVM) method which was performed on MATLAB. Fifty-nine classification methods (please see Table 3.2) were applied to feature sets which were selected by PCA and t-SNE methods. These feature sets contained up to 956 features according to the number of samples in the datasets. For the first, second, third and fourth data sets 956, 956, 534 and 422 different ARFF files were prepared respectively for this purpose. The selected methods with best performances among 59 methods were used in this study were Random Forest (RaF), Rotation Forest (RoF), Sequential Minimal Optimization (SMO), Bayesian Logistic Regression (BLR), Instance Based 1 Nearest Neighbor (IB1), Reduced Error Pruning Tree (REPTree), and Support Vector Machines (SVM). These methods were the best among the tested methods available in Weka and MATLAB in terms of classification accuracy. The details of these approaches can be found in [102]. The classification accuracy metrics used were the accuracy, true positive rate, false positive rate, precision, recall, and F-score.

Table 3.2 Classifiers list employed during evaluations

Classifier Family	Classifiers
functions	Logistic, RBFNetwork, SimpleLogistic, SMO, SPegasos, VotedPerceptron
Bayes	BayesianLogisticRegression, BayesNet, DMNBtext, NaiveBayes, NaiveBayesUpdateable, NaiveBayesSimple
lazy	IB1, IBk, LWL
meta	AdaBoostM1, AttributeSelectedClassifier, Bagging, ClassificationViaClustering, ClassificationViaRegression, CVParameterSelection, Dagging, Decorate, END, FilteredClassifier, Grading, LogitBoost, MultiBoostABs, MultiClassClassifier, MultiScheme, OrdinalClassClassifier, RacedIncrementalLogitBoost, RandomCommittee, RandomSubSpace, RotationForest, Stacking, StackingC, ThresholdSelector, Vote
misc	HyperPipes, VFI
rules	ConjunctiveRule, DecisionTable, JRip, NNge, PART
trees	ADTree, DecisionStump, FT, J48, J48graft, LADTree, LMT, NBTree, RandomForest, BFTree, SimpleCart, RandomTree, REPTree

3.2. Results

Figure 3.6 shows a visual comparison of different thresholding and segmentation methods that were evaluated in this study. Otsu's method performed significantly better in terms on performance, speed and simplicity compared to other more complex methods like active contours region growing and local first-order statistics. As depicted in the figure, Otsu's method was more successful in distinguishing the patient and the background than the other two approaches.

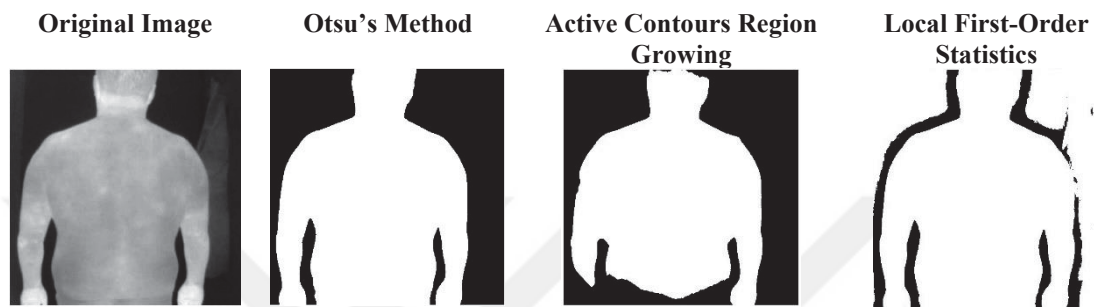


Figure 3.6 Evaluation of segmentation methods

Figure 3.7 demonstrates the outcomes of Otsu's thresholding approach for three different sample images to differentiate the pixels corresponding to body parts from the ones corresponding to non-body parts (background). On the left column original images are presented and, in this column, although the room temperature was controlled, the clothes of the patient could be seen as part of the background, therefore a proper method is needed to successfully segment body parts in the image. There were several images like this one in our image set because the imaging procedure was not fully standardized due to working conditions of the clinic. The masks obtained using Otsu's thresholding method indicated as the ROIs on the images (middle panel) were used to apply on the original image whose output can be seen on the right most column, *i.e.*, only the intensity values corresponding to the pixels inside the mask were kept as they are and the intensities on the remaining pixels (background) were set to zero to be depicted as black.

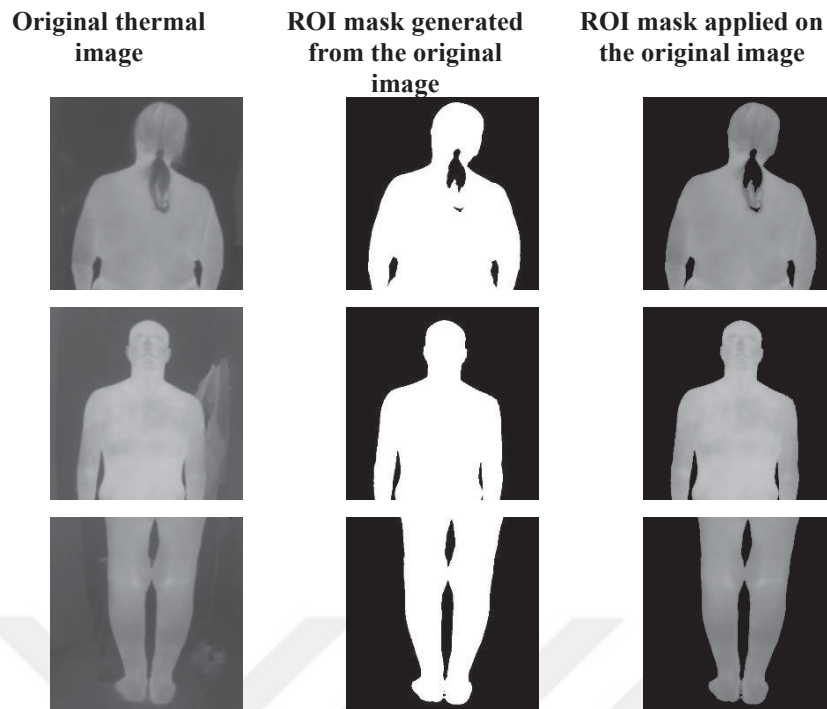


Figure 3.7 Application of ROI mask generated using Otsu’s thresholding method on thermal images

Figure 3.8 shows the outcomes of applying histogram equalization (HE) method on the original or preprocessed images. The figure demonstrates the superior performance of applying the HE method only for the intensity values corresponding to the binary mask obtained using Otsu’s thresholding approach. On the left column the sample raw thermal images can be seen. The second column demonstrates the results of applying the HE method on the original image without any masks. It is obvious that the objects on the background may negatively affect the feature extraction process. On the third column, the HE method was applied on the whole masked image (please see right-most column of Figure 3.8), however, the temperature/intensity details over the body parts were lost. On the right-most column, the HE method was applied only within the ROI which did not include the background pixels. It was observed that the temperature details on the body parts were sharpened and more obvious than the other two cases. This step was critical in terms of feature quality extracted from the images. Thus, it was decided to perform histogram equalization only on the body parts determined by the Otsu’s thresholding method.

Medical thermal image analysis aims to explore the slightly thermal differences on body surface, even less than a half degree can be meaningful. However, there is about 10-degree Celsius difference between body temperature and room temperature, which must

be excluded while processing thermal images. Since the background temperature values were not included in the histogram equalization process, the resulting images were better in terms of being able to differentiate the slight changes on the temperature values on the body when HE was applied on the pixels only within the mask or when HE applied on the whole image. This was the case not only for these sample images but also for many other thermal images in the database.

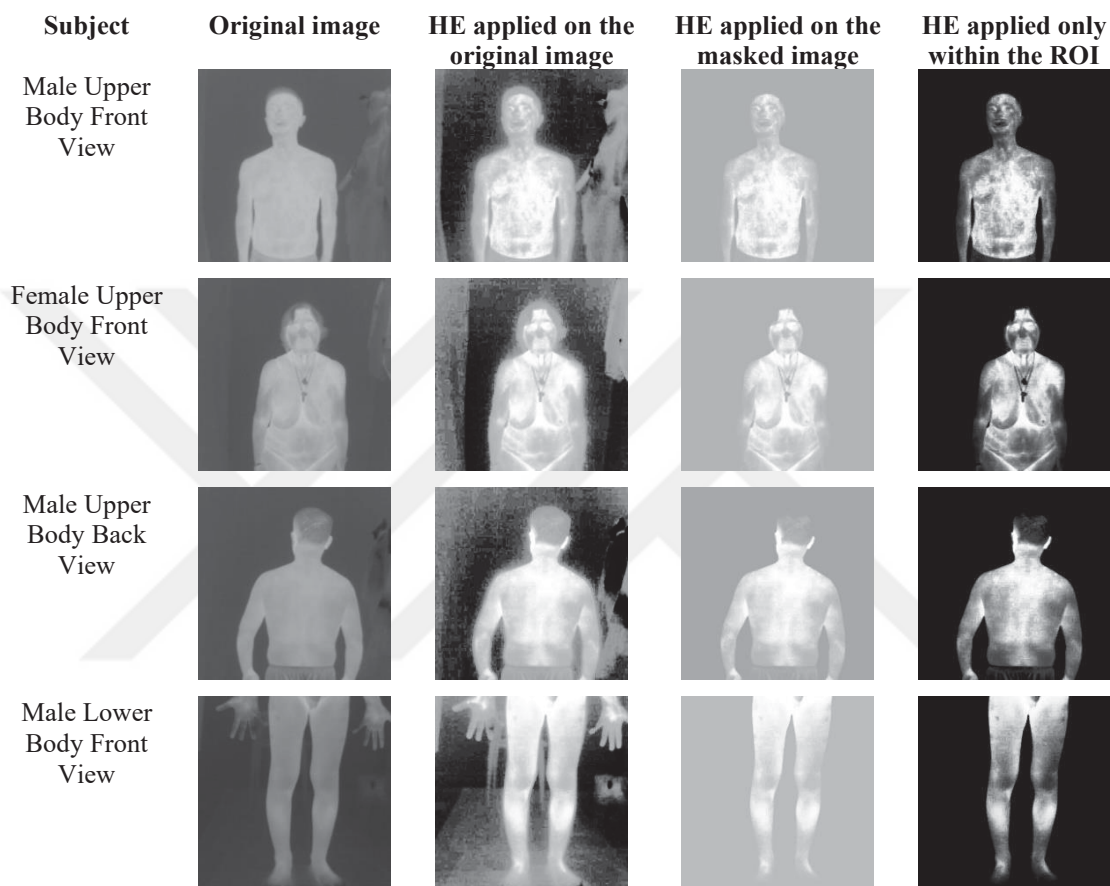


Figure 3.8 The results of histogram equalization (HE) method with and without focusing on the body parts as the ROI The first column: original image, second column: HE applied on the whole image, third column: HE applied on the whole masked image, and the fourth column: HE applied only within the ROI.

The first image dataset was prepared for multi-class classification problem to classify four classes into: lower-back, lower-front, upper-back, and upper-front. The best correctly classification rate observed during experiments was 96.55% with Sequential Minimal Optimization SMO classifier using 103 features selected by PCA.

Then, multi-class classification problem was changed into binary-class classification by increasing classification steps to improve classification accuracy. For this purpose, the first dataset was divided into two classes as upper and lower body parts

for the first step of classification, and for the second step the resulting two datasets were divided into front and back classes separately. In the end four classes were acquired. Selected features in the second image subset were successful in separating the upper and lower body parts. However, the selected features on the third image subset could not differentiate the back and front poses of the lower part of the body. For the fourth image subset the discrimination success increased as good as the second case. The feature selection results using two most features on the first, second, third, and fourth image subsets using PCA and t-SNE can be seen as scatter plots in Figure 3.9. PCA selected the two most principal components and t-SNE calculated two features.

The results depicted in this figure clearly show that t-SNE outperforms PCA in terms of separating these two features and further evaluations were conducted to find out more-than-two-feature bundles can perform better. During evaluations for all four datasets features reached up to the number of images in the subsets, and 59 different classifiers were applied on generated feature sets using WEKA. For example, for the first dataset 956 different incremental ARFF files were prepared using 956 components selected by PCA. These 956 files consisted of the features as the following: The first ARFF file contains 1 feature, the second ARFF file contains 2 features and 956th ARFF file contains 956 features. For the second, third and fourth datasets 956, 422, and 533 different ARFF files were generated respectively. These evaluations demonstrated that increased number of features perform better classification results on both PCA and t-SNE than low number of features do (Table 3.3).

The second image subset was classified with 100% accuracy since upper and lower parts of the body have significant differences. Lower part has two legs, but upper part has a head, two arms and the body, which makes significant difference and automatic classification achieved a great success. However, the success of the back vs. front classification of lower and upper parts separately decreased since both parts have high similarity between front and back scenes. Although upper part classification on fourth dataset success was as good as the second dataset, lower part classification should have been increased by further processing techniques.

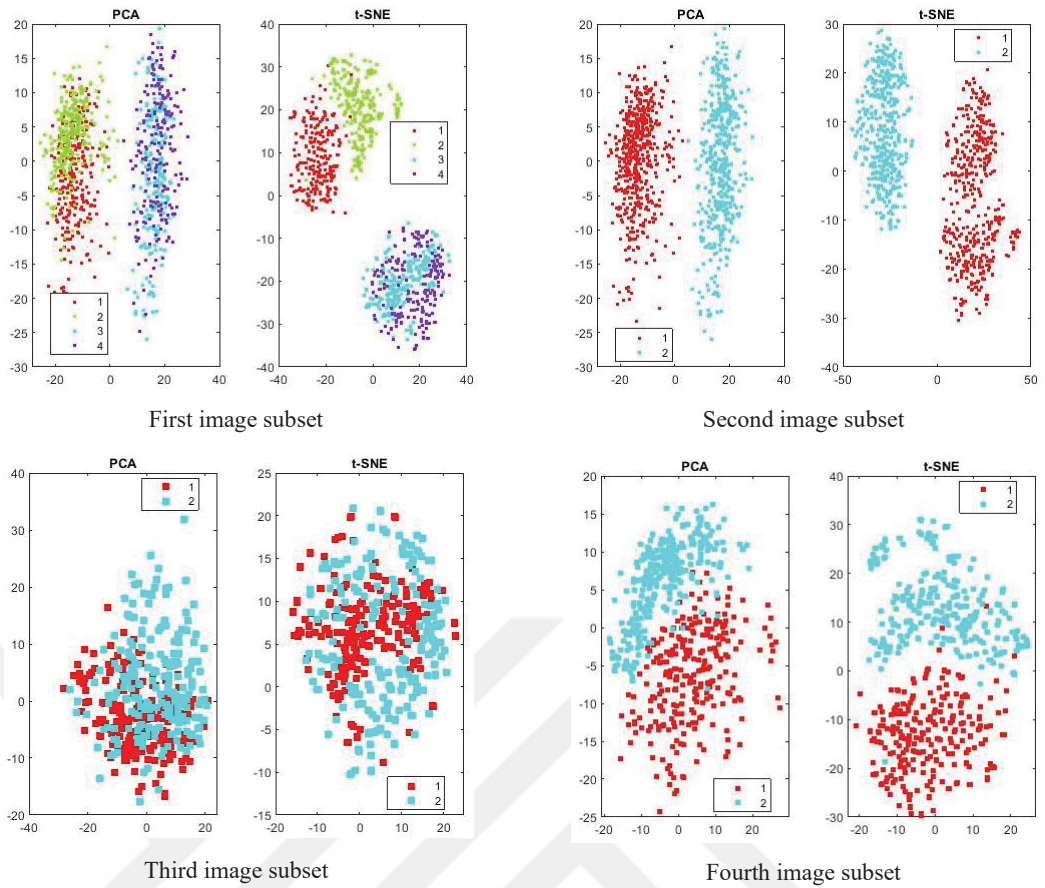


Figure 3.9 PCA and t-SNE results on the first, second, third, and fourth image subsets.

Figure 3.10 demonstrates the resemblance of lower part back view in the first row, and front view in the second row. One can infer that the degraded performance was caused by this resemblance. The high resemblance here can be reduced by using other pre-processing approaches or by eliminating non-standard images from the image set in a future study.



Figure 3.10 A visual explanation of the resemblance of the back and front views of the lower part of the body. Lower part back view is shown on the first row, and lower part front view on the second row.

Table 3.3 summarizes the results of automatic classification with different methods for abovementioned classification problems. The first column demonstrates the data set number used for classification. Since four different data sets were prepared from the thermal images set, the results of three or four methods showing the highest performances were reported here even though the performances of many other methods were investigated. Image subset 1 includes all the images divided into four classes. Image subset 2 also includes all images, but this time images were divided into upper vs. lower classes. Image subsets 3 and 4 include upper and lower images respectively, and in these subsets, images were divided into front vs. back classes. The second column indicates the best performing classification methods for each dataset indicated on the first column. The other columns present the associated method's performance metrics such as the classification accuracy, true positive (TP) rate, false positive (FP) rate, precision, recall, and F-score. The right-most column includes the feature selection method (PCA or t-SNE) and the number of selected features. SMO based classification method performed remarkable well when compared to other methods for all image subsets. One may argue that since the SMO divides the problem into smaller sub-problems and is used to solve quadratic functions it is better suited for the datasets in this study.

Table 3.3 Performance metrics for different classification methods on different image subsets.

Image subset	Classification method	Correctly classified %	TP rate	FP rate	Precision	Recall	F-score	Feature Set
1	RaF	93	0.93	0.02	0.93	0.93	0.93	t-SNE 5
1	SMO	96.55	0.97	0.01	0.97	0.97	0.97	PCA 103
1	SVM	83.5	0.83	0.17	0.86	0.83	0.83	
2	IB1	100	1	0	1	1	1	t-SNE 2
2	REPTree	100	1	0	1	1	1	PCA 2
2	RoF	100	1	0	1	1	1	t-SNE 2
2	SVM	100	1	0	1	1	1	
3	BLR	93.38	0.93	0.07	0.94	0.93	0.93	PCA 60
3	SMO	93.14	0.93	0.07	0.93	0.93	0.93	PCA 55
3	IB1	82.98	0.83	0.17	0.83	0.83	0.83	t-SNE 2
3	SVM	81	0.81	0.19	0.86	0.81	0.80	
4	BLR	100	1	0	1	1	1	PCA 104
4	IB1	97.19	0.97	0.03	0.97	0.97	0.97	t-SNE 2
4	SMO	100	1	0	1	1	1	PCA 110
4	SVM	85	0.85	0.16	0.86	0.84	0.84	

In Figure 3.11, the performance comparison of evaluated methods can be seen. The first dataset has relatively low success rate due to the multi-class classification problem it contains. The second and fourth datasets were well suited for the classification methods

and gained 100% performance. However, the performance on the third dataset was not as good as the other datasets, but it had a promising performance which was over 90% accuracy. Different processing methods will be considered for further studies.

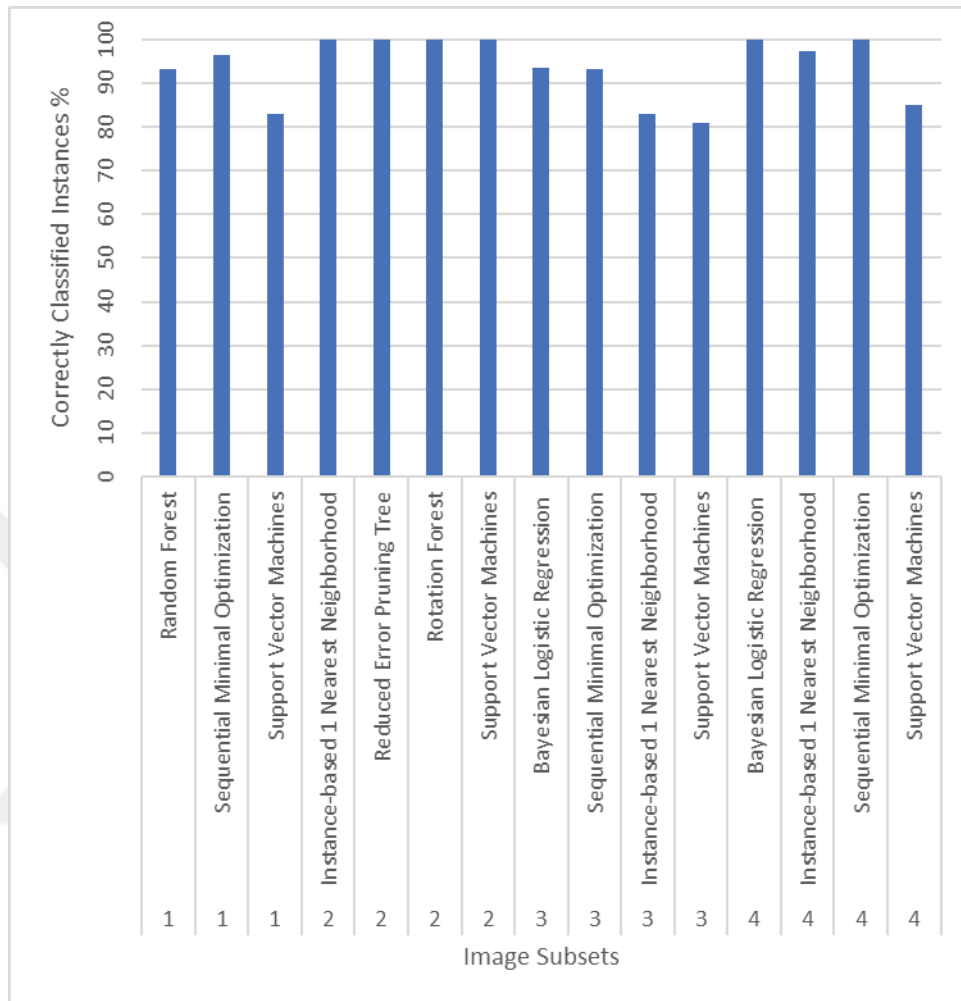


Figure 3.11 Summary of the classification accuracies for the best performing approaches on 4 different image subsets.

3.3. Discussion and Conclusions

MITI is gaining an increased attention in medicine. Since it is a cheap, harmless/noninvasive, and nondestructive approach for medical examination, it has a potential to be employed more frequently as a pre-diagnostic imaging modality. Since the number and skills of experts using MITI in clinical practice are highly limited, automatic schemes might be used to close this gap. The first step for the development of computer-aided diagnosis tool is to determine which part of the body any thermal image contains for further processes such as searching similar cases, creating subsets, performing comparisons between patients or before and after treatment images, and labeling properly.

However, in the literature, automatic detection of different body parts on thermal images automatically has not been studied so far.

It is envisioned that one possible area of body part detection might be the proper labeling of huge datasets for academic use. As expected, upper and lower body parts could be classified with great success and classification of back vs. front of upper body part had same success rate (100%). The clinics employing MITI would need an automatic approach to group thousands of images taken from the patients that is stored in their databases for performing queries on the automatically labeled images and help the physician to compare a case with the other cases in the database.

There are many approaches that can be used to extract features from images. These approaches can be grouped as follows: Low-level (edge, corner, blob, ridge detection and scale-invariant feature transform-SIFT), curvature, shape-based, deformable and active contours [98]. Another group of approaches include texture analysis such as gray-level co-occurrence, gray-level run length, contrast, entropy, homogeneity, etc. [98]. A relatively new set of techniques to extract features from the images is the deep neural networks (NNs) such as convolutional neural networks (CNNs) [103]. CNNs have also been used as the feature extractors. The filter slides along the image and generates a feature map. This map becomes the input of the subsequent layer. This is followed by other layers (pooling layers, fully connected layers, etc.). This whole process lets textural and spectral features to be revealed and exploited. Furthermore, there are numerous studies in the literature in which CNNs were used as the feature extractors [25], [104], [105], and in this study, it was decided to use a CNN based feature extraction approach to be investigated on the medical thermal images. DarkNet-19 is a CNN that is employed as the backbone of YOLOv2.

One of the limitations of this study was the relatively low number of images for processing and classification. The clinic is in the process of collecting more thermal images for different diseases coming from the patients visiting the clinic. Another limitation of the study was that there were non-standard images in the image set. The posture of patients was not similar due to age variance, especially it was hard for children and elderly patients to stand on the right position. This may be overcome by making thermal camera move 360 degrees around the patient where patient stands still, but this is out of the scope of this study.

Chapter 4

Medical Infrared Thermal Image Based Fatty Liver Classification using Machine and Deep Learning

Non-alcoholic fatty liver disease (NAFLD) is a common disorder where there is accumulation of excess fat in the liver affecting people who drink little to no alcohol [106]. Some people with NAFLD can develop an aggressive form of fatty liver disease called nonalcoholic steatohepatitis (NASH). It is manifested by inflammation in the liver and may progress to cirrhosis and liver failure. Due to the substantial change in lifestyle of many people in different countries NAFLD is gaining spread as 15% in 2005 to 25% in 2010 [107]. In the USA approximately 100 million people are estimated to have NAFLD, and especially among children it is the most common form of liver disease.

Disorders, related to blood circulation system and skin surface can be monitored with MITI due to their effect on skin surface temperature. A tumor in breast disturbs the blood circulation within the breast. Imbalanced blood circulation beneath the skin affects the thermal distribution on the surface. The structure of breast made it easy to apply MITI techniques. Therefore, vast amount of the MITI studies were done on the breast tumor screening. Fat accumulated within the liver also disturbs the blood circulation of liver, and therefore, MITI can be effective for screening liver over the skin surface. There is a recent study in [108] which was conducted for classifying the fatty liver disease among mice. They used MITI for capturing the skin temperature map over the liver and achieved 100% classification success.

In this study, our aim was to investigate the feasibility of MITI in automatic detection of NAFLD. Thermal images were evaluated using deep learning- and machine learning-based feature extraction, feature selection and classification methods. Performance comparison of convolutional neural networks (CNN)- and texture analysis-

based feature extraction was the basis for the subsequent analysis aiming at differentiating healthy individuals and the ones with NAFLD.

The main contribution of this study to literature is evaluating human abdomen thermal images using machine and deep learning techniques for NAFLD classification. To our best knowledge, no studies have been conducted in this context on human subjects so far. Different contributions were also made during evaluations of experiments. It was revealed that along with grey level co-occurrence matrix (GLCM) based texture analysis, which was previously shown to be feasible in NAFLD on mice, CNN architectures may be used for feature extraction in this context. Another contribution was to modify GLCM calculation methodology to find pixel co-occurrences only within the upper triangular region-of-interest (ROI) similar to the shape of the liver instead of a rectangular ROI which is more common and includes more unrelated information about the temperature distribution over the liver and nearby regions.

Liver function tests are used to help diagnose and monitor liver disease or damage. In addition, medical imaging and rarely liver biopsy is performed during the evaluation process. Imaging approaches like ultrasonography (US), transient elastography, computed tomography (CT), and magnetic resonance imaging (MRI) are currently being employed in the clinical routine, however, liver biopsy is still perceived as the golden standard to assess progression in the disease [109]. After the biopsy, patients may encounter complications like bleeding, infection and puncture in biliary tract along with temporary pain. Early diagnosis of NAFLD can be ensured by regular follow-up of a patient, however, applying an invasive method like biopsy many times may cause other health risks.

To accompany blood tests and medical imaging as popular non-invasive diagnosis and monitoring approaches, a new pre-diagnosis/scanning modality based on medical infrared thermal imaging (MITI) may be developed as a non-invasive, harmless, user-friendly and cost-effective method. However, MITI is a relatively new and not a dominant method compared to other medical imaging approaches.

Medical infrared thermal imaging (MITI) may be a viable alternative approach for pre-diagnosis and monitoring of NAFLD as a non-invasive and cost-effective method. In this study, the aim was to investigate the feasibility of MITI in automatic detection of NAFLD, and 167 MITI images from 32 patients (123 negative, 44 positive) were evaluated using image processing and classification methods. Three different image sets; unbalanced (original), balanced and upper triangular ROI applied on the unbalanced

dataset were prepared. Eleven different convolutional neural network (CNN) architectures were employed as feature extractors. Texture analysis was evaluated by extracting 9 different texture features. After feature selection and binary classification, the highest values from different setups for recall, f-score, specificity, accuracy, and area-under-curve (AUC) were 1.00, 1.00, 0.83, 1.0, 0.94, and 0.92, respectively. The highest values were achieved by CNN based methods on different datasets, however, texture analysis method performed lower. Here, it is shown that CNN architectures have high potential on extracting features from thermal images. Finally, machine and deep learning approaches can be combined in detecting NAFLD using infrared thermal images.

4.1. Materials and Methods

Thermal images were captured during routine examination of patients of Dr. M.M. YILMAZ clinic in Kayseri, Türkiye. This clinic focuses on traditional and complementary medicine, and the responsible physician (Dr. Mustafa Mücahit Yılmaz) has been using medical thermal images as the initial step of pre-diagnosis of certain diseases (NAFLD is one of them) for the last 10 years. The diagnosis for NAFLD was confirmed with blood tests and ultrasonography performed in public or private hospitals. The collaboration between Abdullah Gül University and Dr. M.M. YILMAZ clinic has been in place since 2019. The research was conducted with the permission of Erciyes University Ethical Council of Clinical Studies, Kayseri, Türkiye (permission number: 2019/524). Informed consent was obtained from all individuals (or their parents if their ages are below 18).

IRIS-XP Infrared Thermography Device (Medicore Co. Ltd., Seoul, South Korea) is used in the clinic for acquiring the images. In the clinic, the thermal images are acquired in a controlled environment with stable thermal conditions. Patients stay only with their underwear and the camera is positioned according to his/her height. First, the patient stands still facing the camera, then turns 90 and 180 degrees around his/her own axis, and then raises the arms. Thus, during the image acquisition procedure thermal images from the upper, lower, frontal and posterior parts of the body were captured.

In this study, the dataset of images consisted of 123 negative (no NAFLD) and 44 positive (with NAFLD) infrared thermal images taken from 32 patients (31 males, ages from 9 to 68). Images from adult women were not included since their breasts covered up the region corresponding to the liver, however, one young female ages of 11 was kept for

further analysis. The mean \pm standard deviation of the body mass index (BMI) of patients who are below and above 18 years old are 19.37 ± 4.71 and 28.51 ± 5.62 respectively. Only the images with upper front view were selected, and each region-of-interest (ROI) corresponding to the anatomical location of the liver was extracted manually. Figure 4.1 demonstrates 3 samples from the database with the original images on the left column and the selected ROI on the right column. The last row depicts the images from an 11-year-old female participant.

4.1.1. Pre-Processing of Thermal Images

Thermal imaging captures the temperature values of the scene as pixel values using infrared sensor arrays. These pixel (temperature) values are used to color the image either as RGB or grey level. In this study only the grey level images (raw images) were used. In the beginning foreground extraction was applied to images using Otsu's approach [78] for eliminating the background (uninformative temperature values) and letting us to focus on the trunk images of the patients. Several segmentation approaches like active contours region growing and local first-order statistics were investigated, and Otsu's thresholding method was easy and more successful in distinguishing foreground and background than the other two approaches.

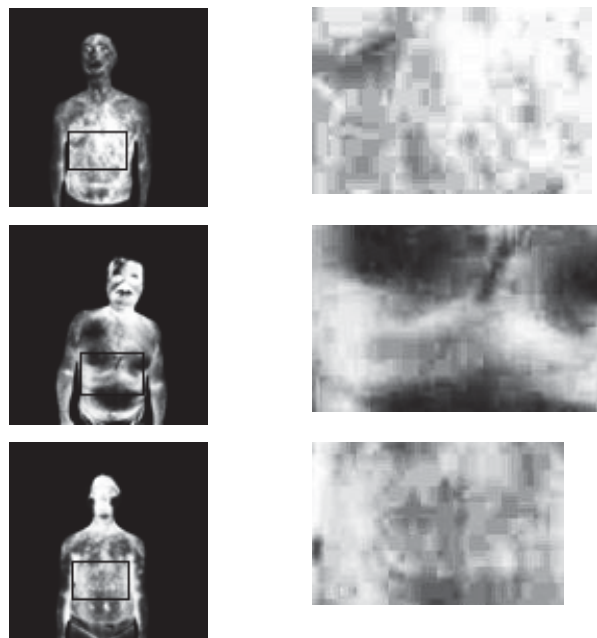


Figure 4.1 Upper front view of thermal images and the corresponding liver regions selected manually

Histogram equalization (HE) method [98] was applied to the outcomes of the Otsu's segmentation approach to boost slight differences in the temperature over the body. Thus, HE method was modified to equalize the histograms only within the body, i.e., Otsu's segmentation produced a mask and HE was applied on the pixels corresponding to that mask [97]. When HE process was over, the anatomical location corresponding to the liver on each image was extracted from the image manually. The pre-processing steps can be seen in Figure 4.2. Figure 4.2 Pre-processing of images a: original image, b: foreground mask, c: HE applied only within the body, and d: ROI corresponding to the liver of the patient.

, where the original image, the mask of foreground/body using Otsu's approach, HE applied on masked image only within the body, and manually extracted liver region can be seen on columns a, b, c, and d respectively. In the last step of the pre-processing phase, selection of ROI corresponding to the liver of the patient was done manually since postures of the patients were not uniform.

4.1.2. Image Datasets

Thermal images were used to generate three different datasets for evaluating different methods. Dataset 1 contained all thermal images (123 negative and 44 positive). Dataset 2 was formed by eliminating 50% of negative subjects' images by keeping the subject number constant (61 negative and 44 positive) for evaluating if the imbalance between negative and positive subjects has negative affect on classification performance. Dataset 3 was formed to improve the performance by reducing the ROI to the upper triangle of the thermal images and no images were removed while generating this dataset. In Figure 4.3, how upper triangular-shaped ROI was obtained from the thermal images can be seen on a positive sample. The left column shows the original image, and the right column depicts the ROI with upper triangular shape. Upper triangular ROI was considered to be well suited to the shape of the liver and more uninformative pixels (temperature pixels that do not correspond to the liver area) would be eliminated.

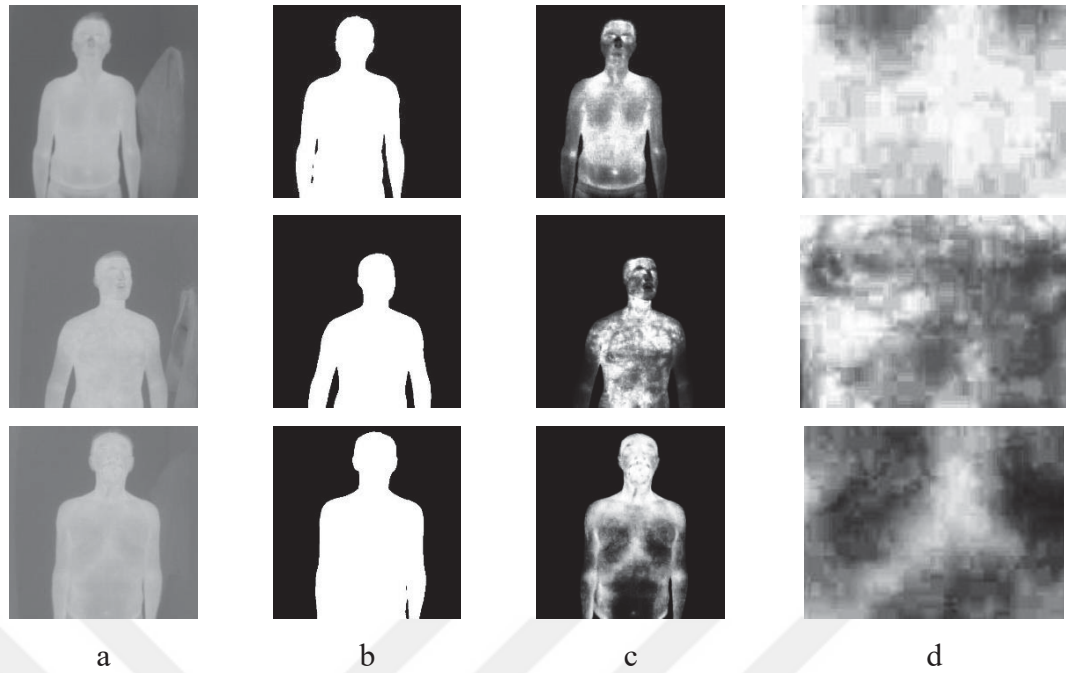


Figure 4.2 Pre-processing of images a: original image, b: foreground mask, c: HE applied only within the body, and d: ROI corresponding to the liver of the patient.



Figure 4.3 Upper triangular ROI used in Dataset 3.

4.1.3. Feature Extraction and Selection of Thermal Images

Two different feature extraction approach were used in this study, texture analysis and CNN architectures. Texture analysis approach was similar to the one used on mice [108] such as mean temperature, variance, skewness, kurtosis, entropy features were extracted from thermal images, and contrast, correlation, energy, and homogeneity were calculated from gray level co-occurrence matrix (GLCM). GLCM contains the number of co-occurrences of 2 gray level values within a neighborhood throughout the image. In this study, 1-neighbor GLCM was calculated both all over the image and only within the upper triangular ROI of the image to compare if there would be an improvement on classification performance. By default, the gray levels of image are scaled into 1-to-8

integer interval including boundaries while calculating GLCM. In our study, GLCM calculation was modified and was added to performance comparison to calculate GLCM in 1-to-256 interval. This modification was applied not to lose the details on thermal images while scaling into 1-to-8 integer interval. In medicine, even 0.5-degree change may be an important symptom of a disease.

Convolutional Neural Networks (CNNs) have proven themselves as a powerful tool for image segmentation, feature extraction and classification. In this study, different pre-trained CNN architectures [87] were investigated for feature extraction from the thermal images. The number of channels in the gray level images was increased from one to three by copying pixel values to new channels for evaluating in CNN phase. The CNNs used here are listed as DarkNet-19, DarkNet-53, ResNet-18, ResNet-50, ResNet-101, DenseNet-201, VGG-16, GoogleNet, SqueezeNet, AlexNet, and Inception-ResNet-v2. These CNN architectures produced 1000 to 4096 features from different datasets.

Two different feature selection methods were evaluated for feature selection step; principal component analysis (PCA) [100] and t-distributed stochastic neighbor embedding (t-SNE) [101] approaches. PCA is computationally low-cost approach and finds the most varying dimensions in the dataset [100]. Therefore, PCA was selected for feature selection in this study, and t-SNE was eliminated due to performance failure on time consumption and classification accuracy during preliminaries.

4.1.4. Classification

These selected feature sets were used to generate train and test files to be used in The Waikato Environment for Knowledge Analysis (Weka) [86] tool. Leave-one-subject-out cross-validation method was used (n-fold cross-validation, in this case 32-fold), and 81078 and 54052 train-test set combinations were generated during CNN and texture analysis steps respectively for evaluating classification methods implemented in Weka, which is a well-known tool for evaluating classification methods and contains numerous methods to investigate on. In this study up to 52 different classification methods (please see Table 4.1) were employed to determine the one with the best performance. The best performing methods and their abbreviations are listed in Table 4.3. For this reason, about 5.000.000 different classification attempts have been made by developing an interface using MATLAB and through this interface Weka tool was used for automatic classification attempts. Actually, the experimental setup was prepared for

$(81078+54052) \times 52 = 6021184$ classification attempts, but some methods were eliminated during evaluations due to low classification accuracy and high computational cost.

All classification results were analyzed using CCI (correctly classified instances) values of 32 folds of each setup, which were computed during the analysis using WEKA tool. These 32-fold CCI values were processed with majority voting method (if a CCI value of test set of a fold was greater than 50% then that subject got 1 vote else 0 vote), TP (true positive) and TN (true negative) values were computed by summation of these vote values. Then performance metrics were computed using TP and TN values. Classification performances were compared on recall, F-score, specificity, accuracy, and AUC of the results after majority voting phase.

Table 4.1 Classifiers list employed during evaluations

Classifier Family	Classifier
functions	Logistic, RBFNetwork, SMO, SPegasos, VotedPerceptron
Bayes	BayesianLogisticRegression, BayesNet, DMNBtext, NaiveBayes, NaiveBayesUpdateable
lazy	IB1, IBk, KStar
meta	AdaBoostM1, AttributeSelectedClassifier, ClassificationViaClustering, ClassificationViaRegression, CVParameterSelection, Dagging, END, FilteredClassifier, Grading, LogitBoost, MultiBoostAB, MultiClassClassifier, MultiScheme, OrdinalClassClassifier, RacedIncrementalLogitBoost, RandomCommittee, RandomSubSpace, Stacking, StackingC, Vote
misc	HyperPipes, VFI
rules	ConjunctiveRule, DecisionTable, JRip, NNge, PART
trees	ADTree, DecisionStump, FT, J48, J48graft, BFTree, SimpleCart, RandomTree, REPTree
rules	OneR, Ridor, ZeroR

4.2. Results

In this study, the dataset of images consisted of 123 negative (no NAFLD) and 44 positive (with NAFLD) infrared thermal images taken from 32 subjects (25 negative and 7 positive subjects). Only one subject was female (age of 11). The ages of the subjects ranged from 9 to 68, and 9 subjects were below 18 years old. The mean +/- standard deviation of the body mass index (BMI) of patients who are below and above 18 years old are 19.37 ± 4.71 and 28.51 ± 5.62 respectively. The average BMIs of positive and negative groups are 30.58 and 24.82 respectively.

The control group patients were selected among other patients who were seeking treatment for diseases other than NAFLD. The disorders the control group suffered from scoliosis, hypothermia-hyperthermia in extremities, neuronal blockage in extremities, thyroid hypoactivity-hyperactivity, hypothermic thymus, dorsal pain center, arterial disorder, sinusitis, and varicose.

The feature exploration step was conducted to find out the most informative features. The importance of this step can be seen in Figure 4.4 where classification results of different feature sets (number of selected features ranged from 1 to 148 in Dataset 1) were displayed. If all cases were not explored, the system would converge to local optimum and miss global optimum.

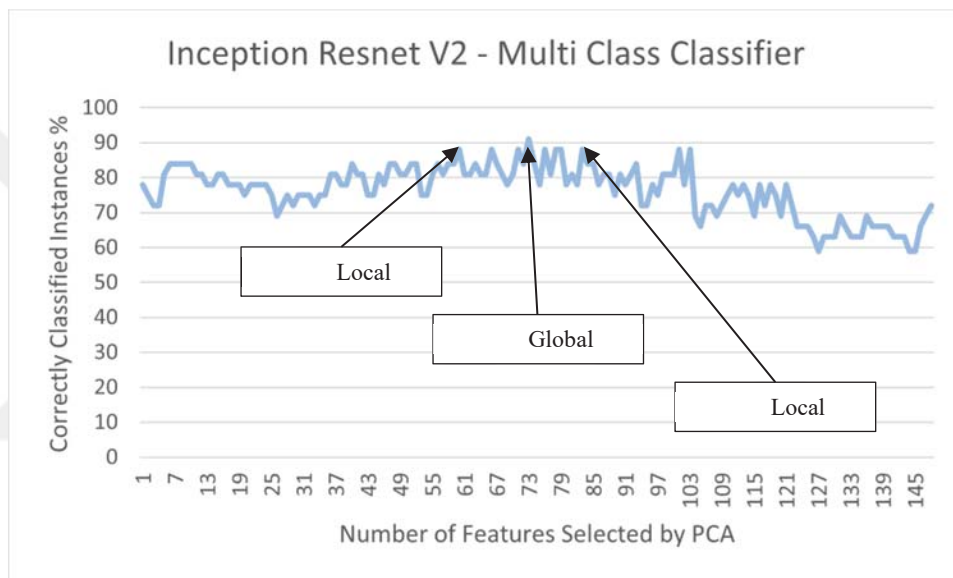


Figure 4.4 Classification accuracy of MCC classifier in which the features were extracted using Inception Resnet V2 extractor and selected by PCA (1 to 148 features).

Table 4.2 summaries the best classification performances of the evaluated classification attempts on different setups. Each line of the table represents a classification phase. The explanation of the columns of the table as follows: The first column contains the neural networks and texture analysis used for feature extraction. The second column depicts the dataset on which the feature extractor was applied. The third column displays the number of features used in the classification phase of that line (determined after testing different number of features). In columns 4 to 8 the classification method, recall, F-score, AUC, and average TPR (aTPR) are listed respectively. PCA method outperformed t-SNE

method nearly in all classification evaluations, therefore, the second feature selection method was not included in Table 4.2 for simplicity.

Table 4.2 Summary of the classification attempts those with the highest performances.

Setup	Dataset	Feature Extractor	# of PCA Features	Classifier	Recall	Specificity	F-Score	Accuracy	AUC
1	1	AlexNet	6	VFI	1.00	0.60	0.58	0.69	0.80
2	1	DenseNet-201	11	VP	1.00	0.56	0.56	0.66	0.78
3	1	Inception-ResNet-v2	79	MCC	1.00	0.84	0.78	0.88	0.92
4	1	Inception-ResNet-v2	5	FC	0.71	1.00	0.83	0.94	0.86
5	1	Texture-8 level	122	END	0.71	0.80	0.59	0.78	0.76
6	1	Texture-256 level	80	CVC	0.43	1.00	0.60	0.88	0.71
7	1	Texture-256 level	3	SPegasos	0.86	0.52	0.48	0.59	0.69
8	2	Inception-ResNet-v2	73	MCC	1.00	0.70	0.76	0.81	0.88
9	2	Inception-ResNet-v2	82	MCC	0.86	0.71	0.84	0.84	0.85
10	2	AlexNet	42	BLR	0.71	0.59	0.80	0.78	0.76
11	2	DenseNet-201	78	JRip	1.00	0.67	0.72	0.78	0.86
12	2	Texture-8 level	55	SMO	0.71	0.55	0.76	0.75	0.74
13	2	Texture-256 level	6	SPegasos	0.86	0.50	0.56	0.63	0.71
14	3	AlexNet	94	SMO	0.71	0.96	0.77	0.91	0.84
15	3	AlexNet	112	Logistic	1.00	0.72	0.67	0.78	0.86
16	3	DenseNet-201	65	VP	0.86	0.76	0.63	0.78	0.81
17	3	Inception-ResNet-v2	76	VP	0.71	0.80	0.59	0.78	0.76
18	3	Inception-ResNet-v2	1	CVC	1.00	0.44	0.50	0.56	0.72
19	3	Texture-8 level	11	VP	0.71	0.52	0.41	0.56	0.62
20	3	Texture-256 level	134	JRip	0.43	0.96	0.55	0.84	0.69
21	3	Texture-256 level	11	VP	0.71	0.52	0.41	0.56	0.62

Table 4.3, lists the abbreviations of classification methods displayed in Table 4.2. The listed methods are available in Weka tool.

Table 4.3 Abbreviations of classification methods.

Method Name	Abbreviation
Bayesian Logistic Regression	BLR
Classification Via Clustering	CVC
Ensembles of Balanced Nested Dichotomies	END
Filtered Classifier	FC
Multi Class Classifier	MCC
Multinomial Logistic Regression	Logistic
Primal Estimated Sub-GrAdient SOLver for SVM	SPegasos
Repeated Incremental Pruning	JRip
Sequential Minimal Optimization	SMO
Voted Perceptron	VP
Voting Feature Intervals	VFI

The highest recall, F-score, specificity, accuracy, and AUC values were achieved by different setups, which means there was no overall winning setup across all performance metrics. Setup 4 has the highest results on specificity, F-score, and accuracy with 1.00, 0.83, 0.94, respectively. However, the highest AUC score was achieved by setup 3 and followed by setup 9 with 0.92, and 0.86, respectively. Both texture- and CNN-based feature extraction methods performed well, however, CNN-based methods outperformed texture-based methods. The 256-grey level GLCM calculation produced better accuracy over traditional 8-grey level GLCM computation on Dataset 1 (original dataset), but the AUC was decreased due to recall failure. The modified GLCM computation method (computation of the GLCM only within upper triangular ROI) was applied with both 8- and 256-grey levels on dataset 2 and depicted in Table 4.2. Texture-256 level feature extraction method with JRip classifier outperformed texture-8 level except for the recall metric.

Dataset 1 is the original set of images on which no modifications were made. This dataset is imbalanced between positive and negative instances. Therefore, dataset 2 was built to help us investigate the effect of the imbalanced nature of the original dataset. The highest classification accuracy results of dataset 1 and dataset 2 were tested with Kruskal-Wallis test [110]. The result of Kruskal-Wallis test show that the results of dataset 1 and dataset 2 were not normally distributed, therefore the non-parametric t-test was applied and no significant difference was reported between the results of dataset 1 and dataset 2 ($p\text{-value} > 0.05$). It is revealed in our study that the imbalance between the classes did not have significant or any negative effect on the classification accuracy. Dataset 3 was built to evaluate if the pixels that do not belong to liver on the abdomen have negative effect on the classification performance, and a second ROI extraction approach was applied by selecting an upper triangular ROI for evaluation. The highest classification accuracy results of dataset 1 and dataset 3 were tested with non-parametric t-test since they were not normally distributed. The results revealed that there was no significant difference between the results ($p\text{-value} > 0.05$). Majority voting method was applied to classification accuracy result of each subject as such, if accuracy is greater than 50%, it is assumed that the subject was classified correctly. Thus, reducing the ROI to upper triangle improved the success for the feature extraction methods AlexNet and DenseNet-201, however the performance decreased for feature extraction methods Inception-ResNet-v2 and the two texture methods.

4.3. Discussion and Conclusions

Vast amount of MITI studies focus on breast screening [36], [65], [111]–[114]. There are other anomalies such as the inflammatory arthritis, osteoarthritis, soft tissue rheumatism, tennis elbow, fibromyalgia, complex regional pain syndrome, peripheral circulation, and fever [115]–[117] that MITI was proposed as the diagnosis/monitoring tool. Moreover, in recent years the field of quantitative analysis of thermal images emerged and has the potential to yield objective interpretation rather than physician-dependent (subjective) analysis [12]. To be more specific, in [65], different sets of features were generated from breast infrared (IR) thermal images and their classification performances were evaluated using support vector machines (SVM). The study in [118] includes the performance comparison of MITI on screening cardiovascular disease with traditional techniques and found promising results. In [48], MITI was used for identifying diabetic foot ulcers. The researchers calculated the mean temperature of regions of interest by considering thermal asymmetry, and applied different machine learning (ML) algorithms on the calculated features. In [66], IR images of both iris were used for diagnosing type-2 diabetes. A decision support system was offered for predicting hemodynamic shock in pediatric intensive care unit and promising performance was achieved in [50]. In [67], burn wounded patients were monitored and a treatment decision system was developed to offer the patient most effective treatment method. A review of studies performed on different diseases can be found in [68].

Furthermore, attaching an infrared camera into a monitoring system is another beneficial use of MITI in medicine. In [69], a smartphone camera-based photoplethysmography (PPG) and a low-cost thermal camera were combined in an instant stress detection model. A facial expression recognition system, using thermal images and SVM, was proposed in [70].

Disorders, related to blood circulation system and skin surface can be monitored with MITI due to their effect on skin surface temperature. A tumor in breast disturbs the blood circulation within the breast. Imbalanced blood circulation beneath the skin affects the thermal distribution on the surface. The structure of breast made it easy to apply MITI techniques. Therefore, vast amount of the MITI studies were done on the breast tumor screening. Fat accumulated within the liver also disturbs the blood circulation of liver, and therefore, MITI can be effective for screening liver over the skin surface. There is a recent study in [108] which was conducted for classifying the fatty liver disease among

mice. They used MITI for capturing the skin temperature map over the liver and achieved 100% classification success.

Non-destructive methods used in medicine should be encouraged to reduce the harm on patients. It is well known that many screening and diagnosing techniques are invasive and cause some kind of harm such as frequently repeated mammograms, CT scans or X-ray imaging causing a risk of tumor development. Therefore, we believe that the use of MITI should be expanded since it has no negative effects on patients. Recently, many studies were conducted on employing MITI in medicine [48], [50], [67], [70], [108], [114], [117]. These kinds of efforts will increase the acceptance of MITI as a pre-diagnosis and treatment follow-up method.

Especially in the context of NAFLD, in [108] infrared thermal images were collected during experiments on mice and a fatty liver classification method was developed using machine learning techniques. The researchers extracted 9 texture features from every image and clustered them into 2 clusters as normal and steatosis. This study was inspirational for us to device this current research.

In the literature many recent studies include machine learning methods for automatic processing of thermal images [68]. However, deep learning methodologies have not been widely explored for MITI. Deep learning CNN architectures proved themselves as a powerful image processing tool. In this study, the performances of the texture analysis and 11 different CNN architectures were cooperatively evaluated, and remarkable results were reported by using different combinations of deep learning or machine learning techniques. The results show that feature extraction with CNN can find more detailed features than human eye.

The main research question of this study was to find out if deep learning methods as the feature extraction approach would perform well on thermal images. It was proven that pre-trained CNN architectures were powerful tools in MITI since these architectures achieved the highest classification performance over texture-based methods. The pre-trained networks were trained using more than a million images to recognize 1000 different objects which improves their learning capacity deeply. It was revealed in [108] that steatosis and inflammation affects infrared radiation release of the liver, therefore they analyzed texture features from the thermal images. In our study it was proven that deep learning architectures are better on differentiating the texture properties of thermal images in the NAFLD context.

Another question investigated in this study was the GLCM calculation of images. The default behavior of GLCM calculation is to scale the gray levels from 0-to-255 into 1-to-8 integer interval, which is called binning. Since the pixel values are scaled into a smaller range and the new values are rounded to integer values, many details may be lost during this scaling. Therefore, in this study GLCM calculation was modified to use the images' original gray level interval. Another default behavior of GLCM calculation is to cover all pixels in the image. However, in this study the region of the liver was the focus of our research and including non-liver area pixels into the calculations will decrease the steatosis information coming from liver area. Therefore, computation of the GLCM of the pixels that belong to liver area was proposed and applied to thermal images, which directs to another finding, combining 256-grey level and including only the pixels that belong to the liver area for GLCM calculation increased performance for AlexNet and DenseNet-201 methods as described in Results section.

Another finding in this study was to explore the performance of all feature sets of a feature selection method. In Figure 4.4 it can be clearly seen that not exploring all possible feature combinations may converge to a local optimum. However, generally the first few principal components were included in classification phase which contains about 95% of variation information of the data, but later component may include meaningful information of data as depicted in Table 4.2.

PCA has proven itself as a powerful feature selector throughout all evaluations against t-SNE method. The t-SNE method also produced good results that were close to PCA, but not better. In addition, t-SNE method's computation cost was high.

Due to working conditions of the clinic the thermal images are not standardized. Another limitation in the image collection phase was the non-standardized postures of patients who were mostly elderly or very young. Adult woman subjects were not included in this study, because the breasts cover up the liver and infrared radiation becomes insensible. For future studies, women subjects may be asked to raise their breasts to uncover the liver area, so that they would be included in such research tuned for women.

Currently the dataset is being improved with new thermal images. New methods for capturing images are being offered to clinic to improve the standardization among thermal images.

We believe that the findings in this research lead to new directions on MITI. New feature selection methods should be evaluated for different deep learning and machine learning methods. The main result of this study is to use different combinations of

methods to find out the highest performing combination. It is important to find the best combination of methods that show the best harmony with each other. This should guide researchers to develop more effective methodologies.

The main contribution of this study is evaluating human abdomen thermal images using machine and deep learning techniques for NAFLD classification. To our best knowledge, no studies have been conducted in this context on human subjects so far. Different contributions were also made during evaluations of experiments. It was revealed that along with grey level co-occurrence matrix (GLCM) based texture analysis, which was previously shown to be feasible in NAFLD on mice, CNN architectures are better to be used for feature extraction in this context. Another contribution was to modify GLCM calculation methodology to find pixel co-occurrences only within the upper triangular region-of-interest (ROI) similar to the shape of the liver instead of a rectangular ROI which is more common and includes more unrelated information about the temperature distribution over the liver and nearby regions, thus some methods' performances increase (AlexNet and DenseNet-201).

The results in this study reveals different directions for further studies. Improvements and modifications can be made on new pre-processing techniques on thermal images, which will improve revealing deeper features in the thermal images using CNN architectures. For example, different supervised or unsupervised feature selection methods can be evaluated. Another improvement can be done in training the CNN architecture with one channel grey level images, i.e., original raw images. In addition, in this study only one offset was calculated for GLCM computation, for future studies different offsets should be evaluated. Another research direction can be to develop a new CNN architecture by combining the evaluated CNN architectures that performed well during this research endeavor.

Chapter 5

Localized Quantification of Medical Infrared Thermal Images for Multiple Sclerosis Assessment and Monitoring

Multiple sclerosis (MS) is an autoimmune disease that affects 2.3 million people worldwide (75% are women, and ages vary between 20 and 40) [119], which may result in progressive disability or even worse, mortality [120]. MS is a disease of central nervous system (CNS) and optic nerves which causes inflammation and demyelination (scar tissue, sclerosis) [121]. Each MS patient encounters a particular combination of symptoms because of the variability in the location and degree of inflammatory demyelination within the CNS. Several kind of symptoms, such as, failure in tactile sensitivity or tingling, muscle fatigue, ataxia, dysarthria, and many others [122] may be observed in these patients. The degeneration of myelin sheath generally affects the extremities of the body. In severe cases both arms and legs are affected, and the patients need to use wheelchair.

Several studies in the last decade have shown that MS affects the thermal balance of body. In [123], it was revealed for the first time in the literature that the body core temperature is increased endogenously and increased fatigue. Later in 2015, a study by Leavitt et al. [124] demonstrated that the fatigue sensed by patient increases with elevated body core temperature. The findings of these studies depict that body temperature variations might be used to help the disease diagnosis.

In 2016, Papaléo et al. [122] used an infrared thermography (IRT) camera and captured 2D thermogram images of a patient who was diagnosed with MS in 2007. Then, these images were evaluated in terms of a possible correlation between the hot spots on the vertebrae and the level of pain patient suffering which may be a clue to devastation of nerve or not. This is the leading study to use IRT for MS evaluation and proposed that the

use of thermograms would be an effective approach to assess the influence of MS disease symptoms on the local body temperature.

In 2020, Pérez-Buitrago et al. [119] presented quantitative analysis of thermograms in which they captured IRT images of an MS patient and a healthy control and evaluated texture features of these images. A significant difference between the two samples was, especially in terms of uniformity feature.

In addition, cardiovascular system disorders can be monitored using MITI from body surface, due to the blood circulation [118]. Since MITI is a handy tool for producing skin temperature maps by absorbing the infrared radiation emitted from the body surface, other body functions other than the cardiovascular system can also affect the infrared radiation emission like the nervous system. There is heat generation while impulse travels along the nerve [125]. Along these lines, when the nerve fiber is degenerated, the effect on the heat distribution over the skin can be observed using IRT cameras. Therefore, this effect can be monitored using MITI system and the conditions beneath the skin can be interpreted without any invasive methods like electroneuromyography (ENMG).

Currently, Magnetic Resonance Imaging (MRI) and neurological examination are golden standards in monitoring MS patients. Patients come to follow-ups every one or two months, however MRI is performed once in a year because during follow-ups MR images are not fully correlated with neurological examination.

With this motivation, the aim of this study is to investigate the feasibility of MITI in monitoring MS damage on the limbs and to evaluate if there is correlation among patients' different images that belong to different visits/follow-ups. Thermal images were evaluated using different processing techniques and an adjusted image set was prepared for the physician to evaluate the degeneration-regeneration of the nerves. The main contribution of this study is to propose a novel approach in evaluating infrared thermography images acquired during different visits of a patient with regards to the disease progression or regression on limbs. To the best of our knowledge, no studies have been conducted in this context on human subjects so far.

5.1. Materials and Methods

5.1.1. Thermal Images

In this study the thermal images of two MS patients who suffer from demyelinated feet and worsening life standards were evaluated and a quantification method was

developed to track the changes between follow-ups. A healthy control was also included in the study. Here, 36 IRT images of legs coming from two patients and a healthy control were included for analysis. The diagnosis of these patients was made by neurologists using traditional diagnosis methods (magnetic resonance imaging and neurological examination approaches), and later patients came to the integrative medicine clinic where Dr. Yılmaz acquired their IRT images to use at the initial screening/visit and follow-up examinations.

Patient 1 has 12 images coming from three different examinations (visits) in 2018, 2019 and 2020. Patient 2 has 16 images coming from four different visits in 2021 at every 2 months. Healthy control has 8 images coming from two different visits in 2018 and 2020. Both patients and healthy control are male, and their birth years are 1994, 2004 and 1974 respectively. Patient 1 has been followed up for 10 years (only last 3 years of the treatment was followed up with IR thermography and he has recovered and currently working on a physical job), patient 2 has been monitored for 1 year, and healthy control for 2 years.

5.1.2. Processing of Thermal Images

The focus of this study was to evaluate the degeneration-regeneration of the nerves at the feet of two MS diagnosed patients who suffer from degeneration of nerves at their feet. Therefore, foot and leg parts below the knee were included in the region-of-interest (ROI) and rectangular coordinates containing these body parts were found on the gray level image manually. Gray level images were processed to extract background by applying Otsu's thresholding method [78] and a proper mask was applied to all images semi-manually. Different segmentation methods were evaluated, and Otsu's thresholding method surpassed other methods like active contours [126], region growing and local first order statistics. However, the images obtained in the clinic were not uniform and determining a threshold between foreground and background were not done fully automatically, few pictures, especially old ones were segmented with the help of MATLAB Image Segmenter. The segmented images were converted into a binary image where foreground and background were represented by ones and zeros respectively. The binarized image used as the background mask was applied onto the gray level image. The subsequent procedures were carried out with the masked gray level image, and background determined by the generated mask was not included in the following phases as well.

The first phase included properly coloring the images to be prepared for the evaluation of the physician. Therefore, segmented gray level images were colored using different level of color maps, which are available in the MATLAB tool. The quantification of thermal images then evaluated on raw thermal images, which the temperature levels were assumed as gray level intensity values.

The gray level leg images were divided into sub-regions to evaluate each region on its own. Each region of a patient was compared among consecutive visits of that patient and the gray level value difference between the visits were used to assess the progress of the treatment. Each region is divided into the number of rows and columns of blocks that can be defined by the user to show a quantitative demonstration of the region. For this purpose, within a region the mean value of pixels in a block was calculated and a vector was formed with the mean values. This vector represents the temperature distribution throughout the relevant region. The calculated mean vectors were compared while evaluating the treatment progress throughout the consecutive visits of a patient.

5.2. Results

The IRT images captured during routine examinations of patients in consecutive visits were not standardized due to working conditions of the clinic. Therefore, in the analysis and quantification efforts, the first step was to determine the locations of the legs and feet manually on the IRT images. In Figure 5.1, the initial step for ROI determination can be seen as the complete image on the left and manually cropped right and left leg images on the right, respectively.

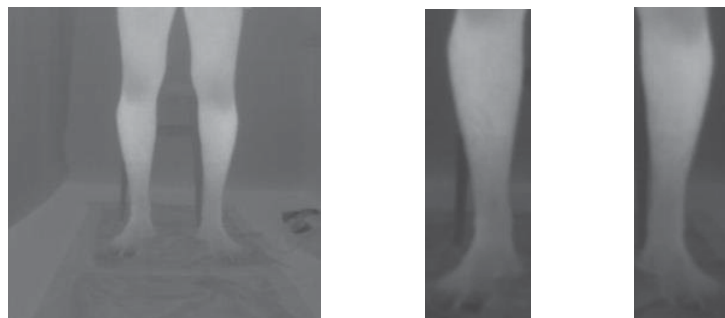


Figure 5.1 Extracting legs and feet from an IRT image from the first visit of the first patient (front view)

Secondly, segmenting the background from foreground was necessary to eliminate non-informative pixels from the image. In this step, segmentation using a classical approach called Otsu's method [78] was successful in most of the images, however few

of the images were segmented semi-manually with the help of an application in MATLAB called Image Segmenter. As shown in Figure 5.2, the IRT images labelled as a, b and c were captured during the first visit (V1) of the first patient (P1), and the images labelled with d and e were captured during the third visit (V3) of the same patient. The image in Figure 5.2-b represents the result of automatic thresholding on a non-standard image using Otsu's method where the foot was wrongfully assigned as the background. The infrared radiation acquired by the imaging system was relatively low over the skin of the foot due to the MS related nerve degeneration on that body part. After semi-manual segmentation, as depicted in Figure 5.2-c the successful segmentation of the leg and the foot was attained. On the other hand, as shown in Figure 5.2-e, where the same right leg image of patient 1 captured during the third visit, automatic thresholding was sufficient to obtain the leg and the foot without any manual intervention. We believe that this can also be an indication of the recovery/regeneration of the nerves in the foot which in turn caused increased heat throughout the nerve and increased IR radiation over the skin.

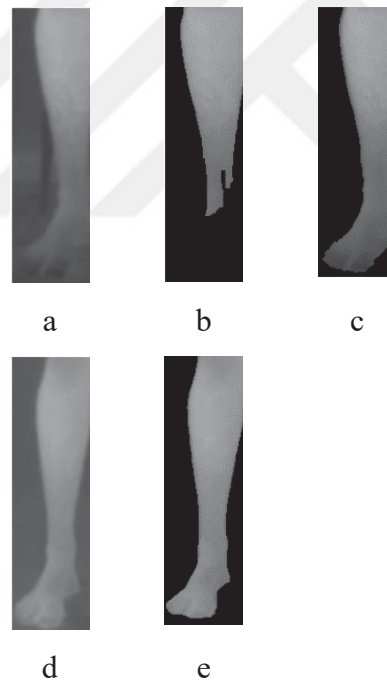


Figure 5.2 Automatic thresholding results (Patient 1, first row: visit 1, second row: visit 3)

The thermal examination on the body is performed on specific areas related to specific diseases. In this study, leg images of patients were evaluated since they suffer from the degeneration of lower limbs. The next step after image segmentation was to color the images to prepare for the evaluation of the physician. Different visit images were placed together in the figures Figure 5.3 and Figure 5.4. Consecutive visit images

were placed consecutively in the figures. The first line in Figure 5.3, the images a-b-c and d-e-f are the three consecutive visits of patient 1's right and left legs images, respectively, from the front view where the second row is from the back view in the same arrangement.

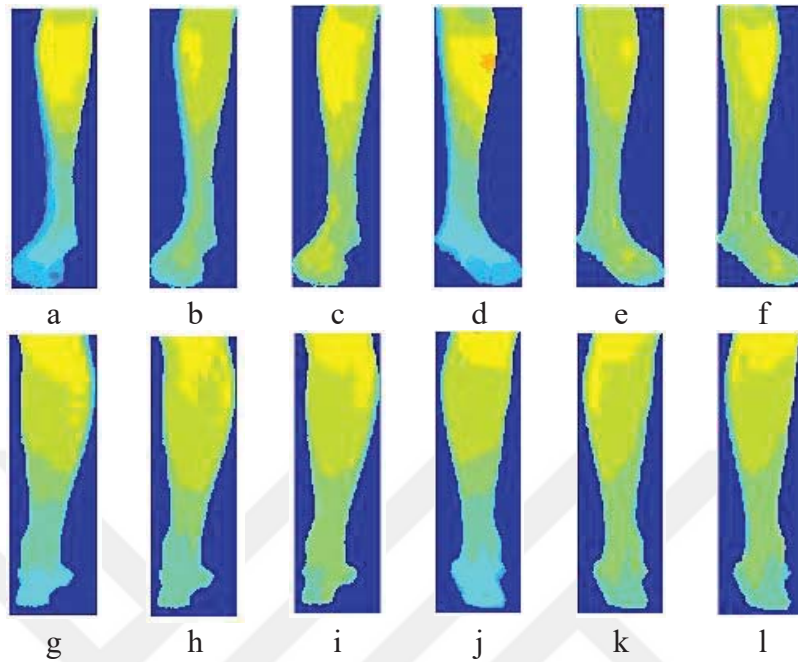


Figure 5.3 Colored thermal images of the three visits of patient 1 (a-b-c and g-h-i right leg images of three visits from front and back view respectively, d-e-f and j-k-l left leg images of three visits from front and back view respectively)

The first line in Figure 5.4, the images a-b-c-d and e-f-g-h are the four consecutive visits of patient 2's right and left legs images, respectively, from the front view where the second row is from the back view in the same arrangement.

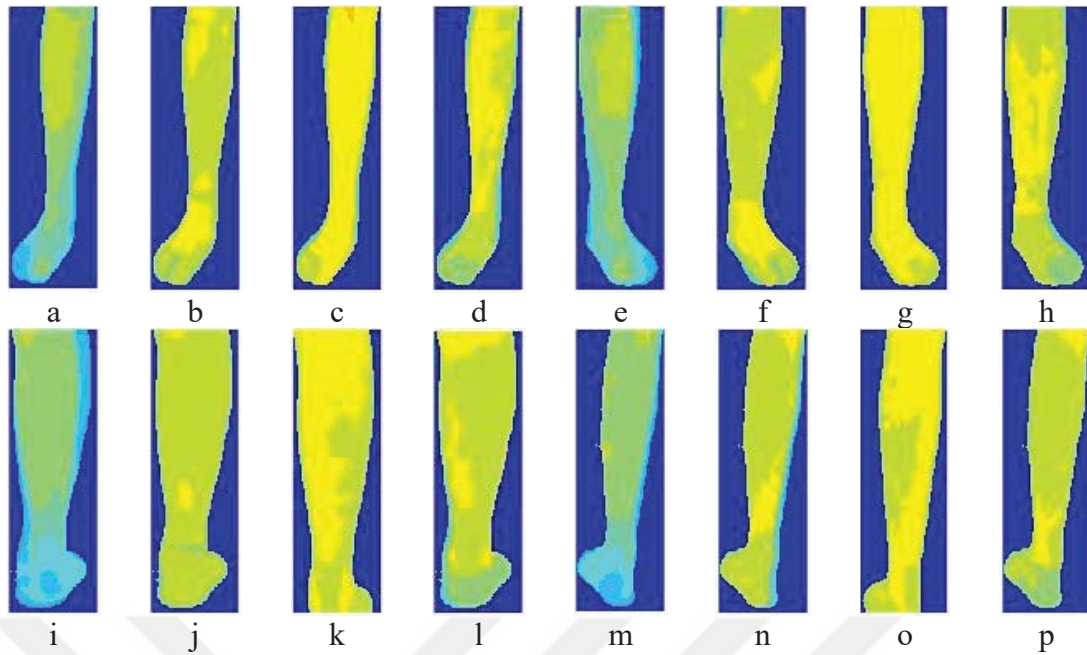


Figure 5.4 Colored thermal images of the four visits of patient 2 (a-b-c-d and i-j-k-l right leg images of four visits from front and back view respectively, e-f-g-h and m-n-o-p left leg images of four visits from front and back view respectively)

In both figures Figure 5.3 and Figure 5.4, the blue parts in feet represent the extend of the degeneration spread.

In the next step, the gray level leg images of patients were divided into sub-regions to focus only on the targeted region, in this case the feet. Each sub-region was divided into blocks. As a demonstrative example shown in Figure 5.5-a and b, the front view image of the right leg of patient 1 captured during visit 1 was divided into 3 sub-regions, and as in Figure 5.5-c, the sub-regions were divided into 9 blocks (3 rows and 3 columns).

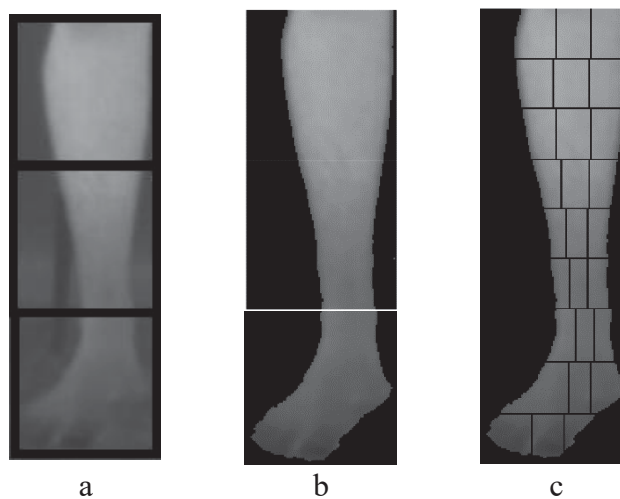


Figure 5.5 A sample image is presented to show how the dividing image into subregions and blocks is performed (Patient 1, visit 1, right leg, front view)

Once we obtained the blocks corresponding to the feet, the mean pixel intensity (gray level) value of each block for each subject and each visit was computed and saved for further comparative analysis. Dividing into blocks made anatomical registration/overlaying possible, so that comparison between visits on similar, if not the same, parts of the foot became feasible. However, we observed that pixel-by-pixel comparison would mislead the procedure due to the non-standard position of the patient during visits. It is most likely that the pixel values of the heatmaps corresponding to consecutive visits would not overlap pixel-by-pixel, and different pixels would be compared leading to incorrect quantitative analysis outcome. Therefore, the regions were divided vertically and horizontally into blocks. Since sub-regions coming from consecutive visits were divided into the same number of blocks, the skin surface they covered remained similar even though the number of pixels contained in the blocks on the same row and column changed. To be more specific, when the foot images coming from the follow-up visits were divided into the same number of blocks, they still showed the same toe even if the number of pixels contained in the blocks showing the same toe was changed. Therefore, the comparison was performed by matching the pixel intensity means of the blocks located in the same row and column within the same region. The front view images of right foot from patient 1 captured during the examinations at visit 1, visit 2, and visit 3 are displayed in Figure 5.6-a, b, and c, respectively. The images in Figure 5.6 clearly supports the idea proposed in this study that dividing the regions into blocks would increase the comparison accuracy of the same area even they encompass different number of pixels.

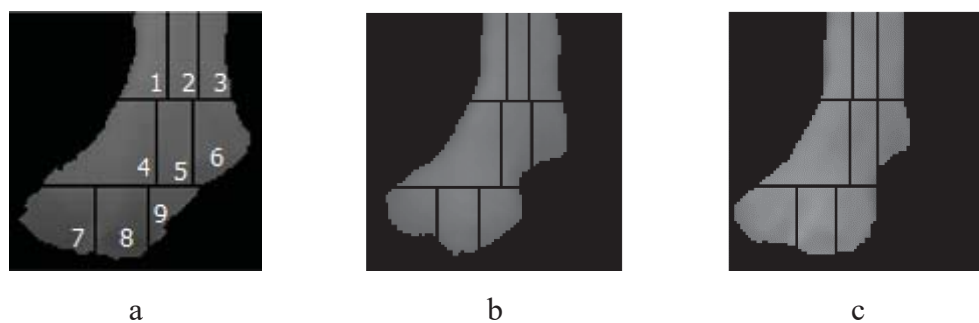


Figure 5.6 Patient 1, right foot images acquired during different visits (a: visit 1, b: visit 2, and c: visit 3)

In the next step, a vector was formed by calculating the mean gray level of the pixel values (Mean GLV) in the block itself, starting from the top left of the blocks in the region to be evaluated, in this case front view of feet images, and a 1-by-9 size vector was formed

since the foot region was divided into 3 rows and 3 columns. Right and left feet images of patient 1, patient 2 and healthy control were processed to form the “vectors of the blocks mean” contained in the foot region. Right and left feet mean vectors of all subjects can be seen in Figure 5.7. Right and left feet images were grouped together to perform a reasonable comparison with healthy control feet images. Therefore, the results were combined where the first column contains the front view of the right feet, and the second column contains the front view of left feet. The first, second, and third rows in the figure contain the results of MS patients and healthy control, respectively. Patient 1 visited the clinic once a year, and totally three times in 2018, 2019, and 2020. Patient 2 visited the clinic 4 times in 2021 in 2-month intervals. Healthy control visited the clinic two times in 2018 and 2020.

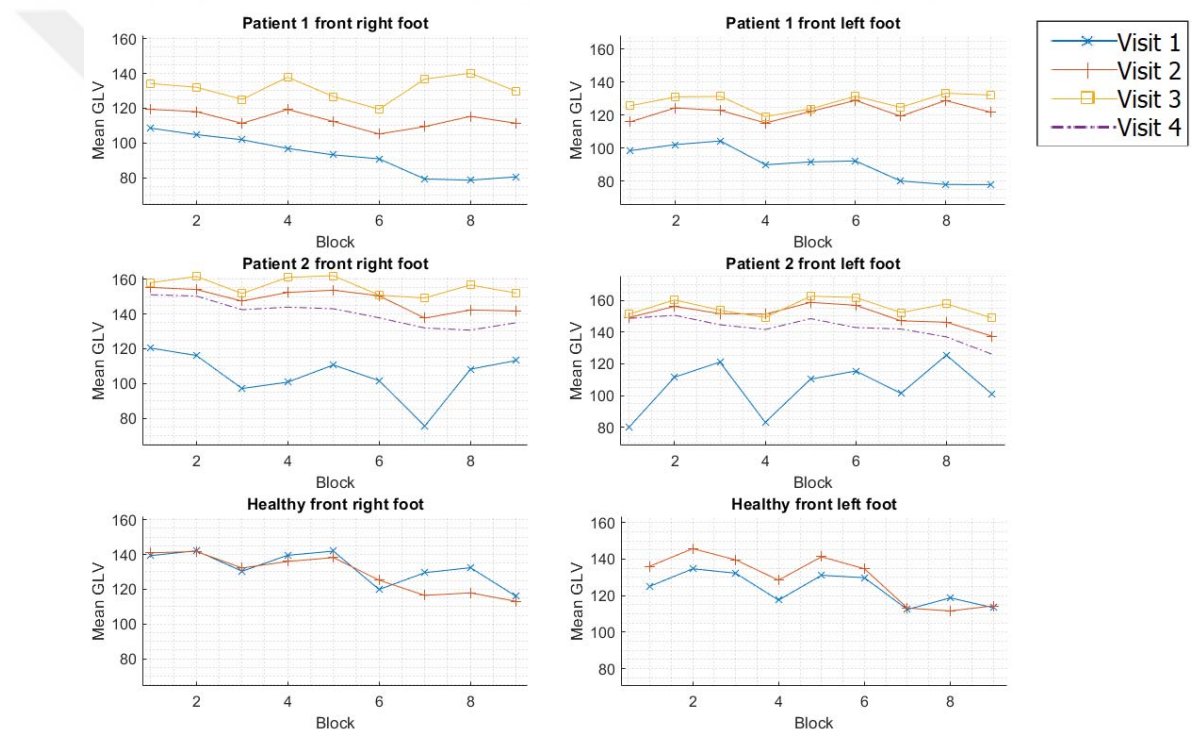


Figure 5.7 Comparison of mean gray levels corresponding to 9 blocks of the right and left feet for MS patients and healthy control from front view during different visits.

In this case the mean vectors of the blocks contain 9 elements, due to foot region was divided into 3 rows and 3 columns. Block-mean vectors of a subject, coming from consecutive visits, were compared with each other using visit-wise subtraction for the same foot from the same view. Finally, the mean of the subtraction results from the region (foot) was calculated. Table 5.1 and Table 5.2 summarize the subtraction results and means of right and left feet of subjects respectively. The progression of the MS disease

can be seen in Table 5.1 and Table 5.2. Patient 1 has constant increase which shows that he was close to full recovery. For Patient 2, there is an increase throughout consecutive visits except for the last visit where there is a moderate decrease that is correlated with the findings observed during clinical examinations. The differences obtained for healthy control can be considered as normal fluctuations.

Table 5.1 Differences of block-mean vectors for the right feet

	Visit difference	Block 1	Block 2	Block 3	Block 4	Block 5	Block 6	Block 7	Block 8	Block 9	Mean
Patient 1	Visit 2-1	10.86	13.21	9.49	22.41	19.23	14.28	30.12	36.74	30.82	20.80
Patient 1	Visit 3-2	14.79	14.06	13.73	18.59	14.31	14.33	27.37	24.81	18.37	17.82
Patient 2	Visit 2-1	34.92	37.95	50.29	51.57	43.04	48.81	62.11	34.03	28.49	43.47
Patient 2	Visit 3-2	2.68	7.51	4.36	8.68	8.30	0.40	11.56	14.42	10.30	7.58
Patient 2	Visit 4-3	-6.90	-11.28	-9.34	-17.12	-19.02	-13.04	-17.26	-25.97	-17.05	-15.22
Healthy	Visit 2-1	1.61	-0.40	1.84	-3.57	-3.71	5.32	-13.05	-14.48	-2.88	-3.26

Table 5.2 Differences of block-mean vectors for the left feet

	Visit difference	Block 1	Block 2	Block 3	Block 4	Block 5	Block 6	Block 7	Block 8	Block 9	Mean
Patient 1	Visit 2-1	17.49	22.3	18.49	25.36	30.58	36.74	39.31	50.91	43.91	31.68
Patient 1	Visit 3-2	9.72	6.62	8.54	3.85	1.60	2.55	5.37	4.44	10.43	5.90
Patient 2	Visit 2-1	68.99	44.60	30.54	68.15	48.36	41.41	45.72	20.71	36.36	44.98
Patient 2	Visit 3-2	2.14	4.05	2.21	-2.12	3.90	4.96	5.20	11.59	11.46	4.82
Patient 2	Visit 4-3	-2.72	-9.71	-9.21	-7.52	-14.13	-18.97	-10.38	-20.84	-22.82	-12.92
Healthy	Visit 2-1	10.97	11.03	7.30	10.95	10.13	4.89	0.77	-7.16	1.01	5.54

5.3. Discussion and Conclusions

Multiple sclerosis is caused by the body's immune response attacks against central nervous system which degenerate the myelin sheath covering the axon. Action potentials are the electrical signals by which the nerves communicate with each other. The communication via action potentials between nerves is deteriorated when the myelin sheath is degenerated (demyelination). Regeneration of demyelinated nerves is a subject that needs to be addressed further.

MS patients generally suffer from degeneration that occurs on extremities. Both patient 1 and patient 2 came to Dr. M.M. YILMAZ Integrative Medicine Clinic with similar complaints after being diagnosed with MS disease in 2011 and 2021, respectively. Both patients had degenerations on their lower extremities, loss of balance and suffer

from hyperactive deep tendon reflexes. Patient 1 was unable to walk at the beginning of the treatment process but was able to fully recover. Patient 2 visited the clinic for the first time in 2021 and currently pursuing the treatment.

In the clinic different treatment and examination processes were applied to the patients such as the magnetic field treatments (peripheral magnetic stimulation [127], transcranial magnetic stimulation [128]), electro acupuncture [129], herbal treatments (oral and IV-intravenous), systemic ozone therapy (major auto haemo therapy) [130]. The cerebrospinal fluid (CSF) was (and is being for patient 2) provoked with magnetic field treatments, and herbal treatments were applied to regenerate the damaged (demyelinated-degenerated) nerve fibers. The progression of regeneration, degeneration or stability was (and is) followed up by combination of anamnesis, capturing thermal images using thermograph and neurological examination [131]. It is important that the three of them, anamnesis, thermal images, and neurological examination overlap and support each other. CSF pressure was (and is being) measured with craniosacral therapy [132] during follow-ups, because a decrease on CSF pressure is a bad sign for MS patients.

Currently MS disease is diagnosed with a combination of anamnesis, standard blood tests, medicated brain and spinal cord magnetic resonance (MR) imaging and CSF examination. However, treatment procedure is not easy and well defined. Generally, three different goals are aimed [133]. The first aim is to treat the patient who comes with a sudden attack, high-dose cortisone treatment is given intravenously for 3-10 days or sometimes a blood exchange called plasmapheresis [134] is performed during this attack period. The second aim is to stop the attacks and to try to prevent the progression of the disease. For this purpose, sometimes injections and pills can be given for a long time. The third aim is to treat the complaints of patients whose quality of life is impaired due to the disease. There are physical therapy methods, different muscle relaxants, pain killers, drugs to prevent urinary incontinence, drugs used in sexual dysfunction to ease the complaints of the patients. During follow-ups, interval between patient visits are 1-2 months and MR images are captured once in a year. Because during follow-ups MR is not fully correlated with neurological examination [135].

Skin temperature decreases towards to the end of the extremities. In Figure 5.7, the temperature decrease can be seen throughout the mean vector, since the first block is at the top left of the image higher order blocks (blocks 7, 8, and 9) represents the end of the extremity. There are fluctuations on the first visit of patient 2, which means there is a pathological disorder, however there is no such fluctuations for patient 1. Because the last

part of the treatment of patient 1 was followed up with IR thermography when stability was maintained, and the patient was close to full recovery. Also, there is stabilization for patient 2 at the following visits' graphs, which means the patient responded well to treatment.

There is certain amount of decrease in the heat generated by the nerve if it is damaged, which makes it possible to monitor the state of the disease with the IR thermography if the clinical examinations like neurological examinations, blood tests etc. support the same findings. Therefore, increase, decrease, and stabilization of the temperature means increase, decrease, and stability of regeneration process, respectively.

In this study thermal images of two patients and a healthy control were captured in a private integrative medicine clinic were evaluated. The aim of this study was to quantify the thermal images of MS diagnosed patients and make it possible to provide a numerical measurement to physician to quantify what he/she sees on the image. This will allow physicians to do evaluation in a more objective and generic manner. Since they evaluate the numbers not the images, the decision will be easier to discuss.

In figures Figure 5.3 and Figure 5.4, the thermal images of the two patients were colored which will enable physician to investigate the images and assess the disease with better accuracy. However, the thermal images can be quantified better when the thermal information in the image is further processed. It is necessary to extract meaningful information from the raw data to present to the physician to assess the disease properly.

In Figure 5.7, the right and left feet images of subjects were displayed as means' vectors of blocks. The healthy control images were taken with two-year intervals, and both mean vectors were highly correlated which means there was no substantial difference between the visits. When figures from patients 1 and 2 were compared to healthy control figures, the thermal difference of figures apparently proves that healthy and unhealthy thermograms have different characteristics.

MS treatment of patient 1 was performed between the years 2011 and 2020, however, thermograms were acquired and recorded only in the last three years of treatment, because in the clinic thermography-based monitoring of MS treatment started in 2018. Therefore, the graphs of patient 1 are stable and there is a constant temperature increase which means there is regeneration in the nerve fibers that were affected by the MS disease.

The treatment of patient 2 started in 2021 and is currently underway. In the beginning of the treatment, he was not able to lift his toe. It can be seen in Figure 5.7 (the

front view images of the right foot from the first visit of patient 2) that 7th block that corresponds to the patient's toe has the lowest mean value. There are significant variations among different blocks in the first visit, especially on the front view vectors of both feet. However, the vectors of consecutive visits do not have such variations as it is in visit 1 due to the positive response obtained during treatment. There is a small decrease of means when the patient 2 came to the 4th visit which is also in parallel with the clinical observations of the physician. This situation indicates that change towards improvement, worsening, or stabilization can be observed using IR thermogram images.

In this study different patients with different visit intervals were evaluated, patient 1 has one year, patient 2 has 2 months, and healthy control has 2 years between visits. It is observed that quantitative analysis of thermal images can be informative and may have additional value for the assessment of MS patients in conjunction with examinations and tests that the physicians are routinely using in their clinical practice. The assessment of thermograms requires a certain level of expertise which is not common in traditional and integrative medicine clinics. Interpreting the thermal images in addition to the clinical findings can help physicians monitor the progress of patients. The physicians have to know how to adjust certain colormaps to correctly visualize the thermal image, focus on the regions related to a specific disease under consideration and know how to interpret what he/she sees in the image. Raw thermal images are gray level images which can be seen in Figure 5.1 and the gray level image is not informative for the human eye. Therefore, the image should be colored, and necessary details in the image should be revealed by adjusting the image properties such as colormaps and temperature range. Special colormaps should be applied to image to make the targeted pathology visible. Even with the colored and adjusted image human eye may not clearly quantify the difference and may not precisely determine the stage of a disease. The method proposed in this study quantifies the local thermal properties of the patient by presenting numbers such as the mean intensity value which will help physician to interpret the findings in the thermal image. We believe that findings in this study revealed the promising future of IR based thermal imaging in medicine for pre-diagnosis/screening and follow-up procedures. Therefore, thermal imaging may be a feasible alternative to invasive and costly (both money- and time-wise) screening methods.

The thermal images analyzed in this study were not uniform and standard, therefore it was a challenge while processing images automatically. One of the consequences of this condition was that the fully automatic segmentation approaches did not perform well,

and semi-automatic segmentation was applied to some of the non-standard images. Different view images may help to improve the performance of investigation and may provide more information for evaluation. In this case lateral view of foot may provide extra information.



Chapter 6

Conclusions and Future Prospects

6.1. Conclusions

Diagnosis method should give minimum or no harm to the patient. However, many diagnosis methods may cause some sort of damage to the patient. For example, mammogram is the standard diagnosis method for breast cancer, but this test itself can cause the initiation of a tumor in the breast due to the ionizing radiation used during the test. It is an urgent need to develop more harmless methods for patient's comfort and wellbeing. The IR thermographs do not contain any harmful radiation, but they only absorb infrared radiation naturally emitted from the body. Even no contact is needed for this approach. This makes the thermal imaging method a valuable adjunct diagnosis method due to its harmless nature. One of the collaborators in this research is Dr. M.M. Yılmaz Clinic, which is one of the biggest traditional and complementary medicine clinics in Türkiye, and the main physician in this clinic is the first doctor in the country that used thermographs for pre-diagnosis. The doctor (Dr. Mustafa Mücahit Yılmaz) examined almost 4000 patients since 2012. It is important to introduce this huge experience to other interested physicians. Yet this method did not gain enough interest among medical world. Experienced medical experts are scarce, so smart systems are needed to help unexperienced doctors and technicians for gaining the knowledge of medical thermal imaging faster and easier. With this motivation the aim of this study was to develop automated processing and classification methods for evaluation of medical thermal images.

Medical infrared thermal imaging is a non-invasive, low cost and easily applied to patients without any restriction. Due to these advantages this method will gain the attention of physicians and as well as the experts in other fields. Human body is homeothermic, it can generate and evacuate heat, that is why this working principle of body is fully correlated with MITI. The heat distribution of a healthy individual's body is balanced. Health problems that occur in body can break down the heat balance locally or

in general. The relationship of body heat balance and illness was first documented in 400 BC. An infrared (IR) thermogram is a heat map that displays the heat distribution of the target as an image. The IR thermography in healthcare was first used in late 1950s. In 1956, R. Lawson found out that a tumor tissue increased surface temperature of the skin over itself more than the skin over the normal tissue did [136]. The focus was the breast cancer detection. Since 1995 there has been an increased interest for the IR thermography due to the improvements in IR camera technology and image processing algorithms [1]. The first application area of the thermography in medicine is breast cancer screening, a sample of latest studies can be found in [137]–[146], [147]–[156], [111], [113], [157]–[163]. There are different application areas in medicine other than the breast cancer that the IR thermography is used, the following references can be investigated for further information: [164]–[173], [174]–[183], [184]–[193], [194]–[203], [204]–[213], [214]–[223], [224]–[234], [235]–[244]. Therefore, the emergence of improved image processing techniques has given chance to apply infrared thermal imaging to more complex areas.

Since MITI is a relatively new area, the experts who have experience on evaluating the thermograms are low in numbers. One of the goals of this study is to quantify the experience of the experts which will allow this experience becoming commonly available. This will also allow the common experience growing of MITI to gain pace.

6.2. Societal Impact and Contribution to Global Sustainability

Today, social problems and global sustainability are among major problems which threatens the life on our planet. This is because of the greedy life style of the last century. Therefore, it is important to reverse this situation by prioritizing the social problems and global sustainability in the developing projects.

Developing non-invasive and radiation free methods in medicine is an important subject for this goal. Many different monitoring methods are invasive and contains harmful materials, like x-rays. Thermal diagnosis is a promising monitoring technique for healthcare due to its harmless nature. Since no radiation or any other harmful material is used in this method, there is no limit for the frequency or amount of usage for patient's health. For example, the generally accepted diagnosis method for breast cancer is mammogram, but in this method, radiation is used to examine the patient. It is possible to expand the use of IR thermography in general hospitals for pre-diagnosis of certain

diseases. The diseases should be focused which are highly frequent in the population. The economic impact will be higher when expensive techniques are replaced with cheaper techniques used on highly frequent diseases.

This study is mostly related with the United Nations Sustainable Development Goals of number 3, “Good Health and Well-Being”. Since the method is easy to apply and cheap for installation, it can be set up to many medical centers where it will be easy for many people to reach a harmless and cheap complementary diagnosis method. It is also more or less related with other goals, like economic goals, because you can get a sustainable and harmless diagnosis method without spending much money. Since this method is radiation free, it will also contribute to the goals related to clean energy and climate. This cheap method will also improve the health service accessibility in low income countries.

6.3. Future Prospects

The results of this study reveal different directions for further studies. Current and future research efforts are aiming and will aim at studying different aspects of MITI for it to become an accepted pre-diagnosis tool for certain diseases and conditions in clinical practice. Many researchers believe that this technology has this potential and there are many clinics and experts around the world that employ MITI in their diagnosis (or pre-diagnosis) process. It is obvious that the automatization and standardization of the diagnosis is highly necessary. Along these lines several parallel studies are underway aiming at the automatic detection of certain diseases using conventional machine learning and deep learning approaches from medical thermal images. Possible research directions include the detection of pain centers from the dorsal view of the upper body or finding the varicose vein extension on the legs using thermal images, etc.

Improvements and modifications can be made on new pre-processing techniques on thermal images, which will improve revealing deeper features in the thermal images using CNN architectures. For example, different supervised or unsupervised feature selection methods can be evaluated. Another improvement can be done in training the CNN architecture with one channel gray level images, i.e., original raw images. In addition, in liver steatosis classification study only one offset was calculated for GLCM calculation, for future studies different offsets should be evaluated. Another research

direction can be to develop a new CNN architecture by combining the evaluated CNN architectures that performed well during this research endeavor.

For MS assessment study, further studies should include lateral view thermogram of the feet for assessing the disease comprehensively. Another aspect for further studies is to focus on other body parts who suffer from MS disease and have degeneration on associated nerves. In MS assessment study degenerated nerves in the feet were investigated, and the regeneration was quantified in accordance with clinical findings. Another aspect for the new studies should be evaluating different diseases that are relevant with body temperature. Such diseases can be interpretable and easily trackable when heatmaps of the body parts are generated with thermal imaging and these maps are tracked during consecutive visits using quantification approach as it is proposed in this study. Comparing thermograms may provide an easy and non-invasive method for assessing the status of the disease.

The methods evaluated during this study should be applied to different health problems that are related with heat balance of the body. With this motivation, computer-aided methods should be developed for the disorders like backache, sinus inflammation, liver steatosis, varicose, thymus gland irregularities, and multiple sclerosis.

BIBLIOGRAPHY

- [1] L. J. Jiang *et al.*, A perspective on medical infrared imaging, *J. Med. Eng. Technol.*, vol. 29, no. 6, pp. 257–267, Jan. 2005.
- [2] D. J. Casa, L. E. Armstrong, R. Carter, R. Lopez, B. Mcdermott, and K. Scriber, Historical Perspectives on Medical Care for Heat Stroke, Part 1: Ancient Times Through the Nineteenth Century: A Review of the Literature, *Athl. Train. Sport. Heal. Care*, vol. 2, no. 3, pp. 132–138, Jan. 2010.
- [3] E. F. J. Ring and K. Ammer, Infrared thermal imaging in medicine, *Physiol. Meas.*, vol. 33, no. 3, pp. R33–R46, Mar. 2012.
- [4] S. A., K. H.S., and G. S., Infrared thermography and image analysis for biomedical use, *Period. Biol.*, vol. 113, no. 4, pp. 385–392, 2011.
- [5] J. Mercer, L. De Weerd, Å. Miland, and S. Weum, Pre-, Intra-, and Postoperative Use of Dynamic Infrared Thermography (DIRT) Provides Valuable Information on Skin Perfusion in Perforator Flaps Used in Reconstructive Surgery, *Proc. Inframation*, vol. 11, no. 1889, pp. 313–320, 2010.
- [6] R. C. Purohit and M. D. McCoy, Thermography in the diagnosis of inflammatory processes in the horse., *Am. J. Vet. Res.*, vol. 41, no. 8, pp. 1167–1174, Aug. 1980.
- [7] T. A. Turner, Diagnostic thermography., *Vet. Clin. North Am. Equine Pract.*, vol. 17, no. 1, pp. 95–114, Apr. 2001.
- [8] A. L. Eddy, L. M. Van Hoogmoed, and J. R. Snyder, The role of thermography in the management of equine lameness, *Vet. J.*, vol. 162, no. 3, pp. 172–181, Nov. 2001.
- [9] L. C. Holmes, E. M. Gaughan, D. A. Gorondy, S. Hogge, and M. F. Spire, The effect of perineural anesthesia on infrared thermographic images of the forelimb digits of normal horses, *Can. Vet. J.*, vol. 44, no. 5, pp. 392–396, May 2003.
- [10] S. Bagavathiappan *et al.*, Infrared thermal imaging for detection of peripheral vascular disorders, *J. Med. Phys.*, vol. 34, no. 1, pp. 43–47, Jan. 2009.
- [11] F. J. Ring, Pioneering progress in infrared imaging in medicine, *Quant. Infrared Thermogr. J.*, vol. 11, no. 1, pp. 57–65, 2014.
- [12] D. L. Balageas, A brief history of QIRT concept, structures and community, *Quant. Infrared Thermogr. J.*, vol. 13, no. 1, pp. 109–125, 2016.
- [13] J. Singh and A. S. Arora, Automated approaches for ROIs extraction in medical

- thermography: a review and future directions, *Multimed. Tools Appl.*, vol. 79, no. 21–22, pp. 15273–15296, 2020.
- [14] M. P. Manda and H. S. Kim, A fast image thresholding algorithm for infrared images based on histogram approximation and circuit theory, *Algorithms*, vol. 13, no. 9, p. 207, Aug. 2020.
- [15] J. Huamyun and A. S. Malik, Multispectral and thermal images for acne vulgaris classification, *2011 Natl. Postgrad. Conf. - Energy Sustain. Explor. Innov. Minds, NPC 2011*, pp. 1–4, 2011.
- [16] S. Bardhan, S. Nath, and M. K. Bhowmik, Evaluation of background subtraction effect on classification and segmentation of knee thermogram, in *2017 8th International Conference on Computing, Communication and Networking Technologies (ICCCNT)*, Jul. 2017, pp. 1–7.
- [17] K. Rani, M. Kalra, and R. Kumar, *Infrared Thermography-Based Facial Classification Using Machine Learning*, Springer, Singapore, 2022, pp. 275–284.
- [18] Hairong Qi and J. F. Head, Asymmetry analysis using automatic segmentation and classification for breast cancer detection in thermograms, in *2001 Conference Proceedings of the 23rd Annual International Conference of the IEEE Engineering in Medicine and Biology Society*, 2001, vol. 3, pp. 2866–2869.
- [19] M. Etehadtavakol, E. Y. K. Ng, V. Chandran, and H. Rabbani, Separable and non-separable discrete wavelet transform based texture features and image classification of breast thermograms, *Infrared Phys. Technol.*, vol. 61, pp. 274–286, Nov. 2013.
- [20] T. Jakubowska, B. Wiecek, M. Wysocki, C. Drews-Peszynski, and M. Strzelecki, Classification of breast thermal images using artificial neural networks, in *The 26th Annual International Conference of the IEEE Engineering in Medicine and Biology Society*, 2004, vol. 3, pp. 1155–1158.
- [21] Y. Sahraoui, A. Korichi, C. A. Kerrache, M. Bilal, and M. Amadeo, Remote sensing to control respiratory viral diseases outbreaks using Internet of Vehicles, *Trans. Emerg. Telecommun. Technol.*, p. e4118, Sep. 2020.
- [22] S. L. Aarthy and S. Prabu, Classification of breast cancer based on thermal image using support vector machine, *Int. J. Bioinform. Res. Appl.*, vol. 15, no. 1, pp. 51–67, 2019.
- [23] B. Sankur, Survey over image thresholding techniques and quantitative performance evaluation, *J. Electron. Imaging*, vol. 13, no. 1, p. 146, 2004.

- [24] J. Josephine Selle, A. Shenbagavalli, N. Sriraam, B. Venkatraman, M. Jayashree, and M. Menaka, Automated recognition of ROIs for breast thermograms of lateral view-a pilot study, *Quant. Infrared Thermogr. J.*, vol. 15, no. 2, pp. 194–213, 2018.
- [25] Q. Li, W. Cai, X. Wang, Y. Zhou, D. D. Feng, and M. Chen, Medical image classification with convolutional neural network, *2014 13th Int. Conf. Control Autom. Robot. Vision, ICARCV 2014*, vol. 2014, no. December, pp. 844–848, 2014.
- [26] O. Heriana and I. Soesanti, Tumor size classification of breast thermal image using fuzzy C-Means algorithm, *Proceeding - 2015 Int. Conf. Radar, Antenna, Microwave, Electron. Telecommun. ICRAMET 2015*, pp. 98–103, 2016.
- [27] S. Bardhan and M. K. Bhowmik, 2-Stage classification of knee joint thermograms for rheumatoid arthritis prediction in subclinical inflammation, *Australas. Phys. Eng. Sci. Med.*, vol. 42, no. 1, pp. 259–277, 2019.
- [28] I. Farady, C. Y. Lin, A. Rojanasari, K. Prompol, and F. Akhyar, Mask Classification and Head Temperature Detection Combined with Deep Learning Networks, *2020 2nd Int. Conf. Broadband Commun. Wirel. Sensors Powering, BCWSP 2020*, pp. 74–78, 2020.
- [29] N. Arora *et al.*, Effectiveness of a noninvasive digital infrared thermal imaging system in the detection of breast cancer, *Am. J. Surg.*, vol. 196, no. 4, pp. 523–526, 2008.
- [30] E. Y. K. Ng, Y. Chen, and L. N. Ung, Computerized breast thermography: Study of image segmentation and temperature cyclic variations, *J. Med. Eng. Technol.*, vol. 25, no. 1, pp. 12–16, 2001.
- [31] P. T. Kuruganti and Hairong Qi, Asymmetry analysis in breast cancer detection using thermal infrared images, in *Proceedings of the Second Joint 24th Annual Conference and the Annual Fall Meeting of the Biomedical Engineering Society [Engineering in Medicine and Biology, 2002*, vol. 2, pp. 1155–1156.
- [32] S. T. Kakileti and K. Venkataramani, Automated blood vessel extraction in two-dimensional breast thermography, *Proc. - Int. Conf. Image Process. ICIP*, vol. 2016-Augus, pp. 380–384, 2016.
- [33] S. V. Francis and M. Sasikala, Automatic detection of abnormal breast thermograms using asymmetry analysis of texture features, *J. Med. Eng. Technol.*, vol. 37, no. 1, pp. 17–21, 2013.
- [34] J. Kerr, *Review of the effectiveness of infrared thermal imaging (thermography) for population screening and diagnostic testing of breast cancer (DARE structured*

- abstract*), vol. 3, no. 3. 2004.
- [35] H. G. Zadeh, J. Haddadnia, N. Ahmadinejad, and M. R. Baghdadi, Assessing the potential of thermal imaging in recognition of breast cancer, *Asian Pacific J. Cancer Prev.*, vol. 16, no. 18, pp. 8619–8623, 2016.
- [36] E. Y.-K. Ng, S. C. Fok, Y. C. Peh, F. C. Ng, and L. S. J. Sim, Computerized detection of breast cancer with artificial intelligence and thermograms, *J. Med. Eng. Technol.*, vol. 26, no. 4, pp. 152–157, Jan. 2002.
- [37] N. Lanisa, N. S. Cheok, and L. K. Wee, Color morphology and segmentation of the breast thermography image, in *2014 IEEE Conference on Biomedical Engineering and Sciences (IECBES)*, Dec. 2014, no. December, pp. 772–775.
- [38] H. Ghayoumi Zadeh, J. Haddadnia, O. Rahmani Seryasat, and S. M. Mostafavi Isfahani, Segmenting breast cancerous regions in thermal images using fuzzy active contours, *EXCLI J.*, vol. 15, pp. 532–550, 2016.
- [39] N. Kavya, N. Usha, N. Sriraam, D. Sharath, and P. Ravi, Breast Cancer Detection using Non Invasive Imaging and Cyber Physical System, in *2018 3rd International Conference on Circuits, Control, Communication and Computing (I4C)*, Oct. 2018, pp. 1–4.
- [40] FDA, Breast Cancer Screening: Thermogram No Substitute for Mammogram, *Medical Devices*, 2017. <https://www.fda.gov/consumers/consumer-updates/breast-cancer-screening-thermogram-no-substitute-mammogram> (accessed Jun. 16, 2019).
- [41] N. Köşüş, A. Köşüş, M. Duran, S. Simavli, and N. Turhan, Comparison of standard mammography with digital mammography and digital infrared thermal imaging for breast cancer screening, *J. Turkish Ger. Gynecol. Assoc.*, vol. 11, no. 3, pp. 152–157, 2010.
- [42] S. Akbarian, G. Delfi, K. Zhu, A. Yadollahi, and B. Taati, Automated Non-Contact Detection of Head and Body Positions During Sleep, *IEEE Access*, vol. 7, pp. 72826–72834, Aug. 2019.
- [43] S. T. Kakileti, A. Dalmia, and G. Manjunath, Exploring deep learning networks for tumour segmentation in infrared images, *Quant. Infrared Thermogr. J.*, vol. 17, no. 3, pp. 153–168, Jul. 2020.
- [44] M. Gogebakan and H. Erol, A New Semi-supervised Classification Method Based on Mixture Model Clustering for Classification of Multispectral Data, *J. Indian Soc. Remote Sens.*, vol. 46, no. 8, pp. 1323–1331, 2018.

- [45] M. Gogebakan and H. Erol, Mixture Model Clustering Using Variable Data Segmentation and Model Selection: A Case Study of Genetic Algorithm, *Math. Lett.*, vol. 5, no. 2, p. 23, 2019.
- [46] M. B. Lopez, C. R. Del-Blanco, and N. Garcia, Detecting exercise-induced fatigue using thermal imaging and deep learning, in *Proceedings of the 7th International Conference on Image Processing Theory, Tools and Applications, IPTA 2017*, Nov. 2018, vol. 2018-Janua, pp. 1–6.
- [47] Blum Ronald, FarrierDaniel, and P. Leando, Protocol for Rapid Point-of-Contact Public Screening for SARS using Clinical Digital Infrared Thermal Imaging, *Am. Coll. Clin. Thermol.*, pp. 10–22, 2003.
- [48] R. Vardasca, C. Magalhaes, A. Seixas, R. Carvalho, and J. Mendes, Diabetic foot monitoring using dynamic thermography and AI classifiers, in *Proceedings of QIRT Asia 2019*, 2019, pp. 0–4.
- [49] C. Magalhaes, R. Vardasca, M. Rebelo, R. Valenca-Filipe, M. Ribeiro, and J. Mendes, Distinguishing melanocytic nevi from melanomas using static and dynamic infrared thermal imaging, *J. Eur. Acad. Dermatology Venereol.*, vol. 33, no. 9, pp. 1700–1705, 2019.
- [50] A. Nagori, L. S. Dhingra, A. Bhatnagar, R. Lodha, and T. Sethi, Predicting Hemodynamic Shock from Thermal Images using Machine Learning, *Sci. Rep.*, vol. 9, no. 1, pp. 1–9, 2019.
- [51] J. T and A. M, Model-based computer-aided method for diagnosis of cardiovascular disease using IR thermogram., *Biomed. Res.*, vol. 30, no. 1, pp. 95–101, 2019.
- [52] J. Thiruvengadam and A. Mariamichael, A preliminary study for the assessment of hypertension using static and dynamic IR thermograms, *Biomed. Tech.*, vol. 63, no. 2, pp. 197–206, 2018.
- [53] Y. Ding, The back thermal symmetry identification by pRAM neural networks, in *4th International Conference on Artificial Neural Networks*, 1995, vol. 1995, no. 409, pp. 437–441.
- [54] G. M. K. Ntonfo, M. Frize, and E. Bariciak, Detection of Necrotizing Enterocolitis in newborns using abdominal thermal signature analysis, in *2015 IEEE International Symposium on Medical Measurements and Applications (MeMeA) Proceedings*, May 2015, pp. 36–39.
- [55] P. Mahajan and S. Madhe, Hypo and hyperthyroid disorder detection from thermal

- images using Bayesian classifier, *Proc. - 2014 IEEE Int. Conf. Adv. Commun. Comput. Technol. ICACACT 2014*, pp. 1–4, 2015.
- [56] A. Nowakowski and M. Kaczmarek, Active dynamic thermography - problems of implementation in medical diagnostics, *Quant. Infrared Thermogr. J.*, vol. 8, no. 1, pp. 89–106, 2011.
- [57] B. R. Nhan and T. Chau, Classifying affective states using thermal infrared imaging of the human face, *IEEE Trans. Biomed. Eng.*, vol. 57, no. 4, pp. 979–987, 2010.
- [58] S. R. Samuel, C. G. Shashi Kumar, and G. A. Maiya, Infrared thermal imaging as an outcome measure in low back pain, *Res. J. Pharm. Biol. Chem. Sci.*, vol. 7, no. 1, pp. 1806–1810, 2016.
- [59] T. P. H, Assessment of effect of yoga therapy on backache using infrared thermal imaging system, Mangalore University, 2012.
- [60] D. G. von Schweinitz, Thermographic Diagnostics in Equine Back Pain, *Vet. Clin. North Am. Equine Pract.*, vol. 15, no. 1, pp. 161–177, Apr. 1999.
- [61] C. D. Mansfield, E. M. Attas, and R. M. Gall, Evaluation of static thermal and near-infrared hyperspectral imaging for the diagnosis of acute maxillary rhinosinusitis, *J. Otolaryngol.*, vol. 34, no. 2, pp. 99–108, 2005.
- [62] R. Kalaiarasi *et al.*, Role of Thermography in the Diagnosis of Chronic Sinusitis, *Cureus*, Mar. 2018.
- [63] S. Bagavathiappan *et al.*, Investigation of peripheral vascular disorders using thermal imaging, *Br. J. Diabetes Vasc. Dis.*, vol. 8, no. 2, pp. 102–104, Mar. 2008.
- [64] B. Meneses-Claudio, W. Alvarado-Diaz, and A. Roman-Gonzalez, Detection of suspicions of Varicose veins in the legs using thermal imaging, *Int. J. Adv. Comput. Sci. Appl.*, vol. 10, no. 5, pp. 431–435, 2019.
- [65] U. R. Gogoi, G. Majumdar, M. K. Bhowmik, and A. K. Ghosh, Evaluating the efficiency of infrared breast thermography for early breast cancer risk prediction in asymptomatic population, *Infrared Phys. Technol.*, vol. 99, no. September 2018, pp. 201–211, 2019.
- [66] P. Samant and R. Agarwal, Machine learning techniques for medical diagnosis of diabetes using iris images, *Comput. Methods Programs Biomed.*, vol. 157, pp. 121–128, 2018.
- [67] M. A. Martínez-Jiménez, J. L. Ramirez-GarciaLuna, E. S. Kolosovas-Machuca, J. Drager, and F. J. Gonzalez, Development and validation of an algorithm to predict

- the treatment modality of burn wounds using thermographic scans: Prospective cohort study, *PLoS One*, vol. 13, no. 11, pp. 1–16, 2018.
- [68] R. Vardasca, C. Magalhaes, and J. Mendes, Biomedical Applications of Infrared Thermal Imaging: Current State of Machine Learning Classification, *Proceedings*, vol. 27, no. 1, p. 46, 2019.
- [69] Y. Cho, S. J. Julier, and N. Bianchi-Berthouze, Instant stress: Detection of perceived mental stress through smartphone photoplethysmography and thermal imaging, *JMIR Ment. Heal.*, vol. 6, no. 4, p. e10140, 2019.
- [70] S. Wang, B. Pan, H. Chen, and Q. Ji, Thermal augmented expression recognition, *IEEE Trans. Cybern.*, vol. 48, no. 7, pp. 2203–2214, 2018.
- [71] Infrared. <https://en.wikipedia.org/wiki/Infrared> (accessed Mar. 27, 2022).
- [72] N. C. Beese, Infrared radiation, in *Science*, vol. 95, no. 2477, Hoboken, NJ, USA: John Wiley & Sons, Inc., 1942, pp. 614–617.
- [73] File:Human-Infrared.jpg. <https://en.wikipedia.org/wiki/File:Human-Infrared.jpg>.
- [74] FLIR, IR Temperature Sensor With Gige (Manual Focus): FLIR A35, 2020. <https://bit.ly/2D9gldy> (accessed Mar. 27, 2022).
- [75] TELEDYNE FLIR, How Do Thermal Cameras Work, 2020. <https://www.flir.com/discover/rd-science/how-do-thermal-cameras-work/> (accessed Mar. 27, 2022).
- [76] F. Asia, Can Thermal Imaging See Through Walls? And Other Common Questions, 2019. <https://www.flir.asia/discover/cores-components/can-thermal-imaging-see-through-walls/> (accessed Mar. 27, 2022).
- [77] F. Wikipedia, Thermographic camera, 2014. https://en.wikipedia.org/wiki/Thermographic_camera (accessed Mar. 27, 2022).
- [78] N. Otsu, Threshold Selection Method From Gray-Level Histograms., *IEEE Trans Syst Man Cybern*, vol. SMC-9, no. 1, pp. 62–66, 1979.
- [79] R. C. Gonzalez and R. E. Woods, *Digital Image Processing (3rd Edition)*. Prentice-Hall, Inc., 2006.
- [80] Histogram equalization, 2022. https://en.wikipedia.org/wiki/Histogram_equalization (accessed Mar. 27, 2022).
- [81] A. Géron, *Hands-on machine learning with Scikit-Learn, Keras and TensorFlow: concepts, tools, and techniques to build intelligent systems*, 2nd ed. O’Reilly Media, Inc., 2019.
- [82] Y. LeCun, Y. Bengio, and G. Hinton, Deep learning, *Nature*, vol. 521, no. 7553,

- pp. 436–444, May 2015.
- [83] W. McCulloch and W. Pitts, A Logical Calculus of the Ideas Immanent in Nervous Activity (1943), in *Ideas That Created the Future*, The MIT Press, 2021, pp. 79–88.
- [84] Y. Lecun, L. Bottou, Y. Bengio, and P. Haffner, Gradient-based learning applied to document recognition, *Proc. IEEE*, vol. 86, no. 11, pp. 2278–2324, 1998.
- [85] K. Fukushima, Neocognitron: A self-organizing neural network model for a mechanism of pattern recognition unaffected by shift in position, *Biol. Cybern.*, vol. 36, no. 4, pp. 193–202, Apr. 1980.
- [86] M. Hall, E. Frank, G. Holmes, B. Pfahringer, P. Reutemann, and I. H. Witten, The WEKA data mining software, *ACM SIGKDD Explor. Newsl.*, vol. 11, no. 1, pp. 10–18, Nov. 2009.
- [87] Matlab, MATLAB. 2021.
- [88] Medcore, IRIS-XP. <https://medi-core.com/en/thermography/iris-xp.html>.
- [89] A. Jalal, A. Nadeem, and S. Bobasu, Human Body Parts Estimation and Detection for Physical Sports Movements, in *2019 2nd International Conference on Communication, Computing and Digital systems (C-CODE)*, Mar. 2019, pp. 104–109.
- [90] T. Kohlschütter and P. Herout, Automatic Human Body Parts Detection in a 2D Anthropometric System, 2012, pp. 536–544.
- [91] A. Brandão, L. A. F. Fernandes, and E. Clua, M5AIE - A Method for Body Part Detection and Tracking using RGB-D Images, in *Proceedings of the 9th International Conference on Computer Vision Theory and Applications*, 2014, pp. 367–377.
- [92] H.-W. Chen and M. McGurr, Improved color and intensity patch segmentation for human full-body and body-parts detection and tracking, in *2014 11th IEEE International Conference on Advanced Video and Signal Based Surveillance (AVSS)*, Aug. 2014, pp. 361–368.
- [93] A. Nadeem, A. Jalal, and K. Kim, Automatic human posture estimation for sport activity recognition with robust body parts detection and entropy markov model, *Multimed. Tools Appl.*, vol. 80, no. 14, pp. 21465–21498, Jun. 2021.
- [94] L. Sigal, A. O. Balan, and M. J. Black, HumanEva: Synchronized Video and Motion Capture Dataset and Baseline Algorithm for Evaluation of Articulated Human Motion, *Int. J. Comput. Vis.*, vol. 87, no. 1–2, pp. 4–27, Mar. 2010.

- [95] C. Schuldt, I. Laptev, and B. Caputo, Recognizing human actions: a local SVM approach, in *Proceedings of the 17th International Conference on Pattern Recognition, 2004. ICPR 2004.*, 2004, pp. 32-36 Vol.3.
- [96] D. Ramanan, D. A. Forsyth, and A. Zisserman, Tracking People by Learning Their Appearance, *IEEE Trans. Pattern Anal. Mach. Intell.*, vol. 29, no. 1, pp. 65–81, Jan. 2007.
- [97] A. Özdil and B. Yılmaz, Automatic body part and pose detection in medical infrared thermal images, *Quant. Infrared Thermogr. J.*, pp. 1–16, Jun. 2021.
- [98] R. C. Gonzalez and R. E. Woods, *Digital Image Processing(Second Edition)*, 2nd ed. Prentice-Hall, 2002.
- [99] J. Redmon and A. Farhadi, YOLO9000: Better, faster, stronger, *Proc. - 30th IEEE Conf. Comput. Vis. Pattern Recognition, CVPR 2017*, vol. 2017-Janua, pp. 6517–6525, 2017.
- [100] S. Karamizadeh, S. M. Abdullah, A. A. Manaf, M. Zamani, and A. Hooman, An Overview of Principal Component Analysis, *J. Signal Inf. Process.*, vol. 04, no. 03, pp. 173–175, 2013.
- [101] C. R. García-Alonso, L. M. Pérez-Naranjo, and J. C. Fernández-Caballero, Multiobjective evolutionary algorithms to identify highly autocorrelated areas: The case of spatial distribution in financially compromised farms, *Ann. Oper. Res.*, vol. 219, no. 1, pp. 187–202, 2014.
- [102] U. of Waikato, Class hierarchy (weka-dev 3.9.5 API). <https://weka.sourceforge.io/doc.dev/overview-tree.html> (accessed Jan. 04, 2021).
- [103] N. Ketkar and J. Moolayil, *Deep Learning with Python*, vol. 361. Manning New York, 2021.
- [104] J. Yang, W. Wang, G. Lin, Q. Li, Y. Sun, and Y. Sun, Infrared Thermal Imaging-Based Crack Detection Using Deep Learning, *IEEE Access*, vol. 7, pp. 182060–182077, 2019.
- [105] M. I. Razzak, S. Naz, and A. Zaib, Deep Learning for Medical Image Processing: Overview, Challenges and Future, *Classif. BioApps*, pp. 323–350, Apr. 2018.
- [106] V. A. Sevastianos and S. J. Hadziyannis, Nonalcoholic fatty liver disease: From clinical recognition to treatment, *Expert Rev. Gastroenterol. Hepatol.*, vol. 2, no. 1, pp. 59–79, 2008.
- [107] Z. Younossi *et al.*, Global burden of NAFLD and NASH: Trends, predictions, risk factors and prevention, *Nat. Rev. Gastroenterol. Hepatol.*, vol. 15, no. 1, pp. 11–

20, 2018.

- [108] R. Y. Brzezinski *et al.*, Automated thermal imaging for the detection of fatty liver disease, *Sci. Rep.*, vol. 10, no. 1, pp. 1–24, 2020.
- [109] N. F. Schwenzer, F. Springer, C. Schraml, N. Stefan, J. Machann, and F. Schick, Non-invasive assessment and quantification of liver steatosis by ultrasound, computed tomography and magnetic resonance, *J. Hepatol.*, vol. 51, no. 3, pp. 433–445, 2009.
- [110] W. H. Kruskal and W. A. Wallis, Use of Ranks in One-Criterion Variance Analysis, *J. Am. Stat. Assoc.*, vol. 47, no. 260, pp. 583–621, Dec. 1952.
- [111] U. R. Gogoi, M. K. Bhowmik, A. K. Ghosh, D. Bhattacharjee, and G. Majumdar, Discriminative feature selection for breast abnormality detection and accurate classification of thermograms, in *2017 International Conference on Innovations in Electronics, Signal Processing and Communication (IESC)*, Apr. 2017, pp. 39–44.
- [112] H. Ghayoumi Zadeh *et al.*, Segmenting breast cancerous regions in thermal images using fuzzy active contours, *EXCLI J.*, vol. 15, pp. 532–550, 2016.
- [113] U. R. Gogoi, G. Majumdar, M. K. Bhowmik, A. K. Ghosh, and D. Bhattacharjee, Breast abnormality detection through statistical feature analysis using infrared thermograms, in *2015 International Symposium on Advanced Computing and Communication (ISACC)*, Sep. 2015, pp. 258–265.
- [114] A. Morales-Cervantes, E. S. Kolosovas-Machuca, E. Guevara, F. J. Gonzalez, and J. J. Flores, Evaluation of Breast Cancer by Infrared Thermography, *Res. Comput. Sci.*, vol. 149, no. 5, pp. 137–149, 2020.
- [115] E. Ring, The historical development of thermometry and thermal imaging in medicine, *J. Med. Eng. Technol.*, vol. 30, no. 4, pp. 192–198, 2006.
- [116] M. Anbar, Clinical thermal imaging today, *IEEE Eng. Med. Biol. Mag.*, vol. 17, no. 4, pp. 25–33, 1998.
- [117] H. Hooshmand, M. Hashmi, and E. M. Phillips, Infrared Thermal Imaging As A Tool In Pain Management - An 11 Year Study, Part II: Clinical Applications, *Thermol. Int.*, vol. 11, no. 3, pp. 1–13, 2001.
- [118] J. Thiruvengadam and A. Mariamichael, Model-based computer-aided method for diagnosis of cardiovascular disease using IR thermogram., *Biomed. Res.*, vol. 30, 2019.
- [119] S. Pérez-Buitrago, S. Tobón-Pareja, Y. Gómez-Gaviria, A. Guerrero-Peña, and G. Díaz-Londoño, Methodology to evaluate temperature changes in multiple sclerosis

- patients by calculating texture features from infrared thermography images, *Quant. Infrared Thermogr. J.*, vol. 00, no. 00, pp. 1–11, 2020.
- [120] S. K. Shahi, S. N. Freedman, R. A. Dahl, N. J. Karandikar, and A. K. Mangalam, Scoring disease in an animal model of multiple sclerosis using a novel infrared-based automated activity-monitoring system, *Sci. Rep.*, vol. 9, no. 1, pp. 1–12, 2019.
- [121] S. L. Davis, T. E. Wilson, A. T. White, and E. M. Frohman, Thermoregulation in multiple sclerosis, *J. Appl. Physiol.*, vol. 109, no. 5, pp. 1531–1537, 2010.
- [122] R. M. Papaléo, M. J. Teixeira, and M. L. Brioschi, Infrared thermography to evaluate pain in a multiple sclerosis patient. Case report, *Rev. Dor*, vol. 17, no. 3, pp. 232–235, 2016.
- [123] J. F. Sumowski and V. M. Leavitt, Body temperature is elevated and linked to fatigue in relapsing-remitting multiple sclerosis, even without heat exposure, *Arch. Phys. Med. Rehabil.*, vol. 95, no. 7, pp. 1298–1302, 2014.
- [124] V. M. Leavitt *et al.*, Elevated body temperature is linked to fatigue in an Italian sample of relapsing–remitting multiple sclerosis patients, *J. Neurol.*, vol. 262, no. 11, pp. 2440–2442, 2015.
- [125] B. Drukarch *et al.*, Thinking about the nerve impulse: A critical analysis of the electricity-centered conception of nerve excitability, *Prog. Neurobiol.*, vol. 169, no. June, pp. 172–185, 2018.
- [126] M. Kass, A. Witkin, and D. Terzopoulos, Snakes: Active contour models, *Int. J. Comput. Vis.*, vol. 1, no. 4, pp. 321–331, 1988.
- [127] E. Gallasch, M. Christova, A. Kunz, D. Rafolt, and S. Golaszewski, Modulation of sensorimotor cortex by repetitive peripheral magnetic stimulation, *Front. Hum. Neurosci.*, vol. 9, no. JULY, p. 407, Jul. 2015.
- [128] J.-P. Lefaucheur, Transcranial magnetic stimulation, in *Handbook of Clinical Neurology*, K. H. Levin and P. Chauvel, Eds. Elsevier, 2019, pp. 559–580.
- [129] V. Napadow, N. Makris, J. Liu, N. W. Kettner, K. K. Kwong, and K. K. S. Hui, Effects of electroacupuncture versus manual acupuncture on the human brain as measured by fMRI, *Hum. Brain Mapp.*, vol. 24, no. 3, pp. 193–205, Mar. 2005.
- [130] Dina Soliman, New Erra with Auto-Haemotherapy, *J. Phys. Sci. Appl.*, vol. 7, no. 2, pp. 31–35, Feb. 2017.
- [131] M. McCoyd, A. Salardini, and J. Biller, The Neurological Examination, *Oper. Neurosurg.*, vol. 17, no. Supplement_2, pp. S3–S16, Aug. 2019.

- [132] A. Jäkel and P. von Hauenschild, A systematic review to evaluate the clinical benefits of craniosacral therapy, *Complement. Ther. Med.*, vol. 20, no. 6, pp. 456–465, Dec. 2012.
- [133] R. Milo and E. Kahana, Multiple sclerosis: Geoepidemiology, genetics and the environment, *Autoimmun. Rev.*, vol. 9, no. 5, pp. A387–A394, 2010.
- [134] R. Navarro-Martínez and O. Cauli, Therapeutic plasmapheresis with albumin replacement in alzheimer’s disease and chronic progressive multiple sclerosis: A review, *Pharmaceuticals*, vol. 13, no. 2, p. 28, Feb. 2020.
- [135] A. Galletto Pregliasco *et al.*, Improved detection of new MS lesions during follow-up using an automated MR coregistration-fusion method, *Am. J. Neuroradiol.*, vol. 39, no. 7, pp. 1226–1232, Jul. 2018.
- [136] R. LAWSON, Implications of surface temperatures in the diagnosis of breast cancer, *Can. Med. Assoc. J.*, vol. 75, no. 4, pp. 309–11, Aug. 1956.
- [137] S. Dey, R. Roychoudhury, S. Malakar, and R. Sarkar, Screening of breast cancer from thermogram images by edge detection aided deep transfer learning model, *Multimed. Tools Appl.*, vol. 81, no. 7, pp. 9331–9349, Mar. 2022.
- [138] R. Karthiga and K. Narasimhan, Medical imaging technique using curvelet transform and machine learning for the automated diagnosis of breast cancer from thermal image, *Pattern Anal. Appl.*, vol. 24, no. 3, pp. 981–991, Aug. 2021.
- [139] R. Sánchez-Cauce, J. Pérez-Martín, and M. Luque, Multi-input convolutional neural network for breast cancer detection using thermal images and clinical data, *Comput. Methods Programs Biomed.*, vol. 204, p. 106045, Jun. 2021.
- [140] A. Arul Edwin Raj, M. Sundaram, and T. Jaya, Advanced Framework for Effective Denoising the Enhanced Thermal Breast Image, *IETE J. Res.*, pp. 1–14, Mar. 2021.
- [141] D. Plaza *et al.*, Correlation between isotherms and isodoses in breast cancer radiotherapy—first study, *Int. J. Environ. Res. Public Health*, vol. 18, no. 2, pp. 1–10, 2021.
- [142] A. Lubkowska and M. Chudecka, Thermal characteristics of breast surface temperature in healthy women, *Int. J. Environ. Res. Public Health*, vol. 18, no. 3, pp. 1–11, 2021.
- [143] M. Moderhak, S. Kołacz, J. Jankau, and T. Juchniewicz, Active dynamic thermography method for TRAM flap blood perfusion mapping in breast reconstruction, *Quant. Infrared Thermogr. J.*, vol. 14, no. 2, pp. 234–249, Jul. 2017.

- [144] O. T. Da Silveira F, R. C. Serrano, A. Conci, R. H. C. De Melo, and R. C. F. Lima, On using lacunarity for diagnosis of breast diseases considering thermal images, *2009 16th Int. Conf. Syst. Signals Image Process. IWSSIP 2009*, pp. 1–4, 2009.
- [145] D. Singh and A. K. Singh, Role of image thermography in early breast cancer detection- Past, present and future, *Comput. Methods Programs Biomed.*, vol. 183, 2020.
- [146] U. R. Gogoi, M. K. Bhowmik, D. Bhattacharjee, and A. K. Ghosh, Singular value based characterization and analysis of thermal patches for early breast abnormality detection, *Australas. Phys. Eng. Sci. Med.*, vol. 41, no. 4, pp. 861–879, 2018.
- [147] Z. Zore, I. Boras, M. Stanec, T. Orešić, and I. F. Zore, Influence of hormonal status on thermography findings in breast cancer, *Acta Clin. Croat.*, vol. 52, no. 1, pp. 35–42, 2013.
- [148] F. Gutierrez-Delgado and J. G. Vázquez-Luna, Feasibility of New-generation Infrared Imaging Screening for Breast Cancer in Rural Communities, *Oncol. Hematol. Rev.*, vol. 06, p. 60, 2010.
- [149] V. Madhavi and C. B. Thomas, Multi-view breast thermogram analysis by fusing texture features, *Quant. Infrared Thermogr. J.*, vol. 16, no. 1, pp. 111–128, 2019.
- [150] V. Madhavi and T. Christy Bobby, Thermal imaging based breast cancer analysis using BEMD and uniform RLBP, *Proc. 3rd Int. Conf. Biosignals, Images Instrumentation, ICBSII 2017*, no. March, pp. 16–18, 2017.
- [151] E. Saniei, S. Setayeshi, M. E. Akbari, and M. Navid, A vascular network matching in dynamic thermography for breast cancer detection, *Quant. Infrared Thermogr. J.*, vol. 12, no. 1, pp. 24–36, 2015.
- [152] A. Tiwari, A. Gupta, H. Kataria, and G. Singal, Analysis of Machine Learning and Deep Learning Classifiers to Detect and Classify Breast Cancer, vol. 58, 2021, pp. 471–480.
- [153] N. Golestani, M. EtehadTavakol, and E. Y. K. Ng, Level set method for segmentation of infrared breast thermograms, *EXCLI J.*, vol. 13, pp. 241–251, 2014.
- [154] R. Hatwar and C. Herman, Inverse method for quantitative characterisation of breast tumours from surface temperature data, *Int. J. Hyperth.*, vol. 33, no. 7, pp. 1–17, Apr. 2017.
- [155] S. Pramanik, D. Banik, D. Bhattacharjee, M. Nasipuri, M. K. Bhowmik, and G. Majumdar, Suspicious-Region Segmentation From Breast Thermogram Using

- DLPE-Based Level Set Method, *IEEE Trans. Med. Imaging*, vol. 38, no. 2, pp. 572–584, Feb. 2019.
- [156] P. Gomathi and V. Jamuna, Feature Extraction Of Thermal Image For Breast Cancer Analysis, *Int. J. Pure Appl. Math.*, vol. 118, no. 20B, pp. 707–712, 2018.
- [157] F. J. González, Non-invasive estimation of the metabolic heat production of breast tumors using digital infrared imaging, *Quant. Infrared Thermogr. J.*, vol. 8, no. 2, pp. 139–148, Dec. 2011.
- [158] M. A. S. Al Husaini, M. H. Habaebi, T. S. Gunawan, M. R. Islam, and S. A. Hameed, Automatic Breast Cancer Detection Using Inception V3 in Thermography, in *2021 8th International Conference on Computer and Communication Engineering (ICCCCE)*, Jun. 2021, pp. 255–258.
- [159] M. R. K. Mookiah, U. R. Acharya, and E. Y. K. Ng, Data mining technique for breast cancer detection in thermograms using hybrid feature extraction strategy, *Quant. Infrared Thermogr. J.*, vol. 9, no. 2, pp. 151–165, Dec. 2012.
- [160] F. Sadoughi, Z. Kazemy, F. Hamedan, L. Owji, M. Rahmanikatigari, and T. Talebi Azadboni, Artificial intelligence methods for the diagnosis of breast cancer by image processing: a review, *Breast Cancer Targets Ther.*, vol. Volume 10, pp. 219–230, Nov. 2018.
- [161] G. Schaefer, S. Ying Zhu, and B. Jones, Retrieving Thermal Medical Images, *Comput. Vis. Graph.*, pp. 906–911, 2006.
- [162] K. Das, M. K. Bhowmik, O. Chowdhury, D. Bhattacharjee, and B. K. De, Accurate segmentation of inflammatory and abnormal regions using medical thermal imagery, *Australas. Phys. Eng. Sci. Med.*, vol. 42, no. 2, pp. 647–657, 2019.
- [163] S. Bardhan, M. K. Bhowmik, T. Debnath, and D. Bhattacharjee, RASIT: Region shrinking based Accurate Segmentation of Inflammatory areas from Thermograms, *Biocybern. Biomed. Eng.*, vol. 38, no. 4, pp. 903–917, 2018.
- [164] H. K. V. da Silva, M. C. E. Oliveira, E. Silva-Filho, A. G. Magalhães, G. N. Correia, and M. T. A. B. C. Micussi, Evaluation of the female pelvic floor with infrared thermography: a cross sectional study, *Brazilian J. Phys. Ther.*, vol. 26, no. 1, p. 100390, Jan. 2022.
- [165] R. Rashmi, U. Snehalatha, P. T. Krishnan, and V. Dhanraj, Fat-based studies for computer-assisted screening of child obesity using thermal imaging based on deep learning techniques: a comparison with quantum machine learning approach, *Soft*

- Comput.*, pp. 1–22, Jan. 2022.
- [166] E. Koroteeva and A. Shagiyanova, Infrared-based visualization of exhalation flows while wearing protective face masks, *Phys. Fluids*, vol. 34, no. 1, p. 011705, Jan. 2022.
- [167] S. M. Ahn *et al.*, The Value of Thermal Imaging for Knee Arthritis: A Single-Center Observational Study, *Yonsei Med. J.*, vol. 63, no. 2, p. 141, 2022.
- [168] W. A. D. Strasse *et al.*, Thermography applied in the diagnostic assessment of bone fractures, *Res. Biomed. Eng.*, pp. 141–147, Feb. 2022.
- [169] Y. Mibae and H. Noguchi, Visualization System of 3D Foot Plantar Model with Temperature Information Using RGB-D and Thermography Cameras for Prevention of Foot Ulcer in Diabetic Patients, in *2022 IEEE/SICE International Symposium on System Integration (SII)*, Jan. 2022, pp. 537–542.
- [170] M. Domino *et al.*, Advances in Thermal Image Analysis for the Detection of Pregnancy in Horses Using Infrared Thermography, *Sensors*, vol. 22, no. 1, p. 191, Dec. 2021.
- [171] F. Scholleman, J. Kunczik, H. Dohmeier, C. B. Pereira, A. Follmann, and M. Czaplik, Infection Probability Index: Implementation of an Automated Chronic Wound Infection Marker, *J. Clin. Med.*, vol. 11, no. 1, p. 169, Dec. 2021.
- [172] S. Ervural and M. Ceylan, Thermogram classification using deep siamese network for neonatal disease detection with limited data, *Quant. Infrared Thermogr. J.*, vol. 00, no. 00, pp. 1–19, Dec. 2021.
- [173] H. Leo, K. Saddami, R. Roslidar, M. Oktiana, F. Arnia, and K. Munadi, A Study of Parameters Required for a Thermogram Dataset in Obesity Detection: A Systematic Review, in *2021 International Conference on Computer System, Information Technology, and Electrical Engineering (COSITE)*, Oct. 2021, pp. 112–117.
- [174] I. M. Baker, Infrared antenna-like structures in mammalian fur, *R. Soc. Open Sci.*, vol. 8, no. 12, p. 210740, Dec. 2021.
- [175] R. R. Fletcher *et al.*, The Use of Mobile Thermal Imaging and Deep Learning for Prediction of Surgical Site Infection, in *2021 43rd Annual International Conference of the IEEE Engineering in Medicine & Biology Society (EMBC)*, Nov. 2021, pp. 5059–5062.
- [176] H. Yuan, C. Liu, H. Wang, L. Wang, and F. Sun, Optimization and comparison of models for core temperature prediction of mother rabbits using infrared

- thermography, *Infrared Phys. Technol.*, vol. 120, p. 103987, Jan. 2022.
- [177] B. Kaźmierska, K. A. Sobiech, E. Demczuk - Włodarczyk, and A. Chwałczyńska, Thermovision assessment of temperature changes in selected body areas after short-wave diathermy treatment, *J. Therm. Anal. Calorim.*, Dec. 2021.
- [178] E. Freeman, J. F. Johnson, J. C. Godbold, and R. J. Riegel, Comparison of Infrared Thermal Imaging with Two Canine Pain Assessment Tools in Dogs Undergoing Treatment for Chronic Back Pain, *Preprints*, no. December, 2021.
- [179] R. F. Leite *et al.*, Principles and cautions in the infrared thermography application in sheep, *Multidiscip. Rev.*, vol. 5, no. 1, pp. 1–5, 2022.
- [180] I. A. Burkov, L. M. Kolishkin, A. V. Pushkarev, A. V. Shakurov, D. I. Tsiganov, and A. A. Zherdev, Experimental and computational thermal analysis of partial-body cryotherapy, *Int. J. Heat Mass Transf.*, vol. 183, no. xxxx, p. 122194, Feb. 2022.
- [181] S. Kajiwara, Driver-Condition Detection Using a Thermal Imaging Camera and Neural Networks, *Int. J. Automot. Technol.*, vol. 22, no. 6, pp. 1505–1515, Dec. 2021.
- [182] W. auf der Strasse, D. P. Campos, C. J. A. Mendonça, J. F. Soni, J. Mendes, and P. Nohama, Evaluation of Tibia Bone Healing by Infrared Thermography: A Case Study, *J. Multidiscip. Healthc.*, vol. Volume 14, pp. 3161–3175, Nov. 2021.
- [183] R. L. O. Jr., J. A. Olalia, and M. G. F. Carse, Evaluating Infrared Thermal Image's Color Palettes in Hot Tropical Area, *J. Comput. Commun.*, vol. 09, no. 11, pp. 37–49, 2021.
- [184] W. Der Strasse, J. F. Soni, and P. Nohama, Detecting Bone Lesions in The Emergency Room With Medical Infrared Thermography, *Biomed. Eng. Online*, 2021.
- [185] C. R. Siah, S. T. Lau, S. S. Tng, and C. H. M. Chua, Using infrared imaging and deep learning in fit-checking of respiratory protective devices among healthcare professionals, *J. Nurs. Scholarsh.*, Nov. 2021.
- [186] S. Derruau, F. Bogard, G. Exartier-Menard, C. Mauprivez, and G. Polidori, Medical Infrared Thermography in Odontogenic Facial Cellulitis as a Clinical Decision Support Tool. A Technical Note, *Diagnostics*, vol. 11, no. 11, p. 2045, Nov. 2021.
- [187] Y. Iwashita, K. Nagumo, K. Oiwa, and A. Nozawa, Evaluation of Model Performance for Estimating Resting Blood Pressure Using Independent

- Components of Facial Thermal Images, in *2021 IEEE 19th International Symposium on Intelligent Systems and Informatics (SISY)*, Sep. 2021, pp. 135–140.
- [188] T. Singh, K. Kumar, and S. S. Bedi, A review on artificial intelligence techniques for disease recognition in plants, *IOP Conf. Ser. Mater. Sci. Eng.*, vol. 1022, no. 1, p. 012032, Jan. 2021.
- [189] A. Baic *et al.*, The use of thermal imaging in the evaluation of temperature effects of radiotherapy in patients after mastectomy—first study, *Sensors*, vol. 21, no. 21, p. 7068, 2021.
- [190] M. A. Jaddoa, L. Gonzalez, H. Cuthbertson, and A. Al-Jumaily, Multiview Eye Localisation to Measure Cattle Body Temperature Based on Automated Thermal Image Processing and Computer Vision, *Infrared Phys. Technol.*, vol. 119, p. 103932, Dec. 2021.
- [191] Q. Chen, Y. Huang, J. Luo, H. Lu, Z. Ji, and X. Zhu, Palpation Localization of Radial Artery Based on 3-Dimensional Convolutional Neural Networks, *EURASIP J. Image Video Process.*, pp. 0–17, 2021.
- [192] L. S. Wilk *et al.*, Individualised and non-contact post-mortem interval determination of human bodies using visible and thermal 3D imaging, *Nat. Commun.*, vol. 12, no. 1, pp. 1–10, 2021.
- [193] S. Vaughn, R. Ruthazer, A. Rosenblatt, R. L. Jenkins, A. P. Sorcini, and T. Schnelldorfer, Long-Wave Infrared Imaging for Intraoperative Cancer Detection—What is the True Temperature of a Cancer?, *Surg. Innov.*, p. 155335062110460, Oct. 2021.
- [194] Y. Iwashita, K. Nagumo, K. Oiwa, and A. Nozawa, Estimation of resting blood pressure using facial thermal images by separating acute stress variations, *Artif. Life Robot.*, vol. 26, no. 4, pp. 473–480, 2021.
- [195] E. Gutierrez, B. Castañeda, S. Treuillet, and I. Hernandez, Multimodal and Multiview Wound Monitoring with Mobile Devices, *Photonics*, vol. 8, no. 10, p. 424, Oct. 2021.
- [196] B. Kalivaraprasad, M. V. D. Prasad, K. Rajesh Babu, S. Shameem, S. Mohan, and V. Vani, Comparative Analysis of Watermarking Methods on CFRP Sample Thermal Images, in *Lecture Notes in Networks and Systems*, 2021, pp. 455–462.
- [197] S. Neema, D. M. Tripathy, S. Mukherjee, A. Sinha, S. Vendhan, and B. Vasudevan, Infrared thermography in the diagnosis of palmar hyperhidrosis: A diagnostic study, *Med. J. Armed Forces India*, Sep. 2021.

- [198] Q. Zhang *et al.*, Screening Evaporative Dry Eyes Severity Using an Infrared Image, *J. Ophthalmol.*, vol. 2021, pp. 1–8, Aug. 2021.
- [199] S. Byun *et al.*, The Use of Thermal Imaging and Deep Learning for Pulmonary Diagnostics and Infection Detection, in *2021 IEEE 17th International Conference on Wearable and Implantable Body Sensor Networks (BSN)*, Jul. 2021, pp. 1–4.
- [200] X. Liu, J. Feng, R. Zhang, J. Luan, and Z. Wu, Quantitative assessment of Bell’s palsy-related facial thermal asymmetry using infrared thermography: A preliminary study, *J. Therm. Biol.*, vol. 100, no. April, p. 103070, 2021.
- [201] A. G. Becerra *et al.*, Infrared thermal imaging monitoring on hands when performing repetitive tasks: An experimental study, *PLoS One*, vol. 16, no. 5, p. e0250733, May 2021.
- [202] S. V Francis, J. Sivakamasundari, and S. Jaipurkar, A Preliminary Investigation on Ocular Thermal Image Patterns Using Clinical Case Studies, *Ann. Rom. Soc. Cell Biol.*, vol. 25, no. 6, pp. 13710–13718, 2021.
- [203] M. Monshipouri *et al.*, Thermal imaging potential and limitations to predict healing of venous leg ulcers, *Sci. Rep.*, vol. 11, no. 1, pp. 1–11, 2021.
- [204] C. Magalhaes, J. M. R. S. Tavares, J. Mendes, and R. Vardasca, Comparison of machine learning strategies for infrared thermography of skin cancer, *Biomed. Signal Process. Control*, vol. 69, no. April, p. 102872, Aug. 2021.
- [205] S. Dervis, K. L. Dobson, T. S. Nagpal, C. Geurts, F. Haman, and K. B. Adamo, Heat loss responses at rest and during exercise in pregnancy: A scoping review., *J. Therm. Biol.*, vol. 99, no. December 2020, p. 103011, 2021.
- [206] M. A. Pramod, Preliminary Screening System for Detecting the Presence and Absence of Paranasal Sinusitis using Thermal Imaging Technique, *J. Xi’an Univ. Archit. Technol.*, vol. XIII, no. 5, pp. 394–403, 2010.
- [207] S. J. Ujalambe and S. P. Madhe, Glaucoma Detection using the Thermal Image Processing, in *2021 5th International Conference on Intelligent Computing and Control Systems (ICICCS)*, May 2021, pp. 761–765.
- [208] P. R. Mahajan, N. Parihar, I. Kale, M. Thakur, and S. Raut, Infrared Thermography for Orthopaedic Disorders by Image Processing, *Int. J. Res. Eng. Sci.*, vol. 9, no. 7, pp. 66–69, 2021.
- [209] M. López-Aguirre *et al.*, Lesion 3D modeling in transcranial MR-guided focused ultrasound thalamotomy, *Magn. Reson. Imaging*, vol. 80, pp. 71–80, Jul. 2021.
- [210] T. Sawhney, S. Singh, and P. K. Lehana, Analysis And Evaluation Of Audio

- Induced Acoustic Fatigue Using Infrared Imaging, *Turkish J. Comput. Math. Educ.*, vol. 12, no. 9, pp. 1491–1498, 2021.
- [211] R. A. B. da Silva, B. Stosic, H. Pandorfi, G. L. P. de Almeida, M. V. da Silva, and P. H. D. Batista, Classification of Thermal Images of Bovine Mastitis by Computer Vision, *Int. J. Comput. Appl.*, vol. 174, no. 31, pp. 41–45, 2021.
- [212] M. Monshipouri *et al.*, Thermal imaging potential and limitations to predict healing of venous leg ulcers., *Sci. Rep.*, vol. 11, no. 1, p. 13239, Apr. 2021.
- [213] M. Machoy, L. Szyszka-Sommerfeld, M. Rahnama, R. Koprowski, S. Wilczyński, and K. Woźniak, Diagnosis of Temporomandibular Disorders Using Thermovision Imaging, *Pain Res. Manag.*, vol. 2020, pp. 1–8, Nov. 2020.
- [214] P. Sabitha, C. Bammigatti, S. Deepanjali, B. S. Suryanarayana, and T. Kadhiravan, Point-of-care infrared thermal imaging for differentiating venomous snakebites from non-venomous and dry bites, *PLoS Negl. Trop. Dis.*, vol. 15, no. 2, pp. 1–14, 2021.
- [215] Z. Ovadia-Blechman *et al.*, Assessment of blood distribution in response to post-surgical steal syndrome: A novel technique based on Thermo-Anatomical Segmentation, *J. Biomech.*, vol. 119, p. 110304, Apr. 2021.
- [216] Ilo and Arjaleena, *Infrared thermography in vascular disorders : screening and follow-up.* 2020.
- [217] F. W. Panella, A. Pirinu, and V. Dattoma, A Brief Review and Advances of Thermographic Image - Processing Methods for IRT Inspection: a Case of Study on GFRP Plate, *Exp. Tech.*, vol. 45, no. 4, pp. 429–443, 2021.
- [218] A. Casas-Barragán, F. Molina, R. M. Tapia-Haro, M. C. García-Ríos, M. Correa-Rodríguez, and M. E. Aguilar-Ferrándiz, Association of core body temperature and peripheral blood flow of the hands with pain intensity, pressure pain hypersensitivity, central sensitization, and fibromyalgia symptoms, *Ther. Adv. Chronic Dis.*, vol. 12, p. 204062232199725, Jan. 2021.
- [219] A. Saxena, E. Y. K. Ng, T. Canchi, J. L. Lim, and A. S. Beruvar, A method to produce high contrast vein visualization in active dynamic thermography (ADT), *Comput. Biol. Med.*, vol. 132, no. December 2020, p. 104309, 2021.
- [220] R. Rytivaara *et al.*, Thermographic findings related to facial pain – a survey of 40 subjects, *CRANIO®*, vol. 00, no. 00, pp. 1–8, Mar. 2021.
- [221] J. Diener *et al.*, Sensitivity and Specificity of Thermal Imaging When Used to Detect Superficial Venous Reflux as Compared to Duplex Ultrasound, *Vasc. Dis.*

- Manag.*, vol. 18, no. 3, pp. E45--E49, 2021.
- [222] R. Rashmi, S. Umapathy, and P. T. Krishnan, Thermal imaging method to evaluate childhood obesity based on machine learning techniques, *Int. J. Imaging Syst. Technol.*, vol. 31, no. 3, pp. 1752–1768, 2021.
- [223] T. V. Dave, P. Patodi, A. Richhariya, and V. P. Dave, Thermal Imaging of the Ocular Surface in Thyroid Eye Disease: A Comparison between Active, Inactive and Healthy Eyes, *Curr. Eye Res.*, vol. 46, no. 10, pp. 1482–1488, 2021.
- [224] S. González-Pérez *et al.*, Assessment of Registration Methods for Thermal Infrared and Visible Images for Diabetic Foot Monitoring, *Sensors*, vol. 21, no. 7, p. 2264, Mar. 2021.
- [225] K. Khaksari *et al.*, Review of the efficacy of infrared thermography for screening infectious diseases with applications to COVID-19, *J. Med. Imaging*, vol. 8, no. S1, pp. 1–15, 2021.
- [226] M. Awais *et al.*, Can pre-trained convolutional neural networks be directly used as a feature extractor for video-based neonatal sleep and wake classification?, *BMC Res. Notes*, vol. 13, no. 1, pp. 1–6, 2020.
- [227] B. Peddinti, A. Shaikh, B. K.R., and N. K. K.C., Framework for Real-Time Detection and Identification of possible patients of COVID-19 at public places, *Biomed. Signal Process. Control*, vol. 68, p. 102605, Jul. 2021.
- [228] G. S. Kumar, R. G. Roy, and S. Rajesh, A study on various thermographic methods for the detection of diseases, in *2021 Third International Conference on Intelligent Communication Technologies and Virtual Mobile Networks (ICICV)*, Feb. 2021, pp. 906–916.
- [229] P. Mohamed Shakeel, T. E. E. Tobely, H. Al-Feel, G. Manogaran, and S. Baskar, Neural Network Based Brain Tumor Detection Using Wireless Infrared Imaging Sensor, *IEEE Access*, vol. 7, pp. 5577–5588, 2019.
- [230] D. Fokam and C. Lehmann, Clinical assessment of arthritic knee pain by infrared thermography, *J. Basic Clin. Physiol. Pharmacol.*, vol. 30, no. 3, May 2019.
- [231] D. Koundal, Computer-Aided Diagnosis of Thyroid Nodule: A Review, *Int. J. Comput. Sci. Eng. Surv.*, vol. 3, no. 4, pp. 67–83, 2012.
- [232] N. Arteaga-Marrero, A. Hernández, E. Villa, S. González-Pérez, C. Luque, and J. Ruiz-Alzola, Segmentation approaches for diabetic foot disorders, *Sensors (Switzerland)*, vol. 21, no. 3, pp. 1–16, 2021.
- [233] H. Zbroja, M. Kowalski, and A. Lubkowska, The effect of dry carbon dioxide

- bathing on peripheral blood circulation measured by thermal imaging among patients with risk factors of pad, *Int. J. Environ. Res. Public Health*, vol. 18, no. 4, pp. 1–14, 2021.
- [234] U. S. Kumar and N. M. Sudharsan, Enhancement Techniques on Medical Thermal Image of Pregnant Women for Fetal Growth Monitoring, *Comput. Methods Biomech. Biomed. Eng. Imaging Vis.*, vol. 9, no. 5, pp. 523–534, Sep. 2021.
- [235] S. N. S. Al-Humairi and A. A. A. Kamal, Opportunities and challenges for the building monitoring systems in the age-pandemic of COVID-19: Review and prospects, *Innov. Infrastruct. Solut.*, vol. 6, no. 2, pp. 1–10, 2021.
- [236] P. K, D. K. J.R, K. T, I. J. J. B. Kumar, J. S. Kiran, and S. S, Smart Surveillance System for Controlling Pandemic Diseases in Airports, *SSRN Electron. J.*, no. Icinis, pp. 273–284, 2021.
- [237] E. Y. Koroteeva and A. A. Bashkatov, Thermal signatures of liquid droplets on a skin induced by emotional sweating, *Quant. Infrared Thermogr. J.*, vol. 19, no. 2, pp. 115–125, Mar. 2021.
- [238] V. A. Weidlich, Thermal Infrared Face Recognition, *Cureus*, vol. 13, no. 3, Mar. 2021.
- [239] A. Augusto, C. Paz, R. Fiorin, M. Ferro, and A. De Oliveira, 3Dthermal Models : a Case Study of the Neck 3Dthermal Models : a Case Study of the Neck, *Int. J. Dev. Res.*, vol. 10, no. November, pp. 40705–40710, 2020.
- [240] M. A. Farooq, H. Javidnia, and P. Corcoran, Performance estimation of the state-of-the-art convolution neural networks for thermal images-based gender classification system, *J. Electron. Imaging*, vol. 29, no. 06, pp. 1–20, 2020.
- [241] J. Tulloch, R. Zamani, and M. Akrami, Machine Learning in the Prevention, Diagnosis and Management of Diabetic Foot Ulcers: A Systematic Review, *IEEE Access*, vol. 8, pp. 198977–199000, 2020.
- [242] A. H. Ornek, S. Ervural, M. Ceylan, M. Konak, H. Soylyu, and D. Savasci, Classification of medical thermograms belonging neonates by using segmentation, feature engineering and machine learning algorithms, *Trait. du Signal*, vol. 37, no. 4, pp. 611–617, 2020.
- [243] U. Snehalatha, B. Guhan, S. Sowmiya, and T. Rajalakshmi, Analysis of Heel Fissure Therapy using Thermal Imaging and Image Processing, in *Proceedings of the 2020 IEEE International Conference on Communication and Signal Processing, ICCSP 2020*, Jul. 2020, pp. 326–331.

- [244] C. Ferrari, L. Berlincioni, M. Bertini, and A. Del Bimbo, Inner eye Canthus localization for human body temperature screening, in *Proceedings - International Conference on Pattern Recognition*, 2020, pp. 8833–8840.



APPENDIX

Diagnosis Form

This form is filled by Dr. Mustafa Mücahit Yılmaz while evaluating the thermograms of patients.

Dosya No:	Yaş:	Cinsiyet:	Boy:	Kilo:	Tansiyon:
-----------	------	-----------	------	-------	-----------

Sinüzit			
Tiroid	Hiperaktivite	Hipoaktivite	
Meme değerlendirilmesi	Hipertermik	Hipotermik	
Karaciğer inflamasyonu (Yağlanma)			
Dalak inflamasyonu (Hiperaktivite)			
Mide inflamasyon (Gastrit, peptik ülser, reflü)			
Bağırsak motilite bozukluğu			
Uyluk-Bacak ön	Varis (Toplardamar bozukluğu)	Arterial beslenme (Atardamar bozukluğu)	Nöronal Blokaj
Uyluk-Bacak arka	Varis (Toplardamar bozukluğu)	Arterial beslenme (Atardamar bozukluğu)	Nöronal Blokaj
Servikal Bölge	Ağrı Merkezi	Nöronal Blokaj (Fıtık)	
Thoracal Bölge	Ağrı Merkezi	Nöronal Blokaj (Fıtık)	
Lomber Bölge	Ağrı Merkezi	Nöronal Blokaj (Fıtık)	
Skolyoz			
Doktor Görüşü:			

Informed Volunteer Consent Forms

The following two forms were used to obtain signed informed consent from volunteers during their visit to the clinic. The first and second consent forms were prepared to obtain permission for processing the archived and new thermogram data of the patients, respectively.



BİLGİLENDİRİLMİŞ SAĞLIKLI GÖNÜLLÜ OLUR FORMU (BGOF)	Tarih:
	Sayfa No: 1/2

Bilgilendirme Bölümü (Arsiy verisi için):

Değerli Gönüllü,

İnsan vücudu homeotermik (vücut ısısını sabit tutabilen) olduğu için kendi ısısını sabit tutacak sistemlere sahiptir. Vücutta, ısı oluşturan ve fazla ısının atılmasını sağlayan mekanizmalar vardır. Metabolizma faaliyetleri ısı oluştururken nefes alıp-verme, terleme gibi faaliyetler de oluşan ısının vücuttan atılmasını sağlanarak vücudun sıcaklığı normal yaşamı sürdürülebilecek olan 36.5°C civarında sabit tutulmaktadır.

Sağlıklı bir bireyde vücut ısı dağılımı dengelidir. Vücutta meydana gelecek problemler bu dengeli dağılımı genel veya bölgesel olarak bozar. Örneğin termal görüntülemenin en çok kullanıldığı meme kanseri teşhisinde tümör oluşan bölge ısı değişikliğiyle kendini göstermekte ve oldukça erken fark edilmektedir. Vücutta farklı rahatsızlıkların yol açtığı termal denge bozuklukları, termal görüntüleme cihazları (termograf) ile bu alanda uzman hekimler tarafından kolayca tespit edilebilmektedir. Ağrı merkezlerinin, sinüslerde iltihap olup olmadığının, bacaklarda varis oluşumlarının, vb. tespiti için termal görüntülerin kullanılması hem ucuz hem de hastaya hiçbir zararı ve etkisi bulunmayan bir yöntemdir.

“Medikal Termal Görüntülerin Otomatik Olarak İşlenmesi ve Sınıflandırılması”, başlıklı bu çalışma ile, sağlıklı ve hasta gönüllülere ait olan termal görüntüler bilgisayar ortamında otomatik olarak işlenerek, en başarılı sınıflandırma yöntemleriyle sınıflandırılacaktır.

Amacımız, termal görüntülerin incelenmesi esnasında, geliştirilen yöntem ile yapılan tespitler sayesinde, hekimin muhakeme süresinin azaltılması ve yorulmadan kaynaklanabilecek hataların en aza indirilmesidir. Böyle bir yazılımın medikal görüntü yorumlamada tecrübesi sınırlı hekimler için de önemli bir yardımcı kaynak oluşturabileceği öngörülmektedir.

Çalışma sağlıklı ve hasta gönüllülerden alınan termal görüntüler üzerinde gerçekleştirilecektir.

Bu çalışmada Medicores firmasına ait olan IRIS-XP marka termograf ile sizden farklı açılardan termal görüntüler uzman doktorumuz tarafından alınacaktır. Bu termograf ile görüntü alırken size zararlı ya da zararsız hiçbir şey verilmez, normal kamera ile resminizin çekilmesinden farkı yoktur.

Sizden beklenen, Dr.M.M. Yılmaz klinikte önceki muayenelerinizde alınmış bulunan ve bundan sonra alınacak olan termal görüntülerin kullanımına izin vermenizdir.

Bu araştırmadan çıkan sonuçlar isminiz verilerle herhangi bir yerde yayımlanmayacak, ilan edilmeyecektir. Araştırmada 1 kişiden 15 civarında görüntü alınacaktır ve bunun için gerekli süre 10 dakika olarak düşünülmektedir. Ancak bu araştırmadan istediğiniz zaman çıkabilirsiniz. Araştırmaya katılması düşünülen gönüllü sayısı 150 kişidir. Kimliğiniz kesinlikle gizli tutulacaktır.

Araştırma süresince 24 saat ulaşılabilir kişiler:

Prof. Dr. Bülent YILMAZ

Dr. Mustafa Mücahit YILMAZ

Ahmet ÖZDİL

BİLGİLENDİRİLMİŞ SAĞLIKLI GÖNÜLLÜ OLUR FORMU (BGOF)	Tarih:
	Sayfa No: 2/2

Gönüllü Oluru Bölümü (Arşiv verisi için):

"Bilgilendirilmiş Gönüllü Olur Formundaki tüm açıklamaları okudum. Bana, konusu ve amacı belirtilen araştırma ile ilgili yazılı ve sözlü açıklama, aşağıda adı belirtilen kişi tarafından yapıldı. Araştırmaya gönüllü olarak katıldığımı, istediğim zaman gerekçeli veya gerekçesiz olarak araştırmadan ayrılabileceğimi ve kendi isteğime bakılmaksızın araştırmacı tarafından araştırma dışı bırakılabileceğimi biliyorum".

"Söz konusu araştırmaya, hiçbir baskı ve zorlama olmaksızın, kendi rızamla katılmayı kabul ediyorum".

Çalışma kapsamında benden alınan kayıtların;

- Sadece yukarıda bahsi geçen araştırmada kullanılmasına izin veriyorum.*
- İleride yapılması planlanan tüm araştırmalarda kullanılmasına izin veriyorum.*
- Hiçbir koşulda kullanılmasına izin vermiyorum.*

• Gönüllünün Adı Soyadı / İmzası / Tarih

• Açıklamaları Yapan Kişinin Adı / Soyadı / İmzası / Tarih

BİLGİLENDİRİLMİŞ SAĞLIKLI GÖNÜLLÜ OLUR FORMU (BGOF)	Tarih:
	Sayfa No: 1/2

Bilgilendirme Bölümü (Yeni hasta için):

Değerli Gönüllü,

İnsan vücudu homeotermik(vücut ısısını sabit tutabilen) olduğu için kendi ısısını sabit tutacak sistemlere sahiptir. Vücutta, ısı oluşturan ve fazla ısının atılmasını sağlayan mekanizmalar vardır. Metabolizma faaliyetleri ısı oluştururken nefes alıp-verme, terleme gibi faaliyetler de oluşan ısının vücuttan atılması sağlanarak vücudun sıcaklığı normal yaşan sürdürülebilecek olan 36,5°C civarında sabit tutulmaktadır.

Sağlıklı bir bireyde vücut ısı dağılımı dengelidir. Vücutta meydana gelecek problemler bu dengeli dağılımı genel veya bölgesel olarak bozar. Örneğin termal görüntülemenin en çok kullanıldığı meme kanseri teşhisinde tümör oluşan bölge ısı değişikliğiyle kendini göstermekte ve oldukça erken fark edilmektedir. Vücutta farklı rahatsızlıkların yol açtığı termal denge bozuklukları, termal görüntüleme cihazları(termograf) ile bu alanda uzman hekimler tarafından kolayca tespit edilebilmektedir. Ağrı merkezlerinin, sinüslerde iltihap olup olmadığının, bacaklarda varis oluşumlarının, vb. tespiti için termal görüntülerin kullanılması hem ucuz hem de hastaya hiçbir zararı ve etkisi bulunmayan bir yöntemdir.

"Medikal Termal Görüntülerin Otomatik Olarak İşlenmesi ve Sınıflandırılması", başlıklı bu çalışma ile, sağlıklı ve hasta gönüllülere ait olan termal görüntüler bilgisayar ortamında otomatik olarak işlenerek, en başarılı sınıflandırma yöntemleriyle sınıflandırılacaktır.

Amacımız, termal görüntülerin incelenmesi esnasında, geliştirilen yöntem ile yapılan tespitler sayesinde, hekimin muhakeme süresinin azaltılması ve yorundan kaynaklanabilecek hataların en aza indirilmesidir. Böyle bir yazılımın medikal görüntü yorumlamada tecrübesi sınırlı hekimler için de önemli bir yardımcı kaynak oluşturabileceği öngörülmektedir.

Çalışma sağlıklı ve hasta gönüllülerden alınan termal görüntüler üzerinde gerçekleştirilecektir.

Bu çalışmada Medcore firmasına ait olan IRIS-XP marka termograf ile sizden farklı açılardan termal görüntüler uzman doktorumuz tarafından alınacaktır. Bu termograf ile görüntü alırken size zararlı ya da zararsız hiçbir şey verilmez, normal kamera ile resminizin çekilmesinden farkı yoktur.

Sizden beklenen, vücudunuzun rahat ve terlememiş olması, görüntüler alınırken doktorun belirttiği konumu almanızdır.

Bu araştırmadan çıkan sonuçlar isminiz verilerek herhangi bir yerde yayımlanmayacak, ilan edilmeyecektir. Araştırmada 1 kişiden 15 civarında görüntü alınacaktır ve bunun için gerekli süre 10 dakika civarındadır. Ancak bu araştırmadan istediğiniz zaman çıkabilirsiniz. Araştırmaya katılması düşünülen gönüllü sayısı 150 kişidir. Kimliğiniz kesinlikle gizli tutulacaktır.

Araştırma süresince 24 saat ulaşılabilir kişiler:

Prof. Dr. Bülent YILMAZ

Dr. Mustafa Mücahit YILMAZ

Ahmet ÖZDİL

BİLGİLENDİRİLMİŞ SAĞLIKLI GÖNÜLLÜ OLUR FORMU (BGOF)	Tarih:
	Sayfa No: 2/2

Gönüllü Oluru Bölümü (Yeni hasta için):

“Bilgilendirilmiş Gönüllü Olur Formundaki tüm açıklamaları okudum. Bana, konusu ve amacı belirtilen araştırma ile ilgili yazılı ve sözlü açıklama, aşağıda adı belirtilen kişi tarafından yapıldı. Araştırmaya gönüllü olarak katıldığımı, istediğim zaman gerekçeli veya gerekçesiz olarak araştırmadan ayrılabileceğimi ve kendi isteğime bakılmaksızın araştırmacı tarafından araştırma dışı bırakılabileceğimi biliyorum”.

“Söz konusu araştırmaya, hiçbir baskı ve zorlama olmaksızın, kendi rızamla katılmayı kabul ediyorum”.

Çalışma kapsamında benden alınan kayıtların;

- Sadece yukarıda bahsi geçen araştırmada kullanılmasına izin veriyorum.*
- İleride yapılması planlanan tüm araştırmalarda kullanılmasına izin veriyorum.*
- Hiçbir koşulda kullanılmasına izin vermiyorum.*

• Gönüllünün Adı Soyadı / İmzası / Tarih

• Açıklamaları Yapan Kişinin Adı / Soyadı / İmzası / Tarih

CURRICULUM VITAE

2002 – 2008	B.Sc., Computer Engineering, Yıldız Technical University, İstanbul, TÜRKİYE
2013 – 2015	M.Sc., Electrical and Computer Engineering, Melikşah University, Kayseri, TÜRKİYE
2016 – 2022	Ph.D., Electrical and Computer Engineering, Abdullah Gül University, Kayseri, TÜRKİYE
2009 – 2012	Software Engineer AKEAD Bilişim, İstanbul, TÜRKİYE
2012 – 2019	Research Assistant, Computer Engineering, Abdullah Gül University, Kayseri, TÜRKİYE
2019 – present	Research Assistant, Computer Engineering, Kırşehir Ahi Evran University, Kırşehir, TÜRKİYE

SELECTED PUBLICATIONS AND PRESENTATIONS

- J1)** A. Özdil, B. Yılmaz, Automatic body part and pose detection in medical infrared thermal images, published in QIRT Journal, DOI: 10.1080/17686733.2021.1947595.
- J2)** A. Özdil, B. Yılmaz, Medical infrared thermal image based fatty liver classification using machine and deep learning, published in.
- J3)** A. Özdil, B. Yılmaz, Localized quantification of medical infrared thermal images for multiple sclerosis assessment and monitoring, published in.